



Numerical Investigation of Propeller–Ice Interaction Effects

Aaqib Khan

Master Thesis

presented in partial fulfillment
of the requirements for the double degree:
“Advanced Master in Naval Architecture” conferred by University of Liege
“Master of Sciences in Applied Mechanics, specialization in Hydrodynamics,
Energetics and Propulsion” conferred by Ecole Centrale de Nantes

developed at University of Rostock, Rostock
in the framework of the

**“EMSHIP”
Erasmus Mundus Master Course
in “Integrated Advanced Ship Design”**

EMJMD 159652 – Grant Agreement 2015-1687

Supervisor: Dr. Nikolai Kornev, University of Rostock, Rostock

Reviewer: Dr. Zhe Li, Ecole Centrale de Nantes, Nantes

Rostock, February 2018



Declaration of Authorship

I, Aaqib Khan, declare that this thesis, “Numerical Investigation of Propeller–Ice Interaction Effects” and the work presented in it is my own and has been generated by me as a result of my own original research.

I confirm that:

1. This work was done wholly or mainly while in candidature for a research degree at this University;
2. Where any part of this thesis has previously been submitted for a degree or any other qualification at this University or any other institution, this has been clearly stated;
3. Where I have consulted the published work of others, this is always clearly attributed;
4. Where I have quoted from the work of others, the source is always given. With the exception of such quotations, this thesis is entirely my own work;
5. I have acknowledged all main sources of help;
6. Where the thesis is based on work done by myself jointly with others, I have made clear exactly what was done by others and what I have contributed myself;
7. Neither none of this work has been published before submission nor any part of this work has been published;
8. I cede copyright of the thesis in favor of the University of Rostock, Rostock.

Signed:

Date: 15 January 2018

TABLE OF CONTENTS

ABSTRACT.....	12
INTRODUCTION.....	14
1.1 Motivation.....	14
1.2 Aim & Scope.....	15
1.3 Theoretical Background & Research Methodology.....	15
LITERATURE REVIEW & PRIOR ART.....	17
2.1 V. Ya Jagodkin, 1963.....	17
2.2 Ignatjev M.A., 1964 & 1966.....	18
2.3 Wind J., 1984.....	20
2.4 Veitch B., 1992.....	21
2.5 Jones S. J., 1997.....	22
2.6 Soininen H., 1998.....	23
2.7 Wang J., 2007.....	25
2.8 Bach C., 2017.....	25
2.9 Other Approaches.....	26
2.10 Class Rules.....	28
THE ICE-PPB.....	29
3.1 The Coordinate System and Conventions.....	29
3.2 The Ice-PPB Algorithm.....	30
3.3 Input Data.....	34
3.3.1 Hydrodynamic Data.....	34
3.3.2 Ice Data.....	35
3.4 The Ice Wake Field.....	36
3.4.1 Determination of the Wake Velocity.....	36
3.4.2 Determination of the Wake Region.....	38
3.5 Calculation of the Hydrodynamic Loads.....	42
3.5.1 Calculation of the propeller torque and thrust.....	42
3.5.2 Calculation of the Slipstream Velocity.....	43
3.6 Calculation of the Ice-Loads.....	43
3.6.1 Shadow Effect.....	45

3.7	Polar Class Code.....	47
THE EXPERIMENTS		48
4.1	The Propeller	48
4.2	The Open Water Test.....	49
4.3	Air and Water Milling Experiments.....	50
4.3.1	Large Ice Tank of HSV A.....	51
4.3.2	The Ice Making Process.....	52
4.3.3	The Ice Feeding Device	53
4.3.4	The Test Set-up	55
4.3.5	The Air Milling Experiment	56
4.3.6	The Water Milling Experiment	57
4.3.7	The Ice Compression Test	58
4.3.8	Data Processing and Results	59
CODE CALIBRATION & RESULTS		64
5.1	Calibration of the Separable Hydrodynamic Loads	64
5.1.1	Convergence of the Input Parameters	64
5.1.2	Comparison of the Open Water Results	65
5.1.3	Viscous Correction	68
5.2	Calibration of the Ice Loads	71
5.2.1	Empirical Factor for Crushing.....	71
5.2.2	Empirical Factor for Shearing.....	72
5.3	Calibration of the Inseparable Hydrodynamic Loads	73
5.4	Results and Critical Analysis	73
5.4.1	Influence of Parameters	73
5.4.2	Sensitivity Analysis.....	85
5.4.3	Results from Polar Class Code.....	92
CONCLUSION.....		93
6.1	Conclusion.....	93
6.1.1	Separable Hydrodynamic Loads	94
6.1.2	Inseparable Hydrodynamic Loads	94
6.1.3	Ice Contact Loads	94

6.2 Recommendations.....	95
ACKNOWLEDGEMENTS.....	97
REFERENCES.....	98
ANNEXURE 01.....	101
A. Calculation of Geometrical Parameters of Panels	101
A.1 Calculation of the centroid	101
A.2 Calculation of Normal, Radial and Tangential Vectors.....	102
A.3 Calculation of Area	103
B. Calculation of K_T , K_Q and Efficiency	104
ANNEXURE 02.....	106

LIST OF FIGURES

Figure 1: Ice Loads on a Blade Section [6].....	17
Figure 2: Propeller Geometry and Blade Load Distribution [7]	19
Figure 3: Different Aspects of the Propeller Ice Interaction [9].....	21
Figure 4: The Structure of the Model Development and General Flow of the Simulation Process [10]	23
Figure 5: Schematic Representation of the Simulation Model and the Approach Used [11]	24
Figure 6: Schematic Representation of the Ice Feeding Device [14]	26
Figure 7: The Coordinate System and Conventions.....	29
Figure 8: Simplified Algorithm of Ice-PPB.....	31
Figure 9: Propeller with Planar Ice Floe.....	32
Figure 10: Propeller with Sector Ice Floe.....	32
Figure 11: Paneled Vortex Wake Structure (modified [32]).....	35
Figure 12: Three Stages of Propeller Ice Interaction (modified [33])	37
Figure 13: Grid for Calculation of Wake Field.....	38
Figure 14: Representation of the Milling Angle (modified [4, 5]).....	39
Figure 15: Wake Region along with the Propeller for Planar Ice Floe	39
Figure 16: Plot of the Normalized Advance Velocity around the Propeller Disc for Planar Ice Floe	40
Figure 17: Wake Region along with the Propeller for Sector Ice Floe	41
Figure 18: Plot of the Normalized Advance Velocity around the Propeller Disc for Sector Ice Floe	41
Figure 19: Crushing (Left) and Shearing (Right) of Ice during milling [32]	44
Figure 20: Shadow Panels	46
Figure 21: Variation of the Shadow Panels with Advance Coefficient.....	47
Figure 22: Schematic Representation of the Polarstern Propeller (Top) and Pod (Bottom) [32].....	49
Figure 23: Results of the Open Water test for Polarstern Propeller with pod in pusher mode [32]...50	50
Figure 24: Schematic Representation of the Large Ice Tank at HSVA [32]	51
Figure 25 : Ice floes used in the Experiments	52
Figure 26 : Side View of the Ice Feeding Device [32]	53
Figure 27: Top View of the Ice Feeding Device [32]	53
Figure 28: Front View of the Ice Feeding Device [32].....	54
Figure 29: The Guiding Mechanism [32].....	55
Figure 30: Ice Feeding Device in Air Milling Experiment.....	56
Figure 31: Raw Data from the Air Milling Experiment	57
Figure 32: Raw Data from the Water Milling Experiment	58
Figure 33: Compression Test of Ice: Start (Left), End (Right)	59
Figure 34: Raw Data and Offset Data	60
Figure 35: Frequency Spectrum of Raw Signals from Air Milling.....	61
Figure 36: Frequency Spectrum of Raw Signals from Water Milling.....	62
Figure 37: Convergence of the Input Parameters for Hydrodynamic Loads	65
Figure 38: Comparison of the Open Water Results	66
Figure 39 : Comparison of Open Water Thrust Coefficient.....	67

Figure 40: Pressure & Suction Panels and Surface Normal Vectors	68
Figure 41: Modification of the Mirror Panels	70
Figure 42: Comparison of the Open Water Results - After Corrections.....	70
Figure 43: Variation of KT and KQ with J (Hydrodynamic and Ice Loads Combined)	74
Figure 44: Variation of Normalized Slipstream Velocity along Propeller Race.....	75
Figure 45: Variation of Normalized Acceleration along Propeller Race	76
Figure 46: Variation of Shadow Panels (black) with J Value at 10 mm DOC	77
Figure 47: Variation of Shadow Panels (black) with J Value at 30 mm DOC	77
Figure 48: Variation of Ice Loads with J Value at 30 mm DOC	78
Figure 49: Variation of Hydrodynamic Loads with DOC	79
Figure 50: Variation of Ice wake Field with DOC.....	80
Figure 51: Variation of Ice Loads with DOC.....	80
Figure 52: Variation of Ice Loads with Ice Compressive Strength	81
Figure 53: Variation of Ice Loads with Ice Compressive Strength at constant EFC of 0.14.....	83
Figure 54: Variation of Hydrodynamic Loads with Propeller RPS	84
Figure 55: Variation Ice Loads with Propeller RPS.....	85
Figure 56: Change in Ice Loads with EFC.....	87
Figure 57: Influence of Parameters on the Sensitivity of EFC	87
Figure 58: Change in Ice Loads with W_{avg}	88
Figure 59: Influence of Parameters on the Sensitivity of W_{avg}	88
Figure 60: Change in Ice Loads with EFS.....	89
Figure 61: Influence of Parameters on the Sensitivity of EFS.....	90
Figure 62: Change in Ice Loads with W_{max}	91
Figure 63: Influence of Parameters on the Sensitivity of W_{max}	91
Figure A-1: 3D Quadrilateral	101

LIST OF TABLES

Table 1 : Hydrodynamic Input Data.....	34
Table 2 : Ice Input Data.....	35
Table 3: Geometrical Characteristics of the Polarstern Propeller [32].....	48
Table 4: Open Water Test Parameters [32].....	50
Table 5 : Main Parameters of the Large Ice Tank at HSVA [32].....	51
Table 6: The Data Channels Recorded During the Experiment	56
Table 7 : Test Parameters of Air Milling Experiment	57
Table 8 : Test Parameters of Water Milling Experiment	58
Table 9: Compression Test of Ice: Parameters and Results	59
Table 10: Design Parameters of the Frequency Filter	62
Table 11 : Results from the Milling Experiment.....	63
Table 12 : Input Data for Convergence Study.....	64
Table 13: Comparison of Results of Ice Milling	72
Table 14: Model Parameters for the study of variation of Hydrodynamic and Ice Loads with J values	74
Table 15: Model Parameters for the study of variation of Hydrodynamic and Ice Loads with DOC.....	79
Table 16: Model Parameters for the study of variation of Ice Loads with Ice Compressive Strength	81
Table 17: Model Parameters for the study of variation of Hydrodynamic and Ice Loads with RPM	84
Table 18: Model Parameters for the Sensitivity Analysis of Empirical Factors.....	86
Table 19: Maximum Permissible Loads on the Full Scale of Polarstern Propeller	92
Table T: Load Case Definition	106
Table U: Values of Ice Thickness and Ice Strength Indices.....	108

ABSTRACT

Within the framework of German national funded research project ProEis, focusing on the propeller-ice interaction, an innovative numerical tool has been developed to assess the effects of such phenomenon on the loads acting on the propeller and on its propulsive efficiency. The proposed methodology is to calculate the loads on the propeller as the sum of the separable hydrodynamic loads, the inseparable hydrodynamic loads and the ice contact loads. The separable hydrodynamic loads are the loads acting on the propeller in ice-free water whereas the inseparable hydrodynamic loads act on the propeller due to the ice blockage effect. Both of these loads are calculated by a panel based code. The loads originating from the physical contact between ice particles and the propeller, called the ice-contact loads have a significant contribution to the total loads acting on the propeller. They are calculated using the empirical formulae as given by Wang J. (2007), subdividing the physical propeller-ice interaction into crushing and shearing phenomena. Several interaction scenarios (size, location and strength of ice piece(s)) are modeled & compared and the effect of various parameters is quantified. The numerical tool is calibrated from the results of a model test campaign focused on propeller-ice interaction and in which a linear feeding device is used to guide ice floes into a model propeller to be milled under controlled conditions. Milling tests have been carried out both in the water and in the air, in order to identify the contribution of each type of load to the total load measured on the propeller. The report ends with conclusions and suggests further work to be performed in order to enhance the numerical model.

Key Words: Propeller-ice interaction, ice loads, ice-class, ice going vessels.

Chapter 1

INTRODUCTION

1.1 Motivation

Mankind has been interested in venturing into the vastness of the Arctic since the ancient times. Historical records show that the Greek sailor Pytheas sailed into the Arctic as early as 325 BC [1]. Since then mankind has made continued efforts to conquer the polar regions of our planet. The demand of the fossil fuels has increased exponentially in the last few decades owing to the increasing industrialization, population explosion and improvement in the living standards of people. This ever increasing requirement of the fossil fuels led to the exploration of the new reserves in the polar ice caps. The offshore oil and gas exploration in the Arctic led to a significant increase in the marine traffic in the region as ships were required to transport these natural resources from the Arctic throughout the year. Additionally, the opening of the new trade routes in the Arctic for trade between the ports of Arctic cities, and the intercontinental shipping routes, like the northern sea route, further added to the marine traffic in the Arctic.

With the increase in the marine traffic in the Arctic regions, there is a growing demand for reliable and efficient ice going ships. An ice going vessel needs to have the additional hull strength to withstand the hull–ice interaction loads. The shape of the hull should be such that it breaks the sea ice as the ship moves through it and the material of construction should be a metal that retains its strength in freezing temperatures. Moreover, the propulsion system also needs to be robust so that it can withstand the ice interaction. The interaction of the propeller with ice results in the increased torque on the engine shaft and the reduced thrust on the propeller blades. The milling of the ice by the propeller leads to a significant increase in the stresses on the blades. This can lead to the propeller blade damage, or the partial or complete loss of the propeller, which in high seas is a catastrophic situation.

Therefore, HSVA, a private, self–supporting, non–profit organization is currently engaged in research to evaluate the loads on the propeller due to the ice interactions. This is done under the project ProEis. The project is funded by the German Ministry of Economics and Technology in collaboration with HSVA, DNV GL, MMG Propeller, Voith, MV Werften and Develogic. HSVA has the in–house capabilities to perform the model tests of the ice class propellers. However, they do not have a numerical simulation tool to predict the behavior of these ice class propellers in varied ice conditions.

A numerical simulation tool called PPB (Propeller Panel-Based) based on the surface panel method was however, earlier developed by HSVA for calculating the induced velocity field and predicting the performance of the propellers in normal (ice-free) water [2]. The aim is to develop the numerical simulation tool further, so that the propeller-ice interactions can be taken into account while calculating the induced velocity field and the thrust & torque on the propellers.

The new numerical simulation tool calculates the hydrodynamic loads, induced velocity field as well as the ice loads acting on the propeller during its interaction with ice. The development of this tool is the basis of the master thesis at HSVA.

1.2 Aim & Scope

The primary objective of the master thesis is to develop a numerical simulation tool to calculate the ice loads along with the hydrodynamic loads acting on a propeller during its interaction with ice. This numerical simulation tool called Ice-PPB is then calibrated on the basis of the results obtained from the experiments on the propeller-ice interaction carried out in the ice tank of HSVA.

The first step in the process is to select a suitable model for accurately calculating the ice loads. After the model is selected, the present numerical simulation tool PPB is used to obtain the induced velocity field and hydrodynamic load data of the propeller. This load data includes the panel definitions and the coefficient of pressure (C_p) and normalized tangential force per unit area (T_w) acting on each panel. The data obtained from PPB is then processed by Ice-PPB which then calculates the hydrodynamic as well as the ice loads (torque and thrust) acting on the propeller and superimposes the two results. Ice-PPB also has a module that compares the results obtained from the simulation with those given by the IACS polar class code [3].

The results obtained from the experiments carried out in the ice tank on the propeller-ice interaction are used to calibrate the numerical simulation tool so that the error between the experimental results and simulation results is minimized, making the numerical simulation tool more accurate and precise.

The scope of the report is thus defined in accordance with the aim. The chapter 2 of the report summarizes the existing knowledge and theories in the field of propeller-ice interaction. The chapter 3 explains the algorithm and mathematics involved in the numerical code Ice-PPB. The chapter 4 describes the experiments and the post processing of the data to obtain the results. The chapter 5 deals with the comparison of the results obtained from the numerical simulation tool and the experiments, and also the process of the calibration of the simulation tool. The report ends with chapter 6 that summarizes the results and draws a suitable conclusion based on the report. It also highlights the shortcomings of the simulation tool and the research carried out, and provides the recommendations for developing a better tool.

1.3 Theoretical Background & Research Methodology

In order to find a suitable theoretical model to calculate the ice loads on a propeller during its interaction with ice, a number of research papers, doctoral thesis, technical reports, etc., were

considered as mentioned in chapter 2 of this report. In order to select the most appropriate model a number of factors were taken into the account as mentioned below:

- a. An accurate theoretical model with minimum assumptions and closest resemblance to the real life scenarios.
- b. A theoretical model using a deterministic approach rather than a probabilistic approach to calculate the ice loads.
- c. The adaptability of the theoretical model to a panel method as the original hydrodynamic code is based on the surface panel method.
- d. The ease of developing the numerical model from the given theory in a limited time.
- e. The ease of performing the experiments in order to calibrate the numerical simulation tool.

The most suitable model was the one used by Wang, J., (2007) [4, 5]. In his doctoral thesis, Wang identifies three types of loads acting on the propeller in contact with ice.

- a. Separable Hydrodynamic Loads: These are the loads that act on the propeller due to the presence of water. They are called separable loads as they can be calculated independently without the presence of ice. These hydrodynamic loads are calculated in a separate experiment and compared with the values obtained from Ice-PPB.
- b. Inseparable Hydrodynamic Loads: These are the hydrodynamic loads that act on the propeller in the presence of ice. Due to the presence of ice, there are blockage and proximity effects. These phenomena are simulated by a wake field and these additional loads on the propeller are also calculated by Ice-PPB. Since these hydrodynamic loads cannot be calculated independently in an experiment and require the presence of ice to be evaluated, therefore they are called Inseparable Hydrodynamic Loads.
- c. Ice-Milling Loads: These are the loads that act on the propeller due to the milling of ice particles by the propeller blades. They are primarily of two types; loads due to the crushing of the ice by the propeller blades and loads due to the shearing of ice by the propeller blades. Thus we have,

$$\text{Total loads on the propeller during ice interaction} = \text{Separable Hydrodynamic Loads} + \text{Inseparable Hydrodynamic Loads} + \text{Ice-Milling Loads}$$

In order to evaluate these loads individually, three separate experiments were performed. In the first experiment the separable hydrodynamic loads were calculated by performing the experiment in ice-free water. In the second experiment, the ice-milling loads were calculated by performing the milling of ice by the propeller in air. Finally, in the third experiment, the total loads were calculated by performing the milling of ice by the propeller in water. Thus, by adding the load values obtained from the first and second experiment and subtracting this sum from the load values obtained from third experiment, the inseparable hydrodynamic loads were evaluated. The numerical code provides the values of all the three types of loads and thus comparison is made with respect to each type of load. This leads to a better calibration of the code.

Chapter 2

LITERATURE REVIEW & PRIOR ART

The research regarding the interaction of the propeller with sea ice is mainly done by the universities and research organizations of the Scandinavian countries, Finland, Russia and Canada as these countries host the majority of the maritime traffic in the Arctic due to their climate. As a result most of the research papers, thesis etc. on propeller ice interaction mentioned below belong to the researchers from these countries.

2.1 V. Ya Jagodkin, 1963

To begin with, one of the earliest researches on the subject of propeller-ice interaction was done by V. Ya Jagodkin [6]. In his paper, Jagodkin is mainly concerned about the determination of the torque on the propeller due to the ice loads as the presence of ice in the water offers added resistance to the propeller rotation. He considers milling of the ice as the most important interaction and neglects the axial and radial components of the ice loads. The aim here is to provide sufficient torque to the propeller so that the propeller does not stop rotating once it encounters ice and the milling of the ice is carried out smoothly.

In his paper, he identifies two types of ice failure modes; the first being combined crushing and shearing and the second being pure crushing. Figure 1 gives us the schematic representation of the propeller geometry and the forces.

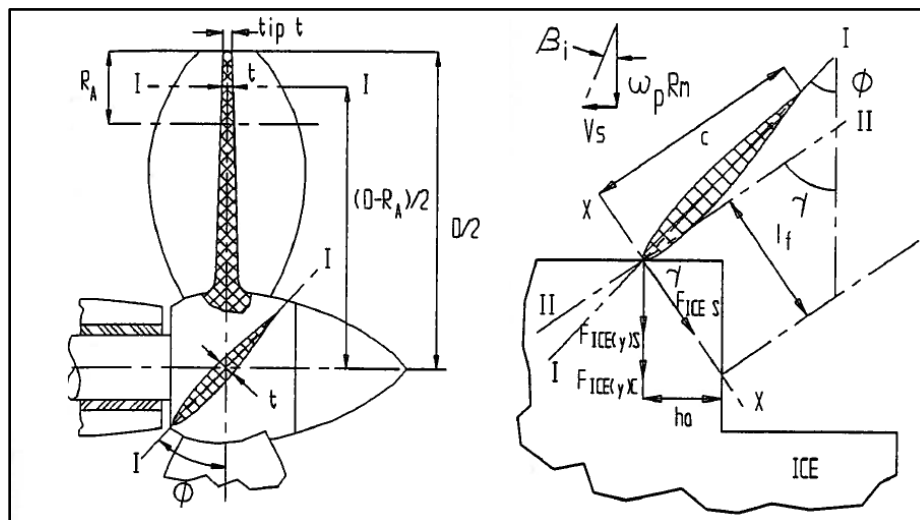


Figure 1: Ice Loads on a Blade Section [6]

For the first case, the tangential force due to the ice fracture (F_{ICE}) is given as the sum of the tangential components of crushing ($F_{ICE (C)}$) and shearing loads ($F_{ICE (S)}$). Thus,

$$F_{ICE} = F_{ICE (C)} + F_{ICE (S)}$$

He then proceeds to calculate these forces based on the propeller and ice geometry and finally arrives at the value of the torque required (T_{ICE}) as,

$$T_{ICE} = \left\{ S_C t R_A + S_S \frac{V_S}{Nn} R_A \right\} \frac{D - R_A}{2}$$

For the second case, according to Jagodkin, the pure crushing takes place only when the propeller speed is small. For this case, the value of the torque is calculated as,

$$T_{ICE} = S_C R_A C |\sin(\phi - \beta_i)| \frac{D - R_A}{2}$$

Where,

S_C = Crushing Strength of ice

S_S = Shearing Strength of ice

t = Average Blade Thickness

R_A = Depth of Cut

D = Propeller Diameter

V_S = Ship Speed

n = Speed of the Propeller in RPS

N = Number of Blades of the Propeller

ϕ = Pitch Angle

β_i = Advance angle of blade section at radius R_m

C = Average Blade Section Chord Length in the cut ice

To validate his theory, he performed experiments in full scale aboard the vessel *I/B Kapitan Voronin*. The measured values from the experiments were slightly lower than the ones predicted from the theory but the difference was acceptable. However, this method is limited to the prediction of the shaft torque only and does not provide any information regarding the stresses developed in the propeller blades due to the interaction with the ice.

This paper of Jagodkin is one of the earliest known works, thus being the reference for all the subsequent works carried out in the field.

2.2 Ignatjev M.A., 1964 & 1966

According to Ignatjev M.A., [7], the blade bending moment was the most important ice load on the propeller blades. For a loading case in which the ice load is assumed to be evenly distributed over 2/3 of the blade span, he proposed a method to evaluate the blade bending moment of the root section.

According to Ignatjev, the bending moment (M_{ICE}) is given as,

$$M_{ICE} = \frac{2}{3} F_{ICE} \sin(\phi_{root} + \zeta)(R - r_{root})$$

$$F_{ICE} = \frac{3T_{ICE}}{(2R + r_{root}) \cos \zeta}$$

$$\zeta = \tan^{-1} \left\{ \frac{2S_S(R - r_{root})(2R + r_{root}) V_S \cos \phi}{9nNT_{ICE}} \right\}$$

Where,

S_S = Shearing Strength of ice

r_{root} = Radius of the hub of the propeller

R = Radius of the propeller measured from the tip of the blade to the axis of the hub

V_S = Ship Speed

n = Speed of the propeller in RPS

N = Number of blades of the propeller

ϕ = Pitch Angle

T_{ICE} = Torque on the propeller shaft due to ice loads

Figure 2 gives us the schematic representation of the propeller geometry and the forces. From the above equations and Figure 2, we can see that we have all the data available to calculate the value of the bending moment (M_{ICE}), except for the torque on the propeller shaft due to the ice loads (T_{ICE}). Ignatjev calculates this value from the diagram of maximum torque versus propeller diameter which is obtained from the full scale experimental results. Once we have the value of the bending moment, we can obtain the section modulus (Z) of the blades, keeping in mind the required factor of safety and the yield strength of the material of construction of the propeller blades.

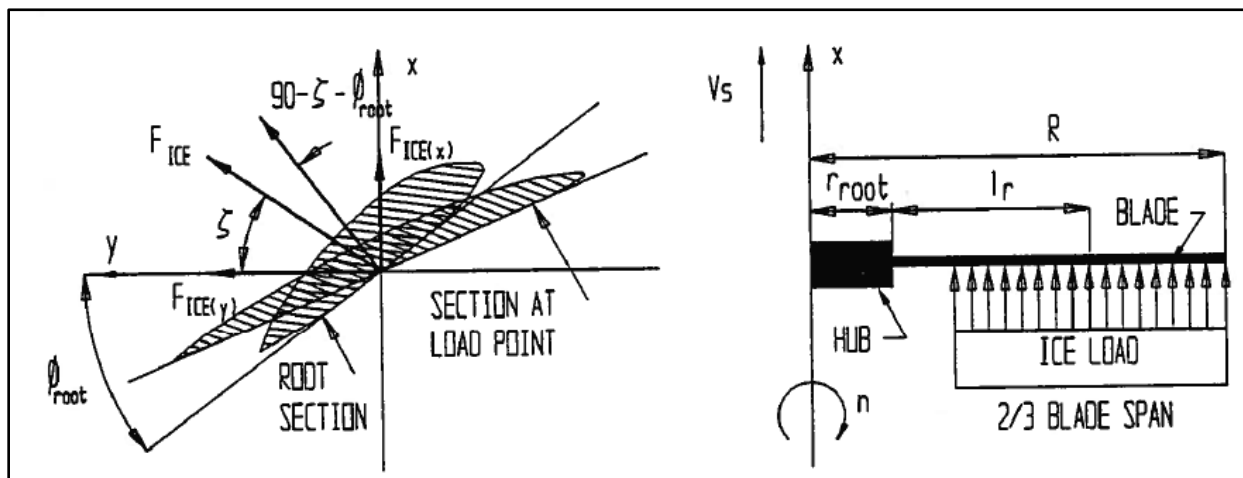


Figure 2: Propeller Geometry and Blade Load Distribution [7]

2.3 Wind J., 1984

Wind J., [8] similar to Ignatjev [7] also established that the bending moment was the most important ice load on the propeller blades. However, his approach of calculations was different in the sense that he advocated that the critical loads are not due to the milling as said by Jagodkin [6] and Ignatjev [7] earlier, but rather they occur during the impact events.

In order to calculate the moment (M_{ICE}), Wind first calculated the force and then multiplied it by the lever arm. Knowing the yield strength of the material (σ_y) of the propeller, he obtained the section modulus (Z). The impact force (F_{ICE}) is given as,

$$F_{ICE} = m_{ICE} \times \frac{V_{ICE}}{t}$$

$$M_{ICE} = F_{ICE} \left\{ \frac{D}{2} - \frac{h_{ICE}}{4} - r \right\} \cos \phi$$

$$Z = \frac{M_{ICE}}{\sigma_y} \times (Factor\ of\ Safety)$$

The ice fragment that will come in contact with the propeller varies in size and mass. To be on a conservative side, Wind used the maximum mass of ice fragment that can be generated by an ice breaking vessel and is given as,

$$m_{ICE} = \rho_{ICE} \frac{B^2}{4} h_{ICE}$$

Where,

V_{ICE} = Velocity of ice fragment relative to propeller

D = Propeller Diameter

h_{ICE} = Thickness of the ice

r = Radius of a point at which the load is acting measured from the axis of propeller

ϕ = Pitch angle

ρ_{ICE} = Density of the ice

B = Ship Beam

t = Time interval

In the above given equations, we have all the necessary data to calculate the modulus of the propeller at a radius (r), except the time interval (t). Wind assumed the time interval to be equal to 1/6 of the propeller rotation speed (n) which is approximately the time taken by the blade to pass over its full chord length.

2.4 Veitch B., 1992

In his doctoral thesis, Veitch [9] divides the process of propeller-ice interaction into three stages; the first stage is the approach of the ice fragment towards the propeller; the second stage is the blockage of the flow to the propeller blades and the third stage is the actual contact between the propeller blades and the ice followed by the milling and/or crushing of the ice fragment. According to him, the theoretical methods provided by Ignatjev (1964) and Wind (1984) to calculate the bending moment were inadequate in terms of predicting the interaction loads as they did not consider the ice mechanics.

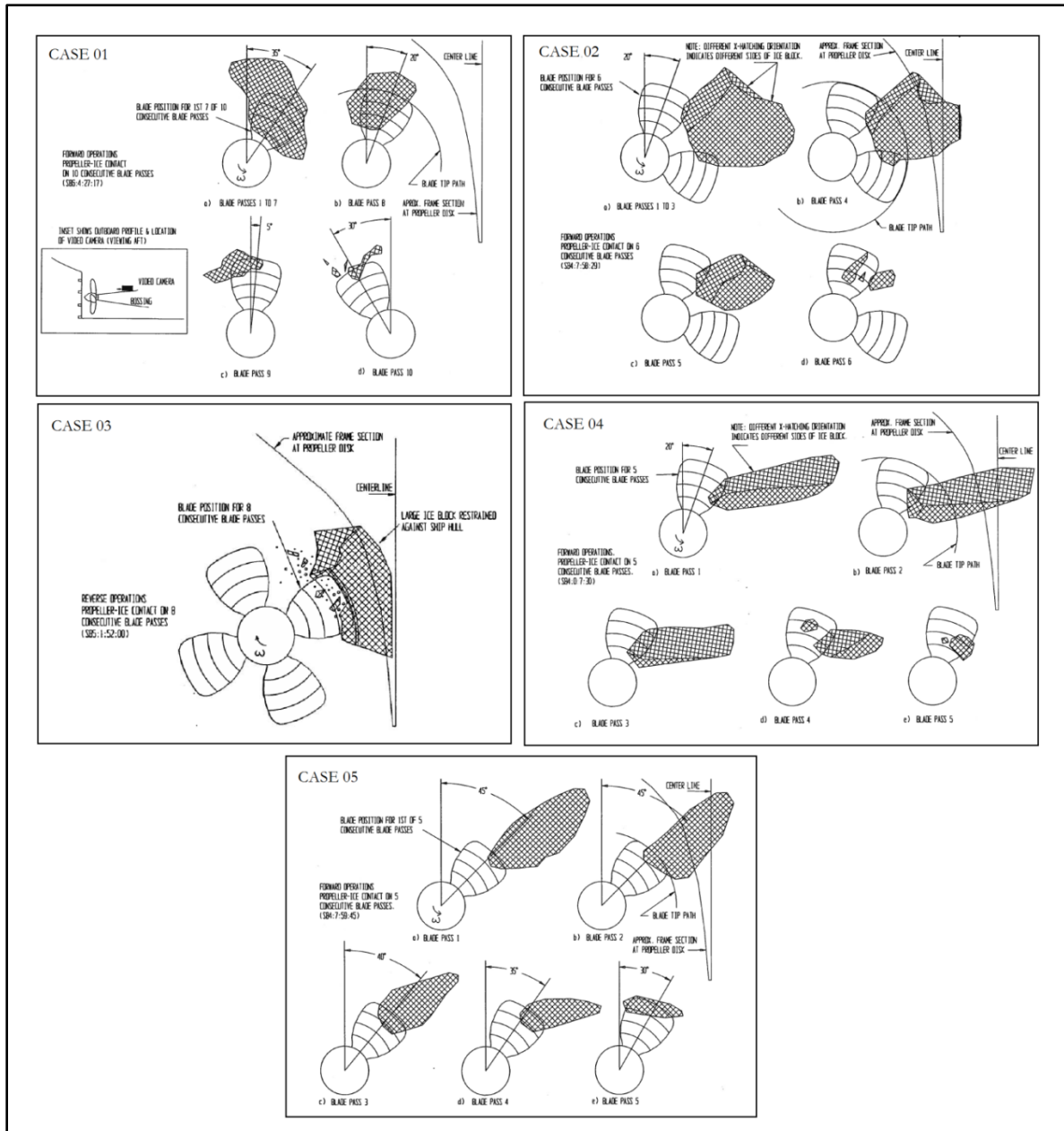


Figure 3: Different Aspects of the Propeller Ice Interaction [9]

In order to understand the ice mechanics, he provides the details of the propeller–ice interaction of the Finnish Vessel I/B Karhu in this thesis. The high frame rate videos recorded from the stern of the ship are used to develop 5 sketches which illustrate the several features of the ice interaction as shown in Figure 3 above. These figures are very important to understand the propeller–ice interaction as they provide the intricate details based on the videos taken by a slow motion camera. From the Figure 3 we can identify 5 cases as mentioned below:

- Case 01: In this figure, we can see the propeller blade and the ice contact on 10 consecutive blade passes during the forward motion of the ship.
- Case 02: In this figure, we can see the interaction between the outer half of the leading edge of the blade and the ice block during forward ship motion.
- Case 03: In this figure, we can see the interaction during the reverse ship motion. A large ice fragment is wedged and subsequently milled by the blades in 8 passes before getting detached from the propeller. The depth of the cut is about 25–30% of the blade span.
- Case 04: In this figure, from blade passes 6–8, the ice block is milled by the blades and in the last pass the remaining piece of ice is thrown off in the tangential direction.
- Case 05: In this figure, we can see the ice contact at the leading edge of the blade tip. Moreover, motion of the ice block in this case is quite evident.

The approach that Veitch followed was mostly experimental; however, a more rigorous theoretical treatment of the propeller–ice interaction was required. This was done by other researchers as mentioned below.

2.5 Jones S. J., 1997

Jones [10] identified the two components of the load that was experienced by the propeller; one was the direct contact force due to the penetration of the blade into the ice block, and the second was the hydrodynamic non–contact load.

According to Jones, the hydrodynamic loads include both the resistance due to the ice–free water and the resistance due to the ice fragments floating in the water. The contact loads on the other hand arise directly from the propeller–ice interaction.

The work of Jones et al. was part of a project funded by the Canadian Coast Guard and Finnish Board of Navigation, called Joint Research Project Arrangement 6 (JRPA#6) which aimed at the development of the new propeller–ice interaction model. Until then, all the ice regulations were based on the torque generated on the propeller shaft due to ice (Jagodkin’s method) and therefore were quite redundant.

In order to develop the new model, both theoretical analysis and experimental modeling of the involved physical phenomenon was done. The contact load model was developed in Finland, whereas the model for hydrodynamic non–contact loads was developed in Canada. Both the models were combined and finally a simple regression type model was developed based on parametric study of the results. The advantage of this approach over the approach of Veitch (1992) was that apart from the experimental modeling a strong theoretical analysis was done.

The structure of the model development and a general flow of the simulation process are given in Figure 4.

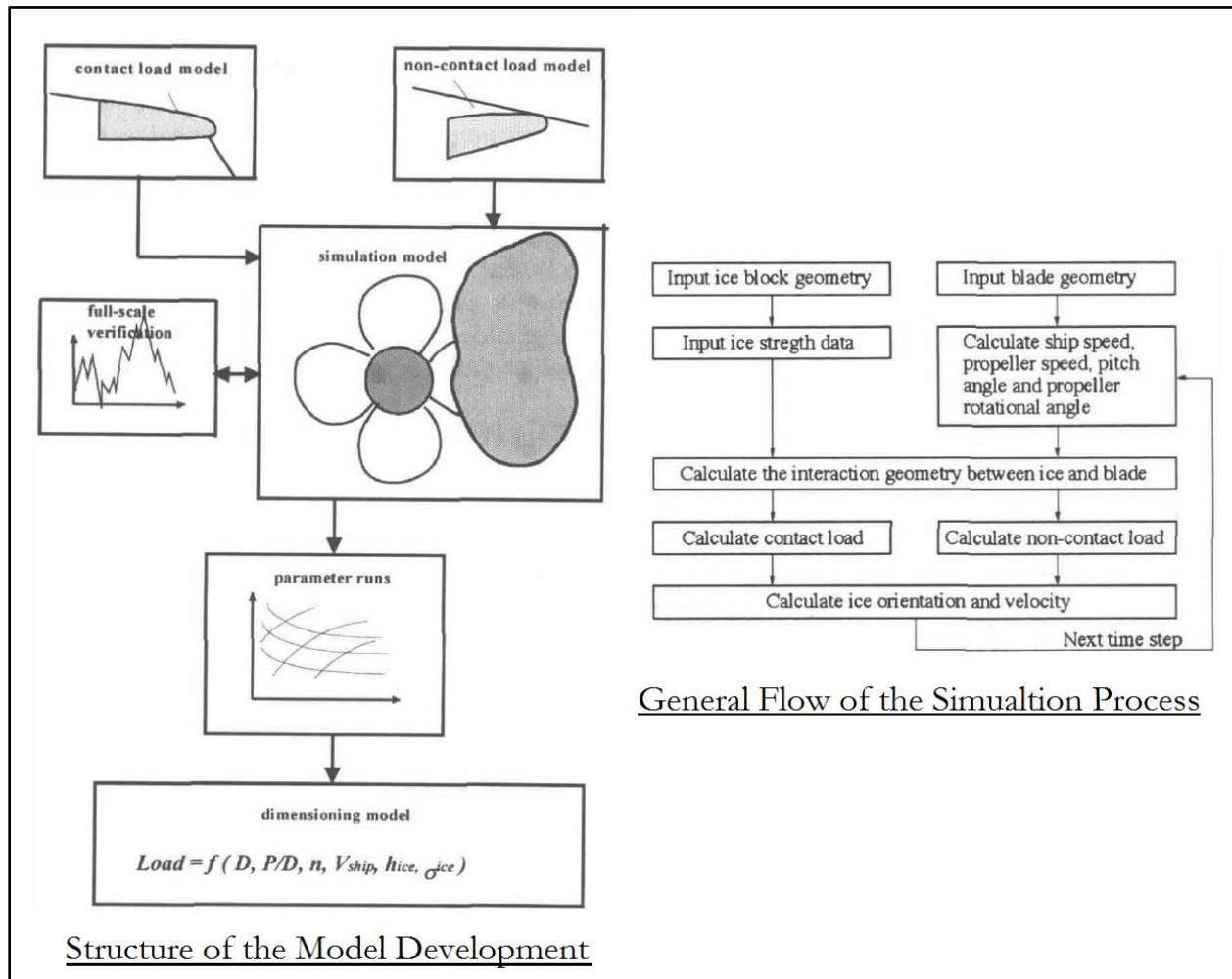


Figure 4: The Structure of the Model Development and General Flow of the Simulation Process [10]

The simulation model developed by Jones predicts the hydrodynamic and contact loads fairly accurately and the values obtained are realistic. The model is however unable to explain the large loads that lead to the forward bending of the blades.

Another limitation is that it cannot correctly model the impact condition where the ice blocks bounce against the blades without coming in contact with the leading edge. However, the effect of these loads on the structural integrity of the blades is significantly less.

2.6 Soininen H., 1998

Soininen [11] analyzed only the contact loads during the propeller–ice interaction and did not include the non–contact hydrodynamic loads in his model. The research was limited to the open propellers and only milling type of contact was investigated and the crushing type of contact was kept outside the scope of his work. Soininen laid more importance on the milling load on the back side of the propeller blade as the full scale and laboratory tests indicated that the maximum loads

bend the blade backwards under normal operating conditions. The schematic representation of the simulation model and the approach used by Soinen is shown in Figure 5.

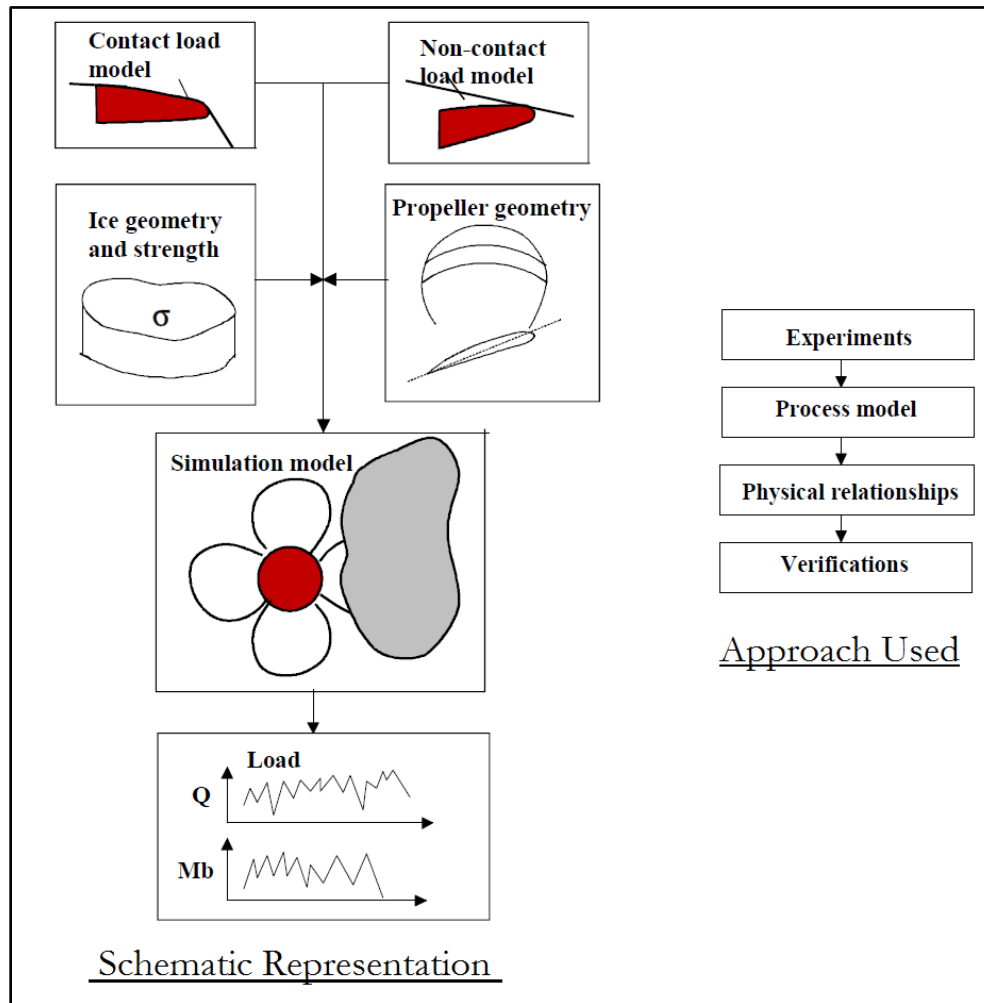


Figure 5: Schematic Representation of the Simulation Model and the Approach Used [11]

The experiments that preceded the development of the model were performed by Soinen et al [12, 13]. In these experiments, the pressure distribution along the propeller blade profile that impacted the ice was measured. The effect of different parameters, like angle of attack, advance velocity of the propeller, temperature of the ice, width of the cut made by the propeller in the ice, grain direction of the ice, etc., on the pressure distribution was thoroughly analyzed.

Based on the test results obtained, the blade–ice contact process model was developed. The model was developed for the case when the orientation of the ice grains is same as the propeller radius. Moreover, the contact loads were based on the quasi–static contact geometry between the ice block and the propeller blades as the pressure distribution was developed for a series of the time steps in a quasi–static way along the blade profile.

Although the process model was able to predict the correct shape of the pressure distribution along the blade profile with respect to the experiments carried out, the model was not however, able to

distinguish the transition from the spalling/chipping of ice due to the milling and the localized crushing. Moreover, the modeling of the large loads that bend the propeller blades backwards could not be accurately done by this model.

2.7 Wang J., 2007

Wang [4, 5] performed a series of model tests on the podded propellers and analyzed their interaction with ice. The main aim of the research was to develop a numerical method to predict the ice loads on the propeller using the combinations of the Panel method and empirical formulations. The Panel method was used to calculate the non-contact hydrodynamic loads on the propeller blades and the empirical formulae were used to calculate the contact loads such as ice milling. The results obtained were in good agreement with the experimental tests described in the same paper.

The earlier researchers divided the loads on the propeller into two types, contact loads like milling and crushing of ice, and non-contact loads or hydrodynamic loads. Wang however, divided the loads into three types;

- Separable Hydrodynamic Loads: These are the loads on the propeller due to the open water.
- Inseparable Hydrodynamic Loads: These are the loads on the propeller due to the blockage effect, proximity effect and cavitation due to the ice.
- Contact Loads: The contact loads like the milling are due to the physical contact between the propeller and the ice.

The Inseparable Hydrodynamic Loads and the Contact Loads are together called the Ice related Loads.

The Separable Hydrodynamic Loads are easy to evaluate in ice-free water. However, in order to distinguish between the Inseparable Hydrodynamic Loads and Contact loads, milling experiments of the ice in air were carried out. The results of the ice milling in air were not useful as there was excessive vibration resulting in a lot of noise in the measured values.

2.8 Bach C., 2017

In order to solve the problems associated with the milling of the ice in air to calculate the pure contact loads, Bach [14] performed the ice milling in air at HSVA in Hamburg. An ice feeding device was built so that problems of the vibration during the milling of the ice can be reduced. A schematic diagram of the ice feeding device is shown in Figure 6.

The model tests were carried out using a podded propeller with model sea ice. The model ice was produced according to the HSVA's standard procedure as given by Evers and Jochmann [15]. No numerical simulation model was developed by Bach to obtain the values of the contact loads theoretically.

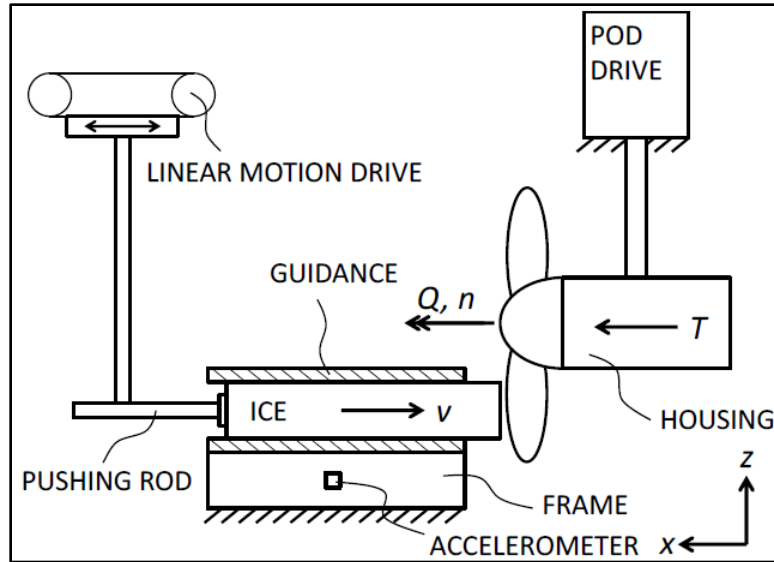


Figure 6: Schematic Representation of the Ice Feeding Device [14]

In his paper, Bach classifies the impact of the propeller blades with ice into two types;

- **Type A:** In the “type A” impact, the blade impacts the top surface of the ice sheet resulting in the milling and crushing of the ice. The granular layer at the top is crushed and the ice chunks are torn apart from the main sheet. The stresses on the blades are higher, followed by the high values of thrust and torque on the propeller shaft.
- **Type B:** In this case, there is not much contact with the top surface of the ice sheet but the blades scrape a thin layer of ice from the face of the sheet facing the propeller. No chunks of ice are generated as the ice sheets are slowly sheared away. The values of thrust and torque are lower than the “type A” impacts.

The major problem with the milling of ice in air was that the ice feeding device was not stiff enough to eliminate the vibrations especially when the hard ice was used. Although there were vibration isolators present in the ice feeding device, the vibrations could not be completely eliminated especially towards the end of the milling of the ice floe.

The experiments carried out in the present thesis report used the modified version of the same ice feeding device. In the new design, the guiding mechanism was improved and the ice feeding device made very rigid to eliminate the vibrations especially when hard ice was milled.

2.9 Other Approaches

The abovementioned thesis, publications and research articles were the ones that were studied in greater depth to understand the current state of the art in the field. Moreover, several other research articles on the subject were referred to get a better grasp of the subject-matter. They have been described in lesser detail below.

Okamoto et al, 1981 [16, 17] carried out the ice impact and ice milling model tests with 4 bladed Ni–Al–Br (Nickel–Aluminum–Bromide) propellers. They also carried out the statistical loading tests and

also performed finite element analysis. Ice blocks were prepared using saline water in paraffin wax blocks. The first report [16] describes in detail the ice impact and ice milling model tests and the second report [17] describes the behavior of stresses developed due to the ice loads in both the fixed pitch and controllable pitch propellers. The main aim was to obtain the data so that the correct scantling of the propellers for ice breaking merchant ships can be developed.

Chernuka et al, 1989 [18] performed finite element analysis to understand the propeller–ice interaction in a better way. They did studies on the contact mechanics and found that during high loading rates the ice was subjected to micro–cracking. They analyzed 2D ice indentation and milling problems and developed a program to determine the loads due to the propeller–ice interactions.

Bose et al, 1998 [19] developed an interaction equation that linked the main limit states that are to be applied at the design point. This limit state analysis for the design of the propeller blades takes into account the extreme hydrodynamic loads (both mean and oscillating) and ice loads (both contact and non–contact/ inseparable hydrodynamic loads). Four limit states were identified; elastic limit state, fatigue limit state, ice loading limit state (under normal operation conditions) and exceptional load limit state. The last two limit states are considered for the ice–class propellers in addition to the first two limit states. The exceptional load limit state is the one where the propeller stops rotating while the ship moves forward as the propeller is rammed into a massive ice formation.

Varma, 2000 [20] developed a numerical model using the existing empirical results of propeller–ice interactions under normal operating conditions which he further refined to predict the loads on the propeller under extreme operating conditions. To verify the results from the numerical model, a series of model tests were performed at high speeds using R–Class propellers and model ice. The test results depicted significant variation due to different modes of ice failure. However, all the modes followed a similar trend; the forces and moments increased linearly with the depth of indentation and were independent of the advance velocity of the propeller.

Norhamo et al, 2009 [21] took into consideration the milling and crushing of ice independently as well as together. The distribution of the ice loads on the propeller blades was derived from the extreme loads that were predicted by the available design models and methods (analytical, numerical, finite element, etc.). A strength assessment using both static and dynamic loads of the essential components of the propeller was done. These include blades, blade bolts & shear pins and the hub & pitch mechanism which further consists of servo cylinder, blade bearing, crank pin, side block, retaining wall and push–pull rod.

Pengfei et al, 2015 [22] developed an advanced 3D unsteady panel method for the design and the optimization of the polar class propellers. They found out that for all the blade sections, the out of plane bending moment resulted in the stress that was much higher than the stress due to the in–plane bending moment and the spindle torque.

Tsarau et al, 2016 [23] developed a numerical model that predicts the propeller–flow velocities, hydrodynamic forces and integrates the equations of motion of the ice cover. The numerical model was calibrated using the experimental results of the full–scale tests. The numerical model was also used to analyze the propeller–wash effect on the level ice. Semi–empirical formulae were used to

model the effect of the propeller on the ice fragments. The experimental results from the full scale tests were in coherence with the results obtained from the numerical model.

Polić et al, 2016 [24] used the bond graph method for modeling the propulsion system exposed to transient ice load. Dynamic torque and angular velocity response of all the links in the propulsion mechanism was simulated. The approach of the authors was similar to that of Jagodkin [6]. The main focus was not the stresses developed on the blades of the propeller due to the ice loads, but the additional torque and thrust produced in the propeller shaft. However, their research was much more detailed and advanced than Jagodkin in the sense that they analyzed the effects of the propeller–ice interaction on the complete propulsion machinery, including the propeller shaft, bearings, engine crank shafts, piston and cylinders etc.

Ye et al, 2017 [25] considered the properties of the propeller and the ice separately. They treated propeller blades as a rigid body and the ice as an elastic brittle material like glass and simulated the brittle failure for ice during the interaction with the propeller. Moreover, a continuous detection algorithm was used by them to detect the contact area between the blades and the ice particles. The numerical method used for developing the numerical simulation tool was based on the peridynamics. Although the results obtained were acceptable, the numerical model ignored the coupling motion of the propeller and the ice block in water. Furthermore, they assumed that the blades of the propeller are totally rigid and undergo no deformation at all on coming in contact with the ice particles. This however, is not a strictly valid assumption and is one of the sources of error in the theoretical calculations.

2.10 Class Rules

Apart from the research papers, theses, etc. an investigation was also done into the existing class rules for the ice-going vessels. Some of them have been mentioned below:

- Design of Propeller and Propeller Shaft, Det Norske Veritas AS [26].
- Propulsors in Ice, Bureau Veritas [27].
- Propeller Strength Assessment for Ice Class Ships, American Bureau of Shipping [28].
- Propulsion and Maneuvering Machinery for Vessels Operating in Low Temperature Environments, American Bureau of Shipping [29].
- Polar Class Ships and Ice Class Ships, Nippon Kaiji Kyokai (Class NK) [30].
- Requirements Concerning Polar Class, International Association of Classification Societies (IACS) [3].

Chapter 3

THE ICE-PPB

The primary objective of this chapter is to describe the numerical simulation tool Ice-PPB. In this chapter the various modules of the tool, the algorithm and the numerical calculations that help it to calculate the hydrodynamic and ice loads on the propeller will be discussed.

3.1 The Coordinate System and Conventions

In order to better understand the algorithm and the numerical calculations of the code Ice-PPB, it is imperative on the part of author to first describe the coordinate system and the various conventions used in the code and the report.

Consider Figure 7 shown below. The propeller is rotating about the x-axis with positive direction being towards the downstream of the propeller (out of the paper).

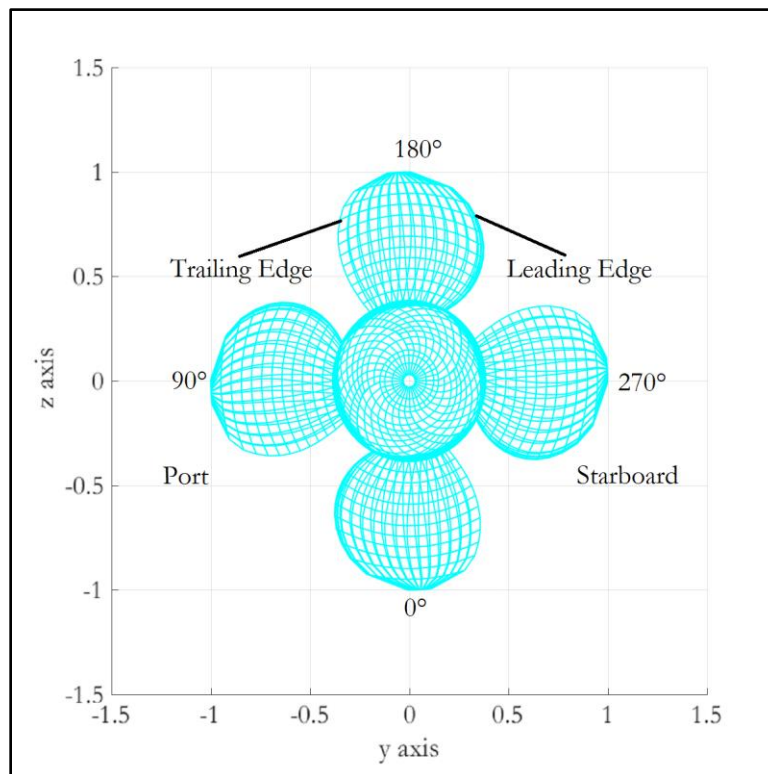


Figure 7: The Coordinate System and Conventions

As a result, the surface of the propeller on the suction side has a negative x component of the normal vector and the surface of the propeller on the pressure side has a positive x component of normal vector.

The y -axis is horizontal and parallel to the free surface of the water and the z -axis is vertical and perpendicular to the free surface of the water. The y -axis is positive towards the starboard side and negative towards the port side. The z -axis is positive in the upward direction and negative in the downward direction.

On the propeller disc, the zero degree is at the bottom, 6 o' clock position and the angle moves in a clockwise fashion when viewed from the pressure surface.

3.2 The Ice-PPB Algorithm

The Figure 8 below shows a simplified algorithm of Ice-PPB. The code is written using the MATLAB [31] software. It essentially consists of 7 modules as mentioned below.

a) **The Input Data Module:** The input data module starts from Step 1 to Step 3 as shown in Figure 8. The purpose of this module is to start the program Ice-PPB and prompt the user to input the data that is necessary for performing the calculations. Furthermore, it asks the user to select the type of floe impacting the propeller, Planar or Sectoral. The input data is then accordingly sent to the Planar Floe or Sector Floe Module respectively.

b) **Floe Module:** The floe module consists of two types of modules, Planar Floe Module and Sector Floe Module. These modules calculate the loads on the propeller in two different conditions. In the planar module, the loads are calculated when a planar sheet of ice is fed into the propeller as shown in Figure 9. This is usually the standard practice when experiments are performed on propeller-ice interaction.

However, in real life scenarios there are scattered ice particles that come in contact with the propeller at different locations of the propeller disc. This kind of situation is also simulated by the code by using the sector floe module. In the sector floe module, an ice particle comes in contact with the propeller disc in a certain region (or sector) as shown in Figure 10.

The floe module forms the backbone of Ice-PPB. It processes the input data from the Input Data Module, writes the wake files (Steps 6-7) and sends the processed data as an input to the Hydro-PPB Module. These wake files will be described in detail in the coming pages.

The Floe Module receives the hydrodynamic data from the KT & KQ Hydro module. Furthermore, the Floe Module uses a detection algorithm to determine the panels of the propeller that will be in contact with the ice floe and sends the data to the Ice CP & TW module (Steps 16-18). It also generates a video of the milling of ice by the propeller blades and highlights the panels of the propeller that are in contact with ice during milling.

Finally, the Floe Module receives the data from the KT & KQ Ice module and Polar Class Module and saves all the data of the simulation on the hard drive for future use and then terminates the program (Steps 27-28).

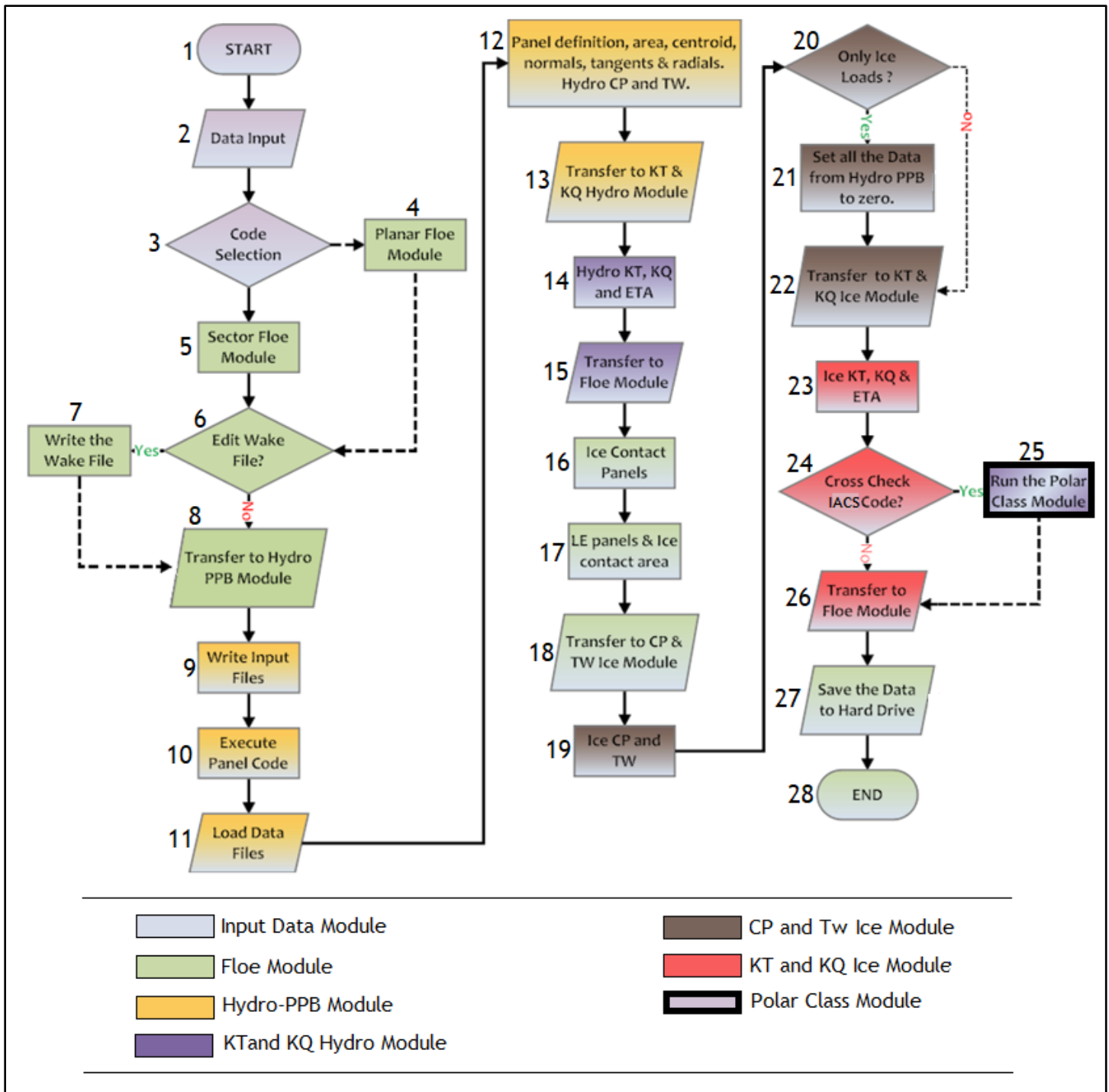


Figure 8: Simplified Algorithm of Ice-PPB

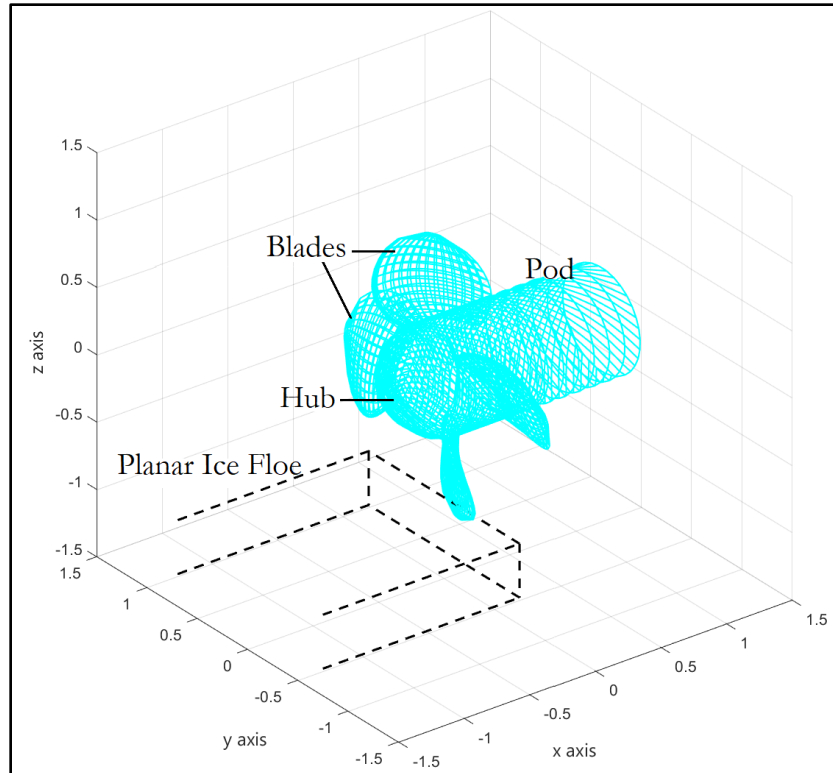


Figure 9: Propeller with Planar Ice Floe

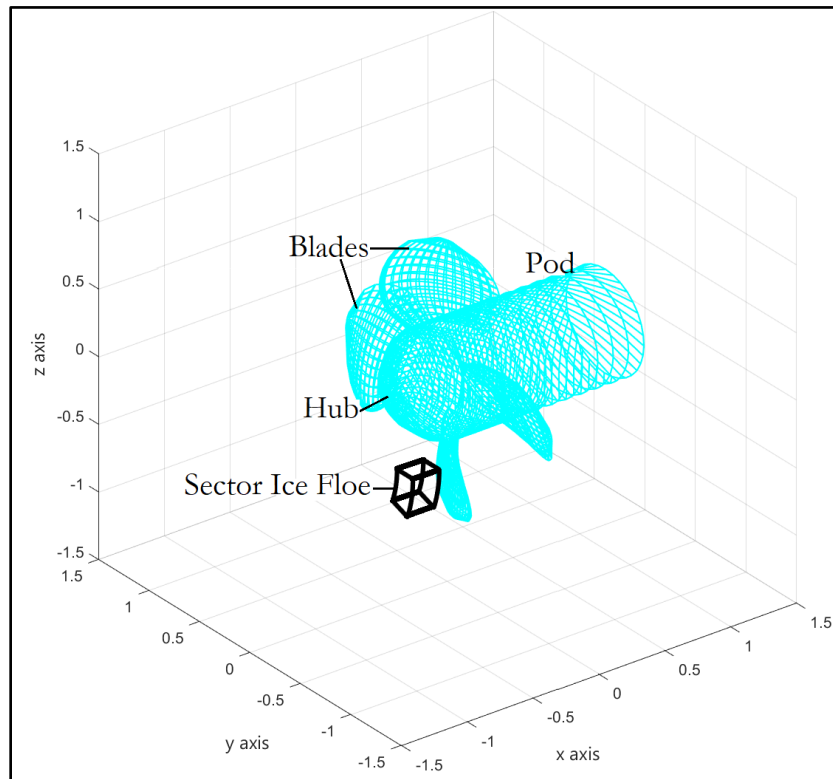


Figure 10: Propeller with Sector Ice Floe

c) **Hydro-PPB module:** The Hydro-PPB module (Steps 9–13) calculates both the separable and inseparable hydrodynamic loads. It receives the input files from the Floe Module and calculates the hydrodynamic loads using the hydrodynamic load data from the existing simulation tool from HSVA called PPB. In the coding algorithm of Ice-PPB, the PPB was made part of Ice-PPB and it runs as a sub program of Ice-PPB and is not run separately or in parallel to Ice-PPB.

Using the data from PPB, the Hydro-PPB module determines the panels that form the propeller. It also calculates the centroid, area, normal, radial and tangential vectors of each panel. Moreover, it assigns the C_p (Coefficient of Pressure) and T_w (Normalized Tangential Force per unit area) value obtained from PPB to each panel and sends all this data to the KT and KQ Hydro module. Using the values of C_p and T_w , the KT and KQ Hydro module calculates the hydrodynamic loads acting on the propeller for a given value of Advance Coefficient (J).

d) **KT and KQ Hydro Module:** The KT and KQ Hydro module (Steps 14–15) receives the hydrodynamic data from the Hydro-PPB module and using this data it calculates the thrust and torque generated on the propeller due to the hydrodynamic loads. The thrust coefficient (K_T), torque coefficient (K_Q) and the efficiency (η) are also calculated. It sends all the data to the Floe Module for further processing.

e) **Cp and Tw Ice Module:** The C_p and T_w Ice module (Steps 19–22) receives the input data from the Floe Module. Using the information from the Floe Module, the C_p and T_w Ice module calculates the ice loads acting on the panels that come in contact with ice and calculates the additional values of C_p and T_w acting on those panels.

The C_p and T_w due to the ice loads are calculated using the empirical formulae given by Wang [4, 5] which will be explained in the coming pages of the report. The ice data is then transferred to the KT and KQ Ice module that calculates the ice loads acting on the propeller.

Moreover, the C_p and T_w Ice module provides an option to calculate the ice loads separately or in combination with the hydrodynamic loads calculated previously. This additional functionality is very helpful during the calibration phase as it facilitates the calibration of the ice and hydrodynamic loads separately as well as together.

f) **KT and KQ Ice Module:** The KT and KQ Ice module (Steps 23–26) receives the ice data from the C_p and T_w Ice module and using this data it calculates the thrust and torque generated on the propeller due to the ice loads. The thrust coefficient (K_T), torque coefficient (K_Q) and the efficiency (η) are also calculated. It sends all the data to the Floe Module for storage and display of the results.

g) **Polar Class Code Module:** This module (step 25) calculates the maximum loads permissible for the propeller using the data it receives from the Floe Module, like propeller diameter, number of blades, etc. and calculates the loads for all the 7 classes (PC1–PC7) as mentioned in the IACS polar class code [3]. The data is sent back to the Floe Module, that compares this data with the one calculated by the numerical code and verifies whether the loads are similar or not.

3.3 Input Data

The input data given to the code is divided into two parts viz. the hydrodynamic data and the ice data as explained below.

3.3.1 Hydrodynamic Data

The Table 1 below lists the various parameters that are required as an input to Ice-PPB for the calculation of the hydrodynamic loads.

Table 1 : Hydrodynamic Input Data

S No	Input Data	Value
1.	Advance Coefficient	User Specified
2.	Full scale diameter of the propeller	User Specified
3.	Full scale diameter of the hub	User Specified
4.	Full Scale Propeller RPM	User Specified
5.	Propeller Blade Number	User Specified
6.	Scaling Factor	User Specified
7.	Expanded Area Ratio	User Specified
8.	Pitch to Diameter Ratio (P/D) at 0.7 R	User Specified
9.	Thickness at 0.7 R in Full Scale	User Specified
10.	Number of Harmonics (n)	Obtained after convergence of output values
11.	Number of turn steps (k)	Obtained after convergence of output values
12.	Number of turns in the propeller race (p)	Obtained after convergence of output values

Out of the 12 parameters mentioned in the above table, 9 parameters are to be input by the user and rest 3 parameters depend on how accurate the solution is required in a given time frame. The value of these 3 parameters is determined by performing the convergence study as explained in section 5.1.1. From this study, the values obtained for these 3 input parameters ensure accurate results in the shortest time possible.

The number of harmonics (n) instructs the code to calculate the influence of all the harmonics from 1 to n of the propeller rotation frequency. Higher the value of n , more accurate is the result in terms of time resolution albeit at the cost of a higher computational time. Moreover, excessively high values of n (greater than 8), increase the numerical errors.

The number of turn steps (k) instructs the code to generate a paneled vortex wake structure at k steps as the propeller rotates from 0° to 360° . If only the open water loads are to be calculated, then there is a simpler shed vortex wake structure and in that case the use of smaller value of k is justified. However, due to the presence of the wake field, the shed vortex structure includes span-wise directed elements and in order to calculate the loads at different positions of the propeller blades, more turn steps between 0° to 360° are required. The higher the number of turn steps, the more accurately is the effect of wake field captured and more accurate are the results obtained.

The number of turns in the propeller race (p) instructs the code to set up the turn steps structure mentioned above for p turns and accordingly calculate the hydrodynamic influence of the propeller up to p turns downstream. For a small pitch propeller, the value of p should be high and it should be low for a high pitch propeller to ensure that the horizontal distance downstream is similar. Figure 11 below shows the paneled vortex wake structure generated by the code for a 6 bladed propeller for 1 turn in the propeller race ($p = 1$) and 18 turn steps ($k = 18$), but only 9 turn steps are visible and the rest 9 are not visible in this view of Figure 11.

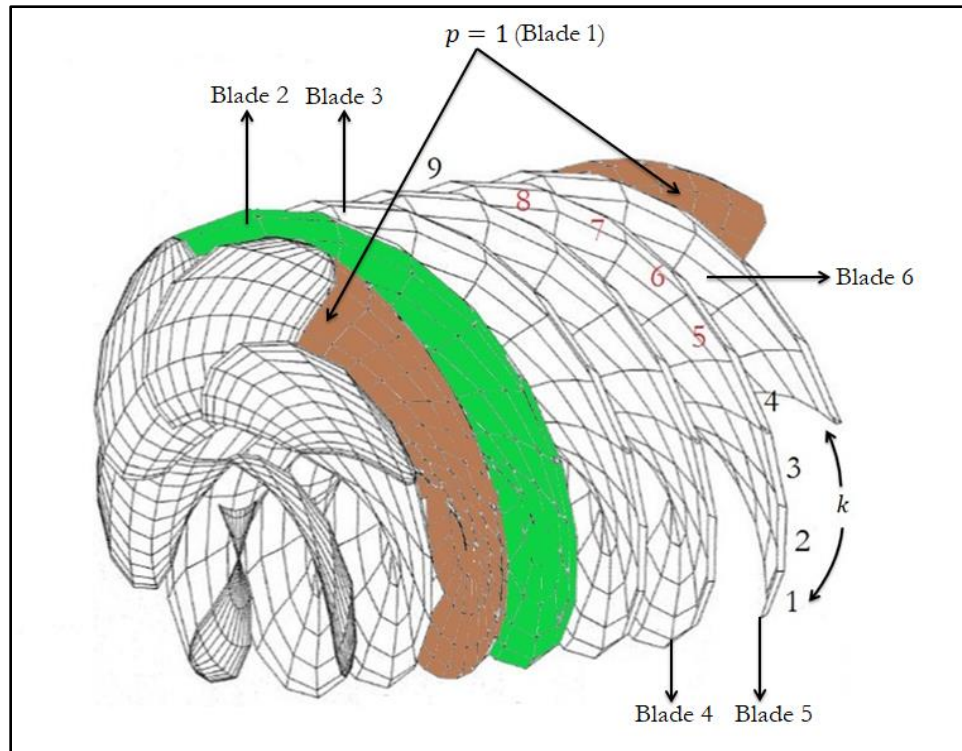


Figure 11: Paneled Vortex Wake Structure (modified [32])

3.3.2 Ice Data

The Table 2 below lists the various parameters that are required as an input to Ice-PPB for the calculation of the ice loads. All the data mentioned in the Table 2 is for the model scale.

Table 2 : Ice Input Data

S No	Input Data	Value
1.	Ice Compressive Strength	User Specified
2.	Ice Density	User Specified
3.	Water Density	User Specified
4.	Length of Ice Floe	User Specified/Planar Floe only
5.	Width of Ice Floe	User Specified/Planar Floe only
6.	Distance between top surface of ice floe and propeller axis/ Depth of cut	User Specified/Planar Floe only
7.	Start angle of Ice Floe	User Specified/Sector Floe only

8.	Start radius of Ice Floe	User Specified/Sector Floe only
9.	End angle of Ice Floe	User Specified/Sector Floe only
10.	End radius of Ice Floe	User Specified/Sector Floe only
11.	Average Weighing Factor	Obtained from Calibration
12.	Maximum Weighing Factor	Obtained from Calibration
13.	Empirical Factor for Crushing	Obtained from Calibration, dependent on ice properties.
14.	Empirical Factor for Shearing	Obtained from Calibration, dependent on ice properties.

Out of the 14 parameters listed above, the first 10 are to be specified by the user and the rest 4 are the empirical factors used by Wang [4, 5] in his empirical formulae to calculate the ice loads. The value of these empirical factors depends on the ice characteristics and is obtained after the calibration of the code is done. Further description is given in sections 3.6 and 5.2.

In addition to the hydrodynamic input data and the ice input data, the propeller geometry files are also required as an input. Additionally, the wake files are also needed as an input to Ice-PPB to calculate the inseparable hydrodynamic loads. The wake files are a set of files that contain the value of the wake velocities in axial, radial and tangential directions at a given radii and angles around the propeller disk. These wake files are generated by the code based on the input data given in Table 1 and Table 2.

In the coming pages, the wake field generated by the ice floes and the corresponding wake files generated by the code are explained in detail.

3.4 The Ice Wake Field

The modelling of the ice wake field in terms of the wake files consists of two parts, one is the determination of the velocity of water in the wake region and the other is the determination of the region around the propeller disc in which the wake effect will be observed. The two steps are explained below.

3.4.1 Determination of the Wake Velocity

The movement of the ice floes towards the propeller can be described in three stages as shown in Figure 12 [33]. During the approach phase, the ice floe gets into the propeller race and starts its motion towards the propeller disc. In the propeller race, due to the acceleration of the fluid, the relative axial velocity between the ice floe and the propeller increases leading to disruption of the fluid flow, producing an ice wake. This leads to the increase in the hydrodynamic loads on the propeller and these additional loads are called the inseparable hydrodynamic loads.

During the blockage phase, the ice floe is in the immediate vicinity of the propeller and the ice wake effect reaches its maximum value as shown in Figure 12. The ice wake (V_W) is almost equal to the ship speed (V_S) and as a result the velocity of the fluid entering the propeller or the advance velocity ($V_A = V_S - V_W$) is essentially zero, making the flow stagnant. This phenomenon is called the blockage effect. However, according to Bose [34], the advance velocity is not zero, but ≈ 0.01 times

the ship speed. This blockage model was also used by Wang [4, 5] and will also be used in this report. Finally, in the contact stage, the ice comes in the contact with the blades of the propeller leading to the milling of ice.

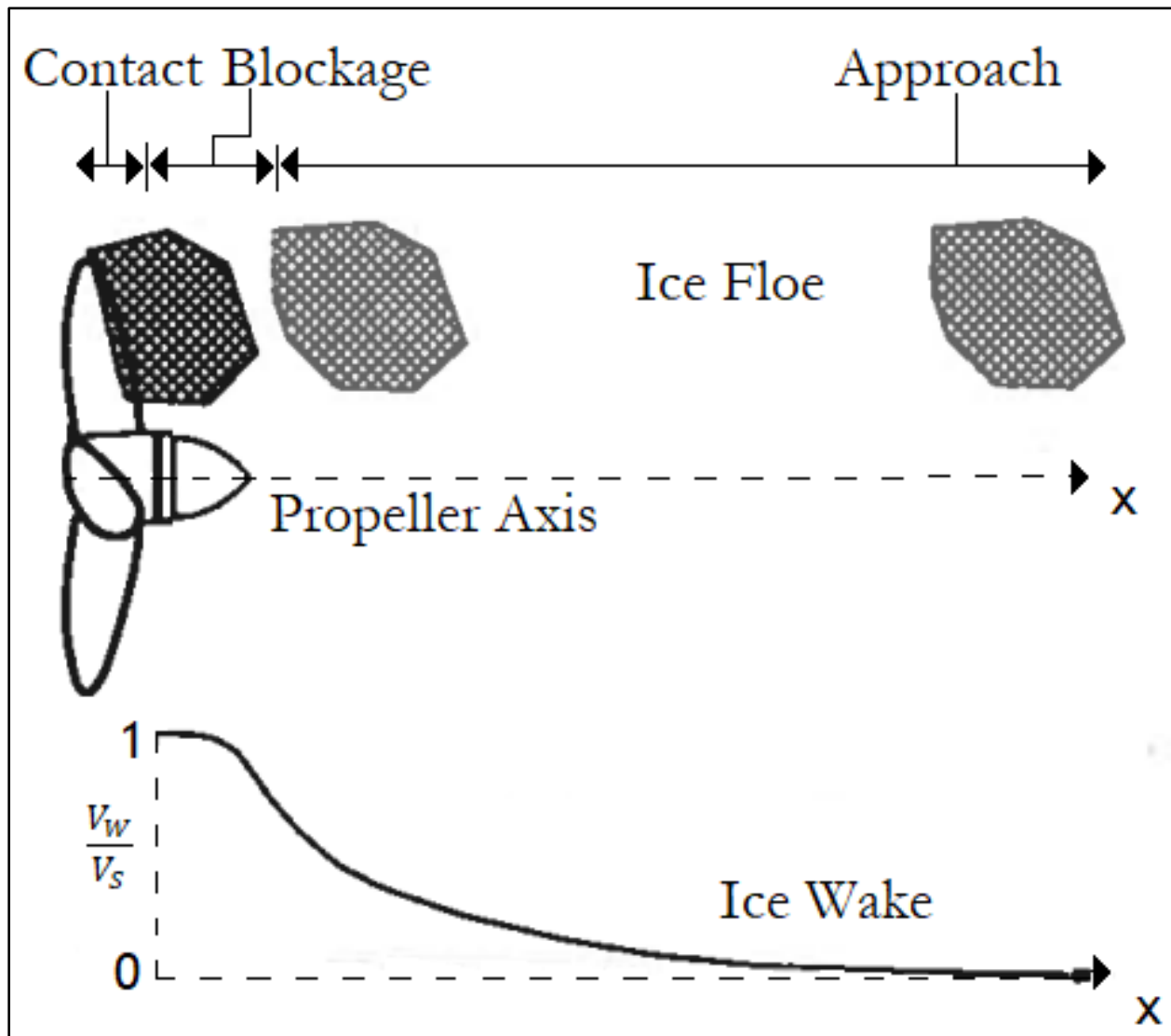


Figure 12: Three Stages of Propeller Ice Interaction (modified [33])

In Ice-PPB, this ice wake phenomenon was modelled by developing a wake file that contains values of the fluid velocity at different angles and radii around the propeller disc. In order to calculate the blockage effect accurately, the ice wake was calculated every 10° at 5 different radii of the propeller disc as shown in Figure 13 below. The values at the other radii and angles were obtained by interpolation.

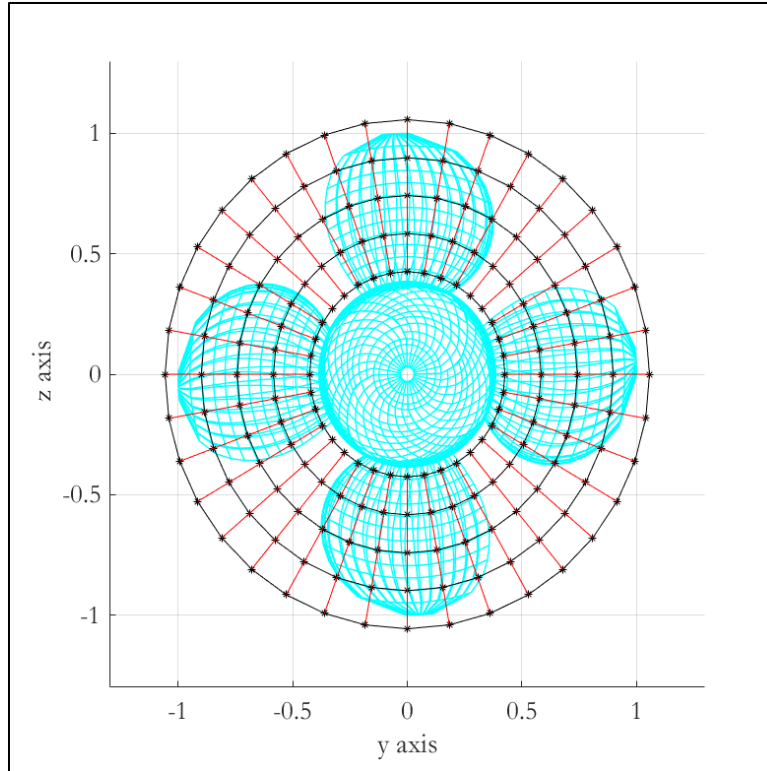


Figure 13: Grid for Calculation of Wake Field

3.4.2 Determination of the Wake Region

The ice wake is developed in the suction side of the propeller in the region containing the ice floe. In order to calculate the effect of the ice wake it is essential to exactly locate this region when the ice floe moves towards the propeller. The determination of the wake region is done in two different ways for the planar and sector ice floe.

a) Planar Ice Floe: For the planar ice floe (which is generally used in experiments), the wake region changes with the change in the depth of cut and the radius of the propeller. For calculating the wake region in terms of angles and radii in order to conform to the format of the wake file, we first define the milling angle (α_m), which gives us the idea about the start and stop angle of the wake region.

Consider Figure 14 shown below. The milling angle (α_m) is the angle during which the blades of the propeller cut through the ice floe. The wake region is a sector whose sector angle is equal to the milling angle; the outer radius is equal to the radius of the propeller (R) and the inner radius is the difference between the propeller radius and the depth of cut (d). The wake region starts at $\theta_1 = 360 - \alpha_m/2$ and ends at $\theta_2 = 0 + \alpha_m/2$. This is in accordance to the angle convention shown in Figure 7.

Using the basic trigonometric relationships, we can calculate the milling angle as,

$$\alpha_m = 2 \times \cos^{-1} \left(\frac{R-d}{R} \right) = 2 \times \cos^{-1} \left(\frac{h}{R} \right)$$

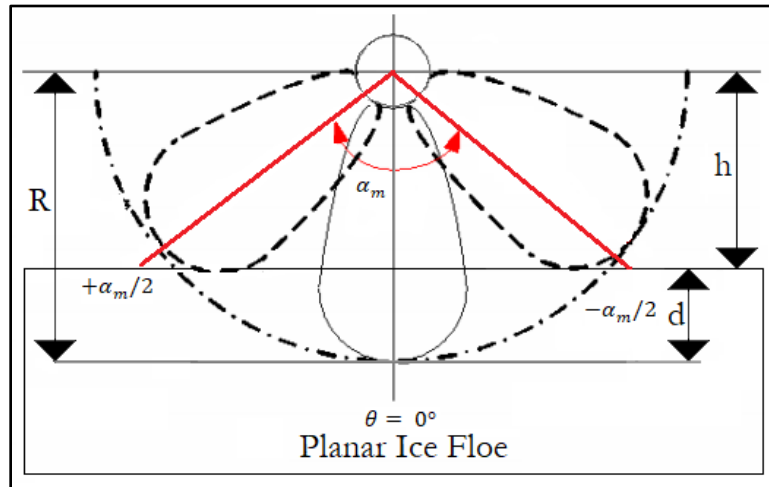


Figure 14: Representation of the Milling Angle (modified [4, 5]).

This wake region (shown in grey) is calculated by the Floe Module of Ice-PPB and is plotted along with the planar ice floe and the propeller as shown in Figure 15. In Figure 16 we can see the normalized advance velocity, which is the ratio of advance velocity and ship speed ($V'_A = V_A/V_S$) plotted around the propeller disc. In the wake region shown in Figure 15, we can see that the normalized advance velocity is close to zero (Figure 16). The reduced velocity in this region forms the ice wake field and leads to the increase in the hydrodynamic loads on the propeller.

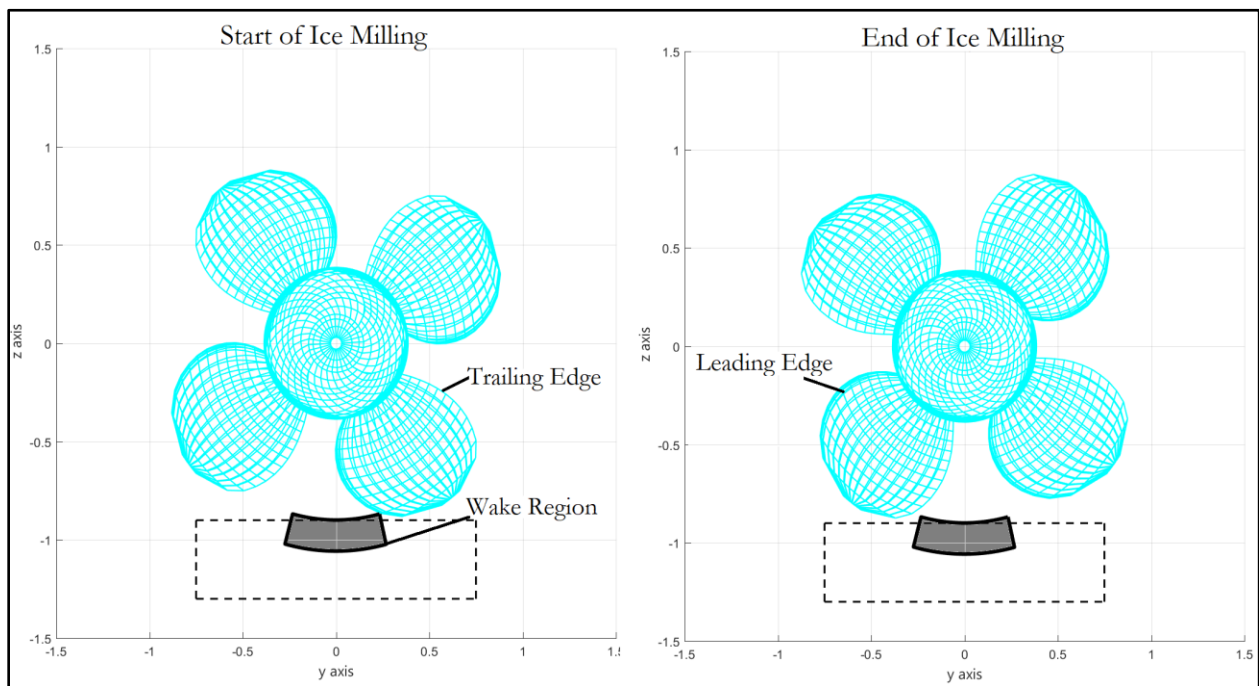


Figure 15: Wake Region along with the Propeller for Planar Ice Floe

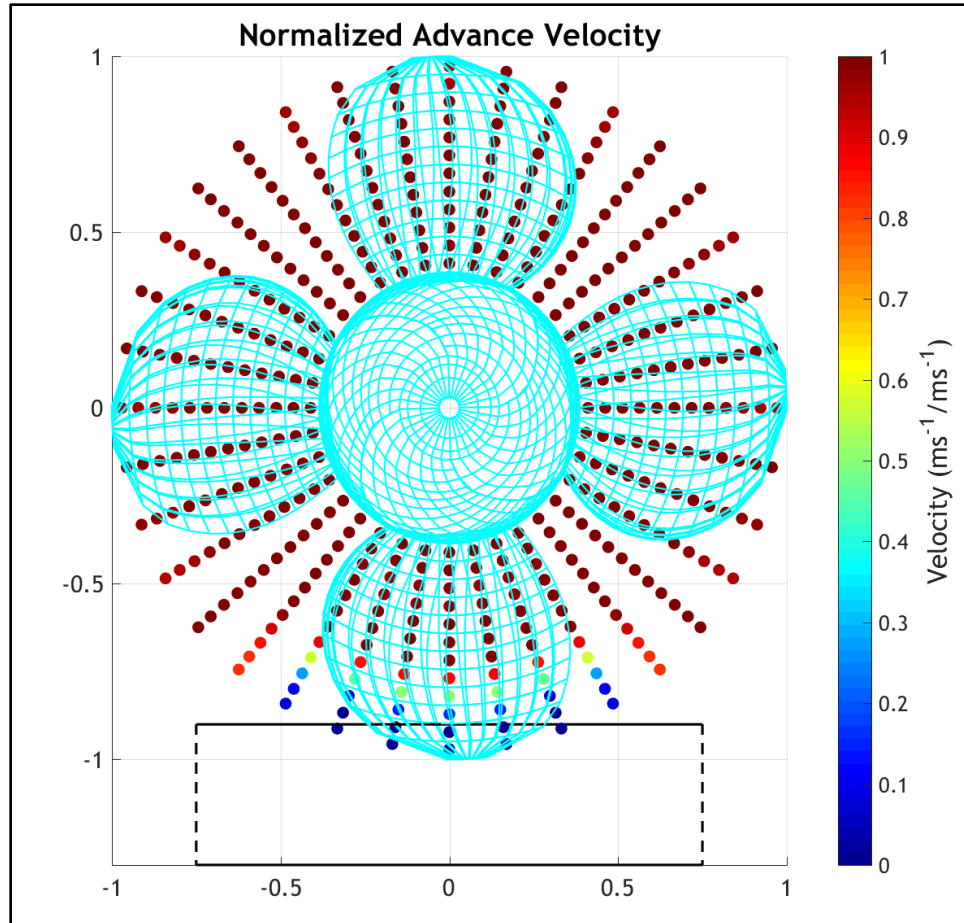


Figure 16: Plot of the Normalized Advance Velocity around the Propeller Disc for Planar Ice Floe

b) Sector Ice Floe: The wake region for a sector ice floe is quite simple to calculate as the wake is in the same region as that of the ice floe. The sector ice floe is specified by the two angles and two radii, and these angles and radii also determine the wake region.

Figure 17 shows the wake region (shown in grey) and the start and end of the milling. Figure 18 shows the variation of normalized advance velocity in the wake region. From Figure 18 we can see that the normalized advance velocity (V'_A) or the advance velocity (V_A) (as ship speed (V_S) is constant) approaches zero due to the presence of the ice floe leading to the increase in the hydrodynamic loads.

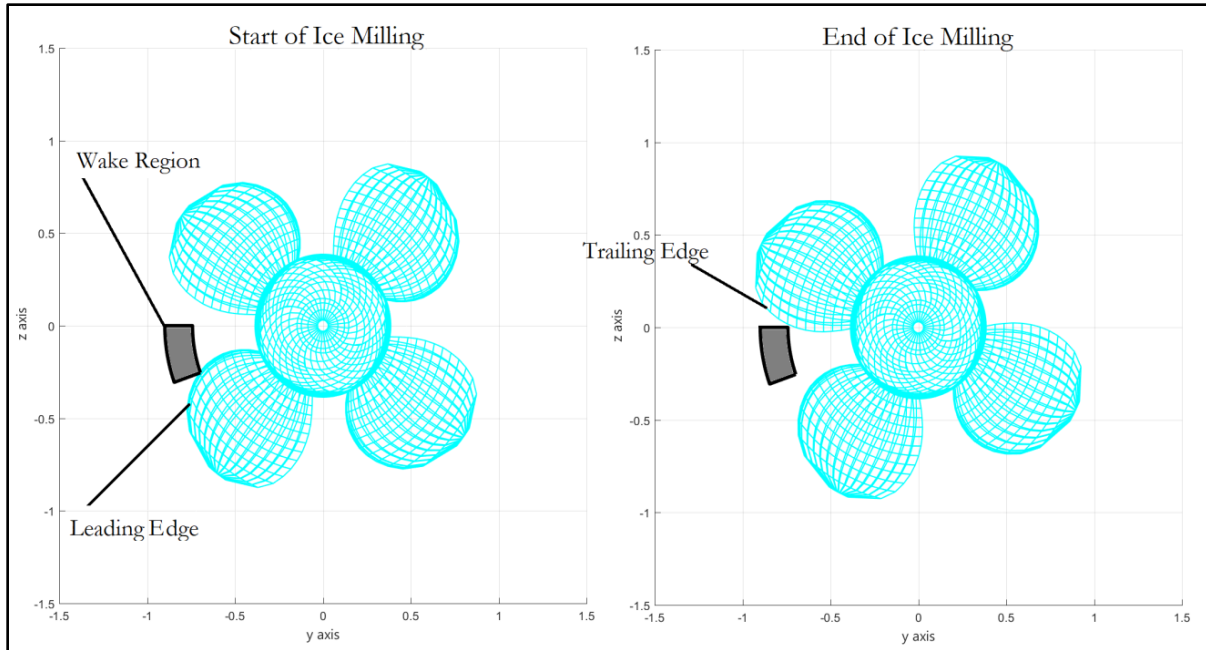


Figure 17: Wake Region along with the Propeller for Sector Ice Floe

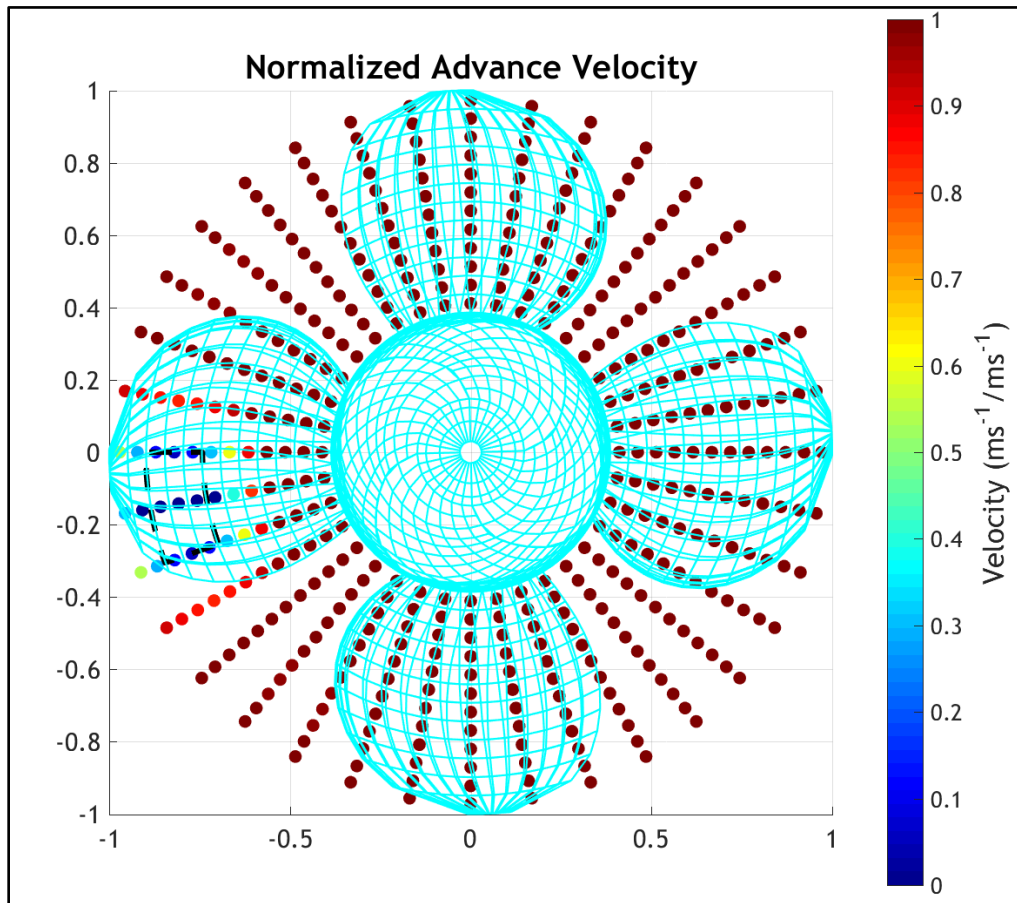


Figure 18: Plot of the Normalized Advance Velocity around the Propeller Disc for Sector Ice Floe

3.5 Calculation of the Hydrodynamic Loads

The separable and inseparable hydrodynamic loads are calculated by Hydro-PPB module. Hydro-PPB module receives the input data from the floe module and using this input, the propeller geometry files and the wake files generated in the previous step (section 3.4), it runs the PPB code. When the PPB is executed, it generates five types of output files as mentioned below:

- a. **Point File:** It contains the x , y and z values of all the points that form the panels of the hub and the propeller.
- b. **Panel File:** It contains the list of all the panels and for each panel, the index number of the points forming the panel.
- c. **Cp file:** It contains the values of the coefficient of pressure to be applied on the panels defined in the panel file.
- d. **Tw file:** It contains the values of the normalized tangential force per unit area to be applied on the panels defined in the panel file.
- e. **Slipstream Velocity file:** This file contains the values of the induced velocity, wake velocity and advance velocity in the y - z plane at a given distance x (user specified) from the propeller disc.

Hydro-PPB receives the point files, panel files, Cp files and Tw files for all the turn steps specified by the user in Table 1. On this data, following functions are performed by Hydro-PPB for each turn step in a sequential order:

- a. Using the point file and the panel file from PPB, the panels are defined by the code. Each panel is a three dimensional quadrilateral surface i.e., all the four points that constitute a panel are not necessarily coplanar. This kind of geometry is called a skew quadrilateral.
- b. Once, the panels are defined and plotted, the code calculates the centroid, area, normal vector, tangential vector and radial vector of each panel using the basic geometry and trigonometric relationships.
- c. Finally, the Cp and Tw value from PPB is assigned to each panel by the code.

The detailed calculations and mathematics involved in the calculation of the centroid, area, normal, tangential and radial vectors of the panels have been omitted to keep the report short. They are explained in detail in Annexure 01 at the end of the report. All the data calculated by the Hydro-PPB module is then send to the KT and KQ Hydro module for the calculation of the thrust and torque acting on the propeller.

3.5.1 Calculation of the propeller torque and thrust

The KT and KQ Hydro module receives the data from Hydro-PPB module and using this data, the module calculates the 3 components of the force (f_x , f_y and f_z) acting on each panel of the propeller. The force f_x acts along the x direction and directly contributes to the thrust produced by the propeller. The forces f_y and f_z generate moments about the propeller axis and this moment directly contributes to the torque generated on the propeller shaft.

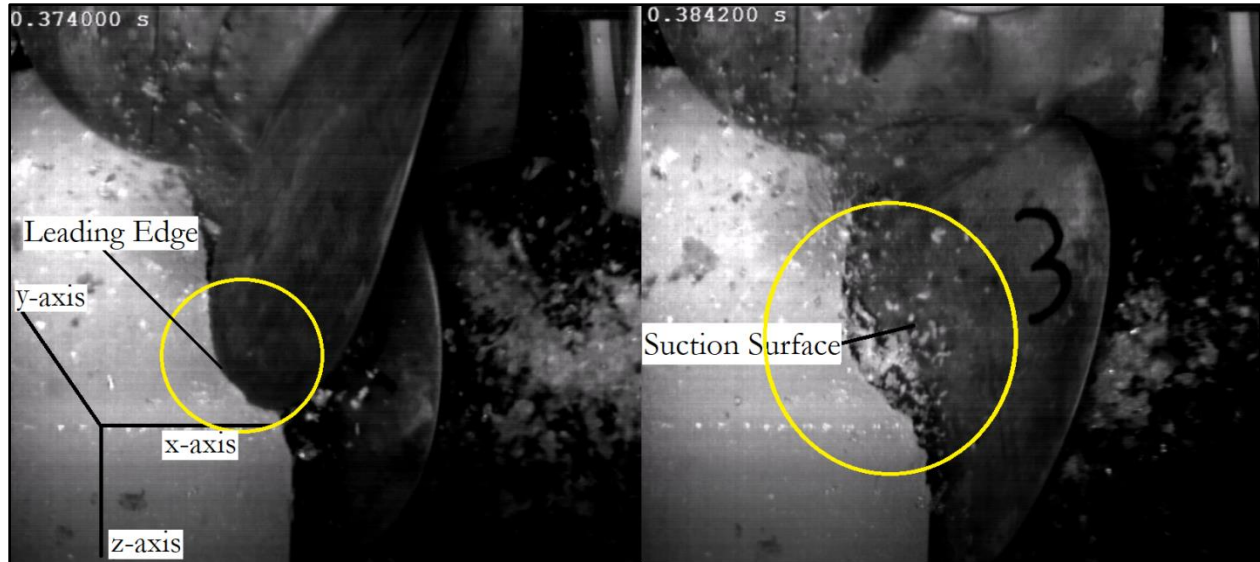


Figure 19: Crushing (Left) and Shearing (Right) of Ice during milling [32]

Wang [4, 5] developed separate empirical formulae for the crushing and shearing of ice and used separate empirical factors in each case. The pressure on each panel is given as:

$$P_{crushing} = w \times EFC \times S_{ice} \quad (1)$$

$$P_{shearing} = S_{ice}/EFS \quad (2)$$

$$C_p = P_{crushing} / (0.5 \times \rho \times (\omega R)^2) \quad (3)$$

$$T_w = P_{shearing} / (0.5 \times \rho \times (\omega R)^2) \quad (4)$$

Where,

w = Empirical weighing factor

EFC = Empirical Factor for Crushing

EFS = Empirical Factor for Shearing

S_{ice} = Compressive Strength of ice

ρ = Density of water

ω = Angular Frequency of the propeller rotation

R = Radius of the propeller

The additional C_p and T_w values calculated in the above equations are added to the suitable panels and are used to calculate the Ice Loads on the propeller. These calculations are done in the C_p and T_w Ice Module of Ice-PPB. The additional C_p and T_w data is sent from the C_p and T_w Ice Module to the KT and KQ Ice Module for the calculation of additional torque and thrust developed on the propeller due to ice interactions. The detailed calculations are mentioned in the Annexure 01 of this report.

The compressive strength of the ice is given as a user input as shown in Table 2. The two empirical factors i.e., EFC and EFS vary from simulation to simulation. These empirical factors are dependent

on the ice properties. Thus, as the ice properties change, the value of these factors also changes. These empirical factors are explained in detail in chapter 5.

The empirical weighing factor (w) has an average or base value of 1 and a maximum value of 6 [4, 5]. The maximum value is used to calculate the pressure on the leading edge panels, which undergo severe impact loading during the milling of ice. The average value of 1 is used to calculate the pressure on the suction panels which have a considerable small loading during the ice milling.

Moreover, not all the suction panels present in the ice field (region of the propeller disc in which ice is present) come in contact with the ice floe as the front face (y - z plane) of the floe is not parallel to the suction surface of the blades due to the non-zero pitch angle. As a result, as the ice floe moves towards the rotating blades of the propeller, different parts of the suction surface come in contact with the floe at different blade positions.

In order to correctly simulate this effect, a detection algorithm was developed that calculates the suction side panels in contact with the floe for each turn step (k). This effect is termed as the shadow effect (some parts of the blade shadow out other parts and prevent them from contacting the ice floe) and the suction panels in contact with the ice floe are called shadow panels. The algorithm for the detection of the shadow panels is explained in the next section.

3.6.1 Shadow Effect

The shadow effect is a phenomenon that comes into existence due to the absence of the coplanarity between the front face of the ice floe and the suction surface of the propeller blades. For a propeller having a zero pitch angle, the blades are parallel to the y - z plane and the entire front face of the ice floe comes in contact with all the suction panels present in the ice field. However, in reality a screw propeller cannot have a zero pitch angle and thus, the shadow effect cannot be eliminated.

Due to the non-zero pitch angle of the propeller, some parts of the blade are closer to the ice floe than the others. The leading edge of the blade is closest to the ice floe and the trailing edge is the farthest. Since the propeller is right handed, the leading edge comes in contact with the floe first and hits it at an oblique angle as seen from the high speed footage (Figure 19). As the leading edge moves away, the suction surface then moves in front of the ice floe, some parts of the surface (ones towards the leading edge) being closer to the ice floe than the remaining parts. However, at the same time the ice floe also moves forward towards the propeller.

The propeller blades are rotating at a frequency of n (Hz) and the ice floe is moving towards the propeller at a velocity of V (m/s). In a given time interval Δt , the ice flow advances by a distance (d) towards the propeller and in the same time interval Δt , the blade of the propeller turns by an angle (θ). Thus,

$$J = \frac{V}{nD}, \quad d = JnD\Delta t, \quad \theta = 2\pi n\Delta t$$

Now, for a propeller with b number of symmetric blades, the angle traversed in one blade rotation (θ) is given as,

$$\theta = \frac{2\pi}{b}, \quad \Delta t = \frac{2\pi}{2\pi n b}, \quad d = J n D \frac{2\pi}{2\pi n b} = \frac{J D}{b}$$

Therefore, a suction panel at a particular radius (r) in the ice field will come in contact with the ice floe only when the sum of the x-coordinate of any one out of four points of the leading edge panel at the same radius (r), and the distance travelled by the ice-floe (d) is greater or equal to the x-coordinate of the any one out of four points of the suction panel. When this condition is met by a panel, it will come in contact with the ice flow and become a shadow panel. The shadow panels are shown in green color in Figure 20 below.

In Figure 20 below, the calculation of the shadow panels was done at a relatively small value of $J = 0.015$. As a result, the distance travelled by the ice-floe (d) was small and thus the number of shadow panels was less and they were situated very close to the leading edge. However, as the value of J is increased, the distance (d) increases and so does the number of the shadow panels. The variation of shadow panels with J values can be seen in Figure 21 below.

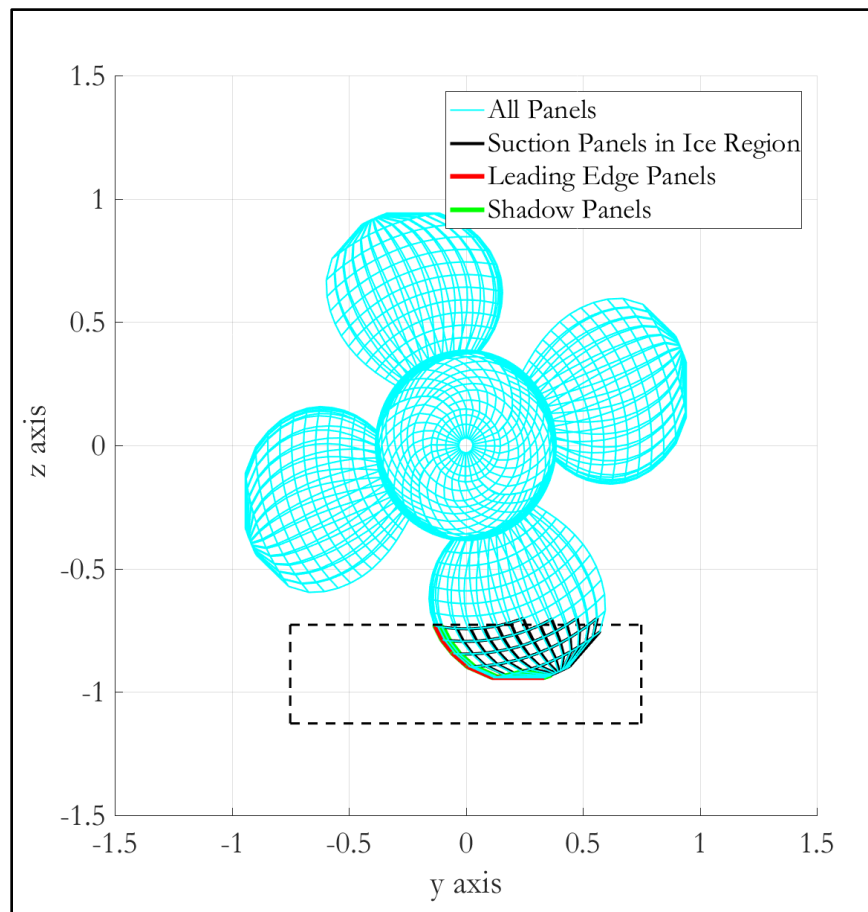


Figure 20: Shadow Panels

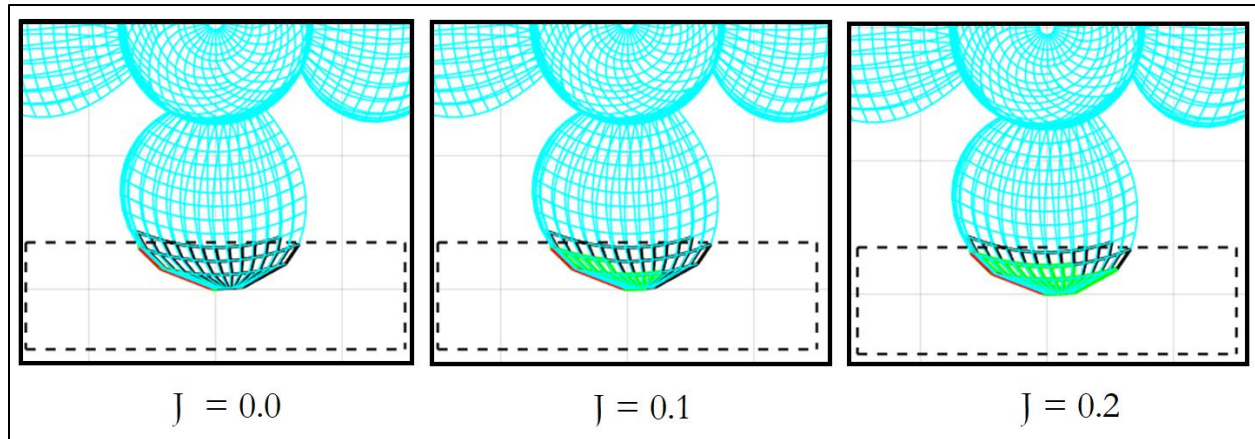


Figure 21: Variation of the Shadow Panels with Advance Coefficient

The leading edge panels receive the loads mainly in the tangential direction and contribute to the increase in the propeller torque during the ice milling. The shadow panels receive the loads mainly in the normal (x -direction) and thus contribute to the decrease in the thrust, as the direction of the thrust produced by the ice milling is from suction side to pressure side, which is opposite to the hydrodynamic thrust produced by the propeller.

In order to check the accuracy and precision of the code, a set of experiments was performed and the results from these experiments were used to calibrate the different aspects of the code like, viscous correction, empirical factors, etc., the details of which are provided in the chapter 5 of the report.

3.7 Polar Class Code

As mentioned in section 3.2, Ice-PPB also has a polar class module that calculates the maximum loads permissible on a propeller with a given scantling and thus verifies whether the loads are comparable or not. The equations for maximum thrust and torque on a propeller due to the ice loads as given by IACS [3] are mentioned in Annexure 02 at the end of the report.

Chapter 4

THE EXPERIMENTS

The code Ice-PPB is a numerical tool and uses a surface panel method to calculate the loads due to the propeller-ice interaction. The hydrodynamic loads are calculated using potential theory and ice loads are calculated using the empirical formulae.

In reality, we have viscous effects which are dominant at low values of Advance Coefficient (J) and most of the ice class propellers operate at low J values to avoid high stresses. Moreover, the ice loads are heavily dependent on the ice properties that change significantly from experiment to experiment. Thus, it is necessary to calibrate the tool and establish an accurate relationship between the ice properties and empirical factors and in order to do that several experiments were carried out.

As mentioned in section 1.3, three types of experiments were carried out so that the code could be individually calibrated for separable hydrodynamic loads, inseparable hydrodynamic loads and ice loads to increase its accuracy and reliability.

In order to calibrate the code with respect to separable hydrodynamic loads, the results from the code were compared with the experimental results from an open water test. For the ice loads, the results from the code were compared with the experimental results from the air milling of ice and finally, for the inseparable hydrodynamic loads the code was calibrated by comparing the results from the water milling, air milling and the open water test. In the coming pages, the three types of experiments and their results have been explained in detail.

4.1 The Propeller

The propeller used in the experiments is an ice-class propeller from the German ice breaker research vessel called Polarstern (*Pole Star*). It is essentially a controllable pitch podded propeller and its geometrical characteristics are listed in Table 3. A schematic representation of the same is shown in Figure 22. The model used for the experiments had a scale factor of 21.

Table 3: Geometrical Characteristics of the Polarstern Propeller [32]

S No.	Parameter	Full Scale Value	Model Scale Value
1.	Diameter	4200 mm	200 mm
2.	Hub Diameter	1617 mm	77 mm
3.	Pitch /Diameter Ratio at 0.7R	1.0534	1.0534
4.	Expanded Area Ratio	0.5529	0.5529
5.	Number of Blades	4	4
6.	Thickness at 0.7R	123 mm	5.86 mm

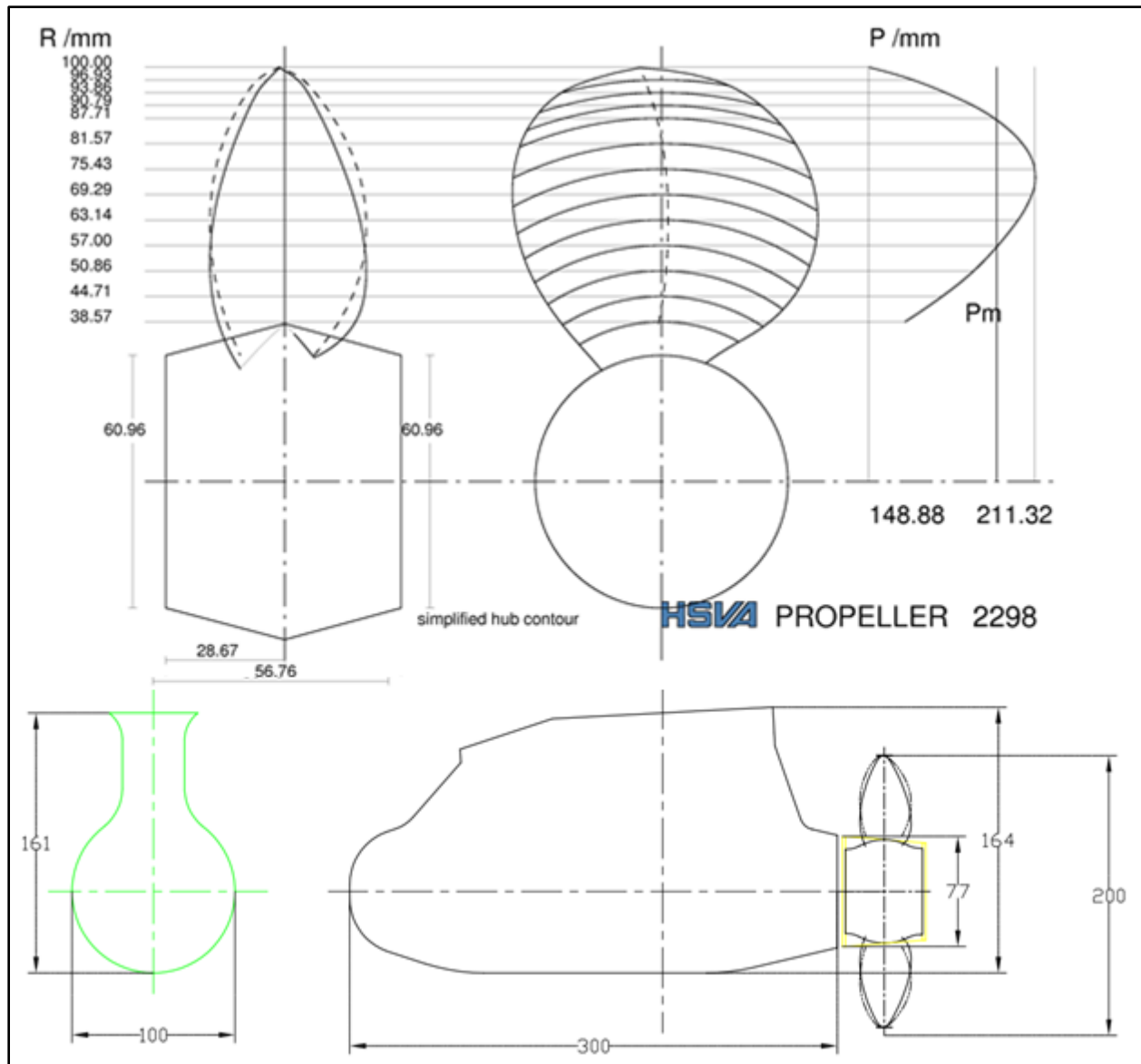


Figure 22: Schematic Representation of the Polarstern Propeller (Top) and Pod (Bottom) [32]

Moreover, an elliptical shaped hub cap (not shown in Figure 22) was placed on the upstream surface of the propeller hub to smoothen the flow as the hub of this propeller is considerably large as compared to its diameter.

4.2 The Open Water Test

The open water experiment for this propeller was carried out to obtain the K_T , K_Q and Efficiency (η) for a range of Advance Coefficients (J). The open water test was not carried out by the author but the results of the same were available in the HSVA Database [32].

The open water test was carried out from $J = 0.00$ to $J = 0.95$ in steps of 0.05. The test parameters are summarized in Table 4. The results obtained from the test are shown in Figure 23.

Table 4: Open Water Test Parameters [32]

S No.	Parameter	Value
1.	Test Number	6387.1
2.	Test Date	11.11.2015
3.	Water Density	998.71 kg/m ³
4.	Water Temperature	16.9 °C
5.	Propeller RPS	11.2 Hz
6.	Reynolds Number	403691
7.	Propeller Diameter	200 mm
8.	Advance Velocity Range	0 m/s to 2.13 m/s
9.	Advance Coefficient Range	0 to 0.95
10.	Pod Orientation	Pusher Mode

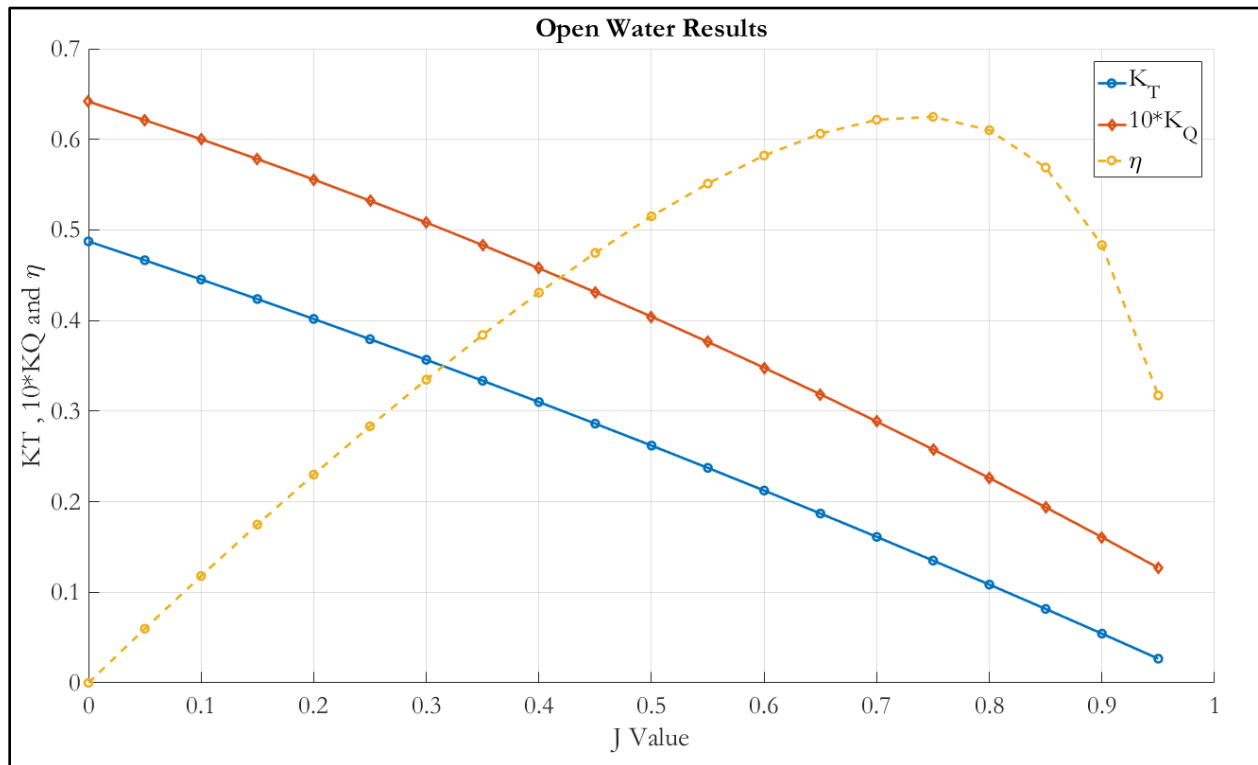


Figure 23: Results of the Open Water test for Polarstern Propeller with pod in pusher mode [32]

4.3 Air and Water Milling Experiments

The air milling and water milling experiments were carried out in the large ice tank of HSVA. The two experiments are similar in every sense except that the milling of the ice was done in air for the first case and was done under water for the second case.

In the coming pages, the ice tank, the ice making process, the ice feeding device and the results of the experiments along with the data processing techniques employed are explained in detail.

4.3.1 Large Ice Tank of HSVA

The large ice tank of HSVA is used to carry out the model test of ships and propellers in sea ice. A schematic representation of the tank is shown in Figure 24. The ice tank also has the capability to generate waves in the ice by the help of the wave maker located on the left side of the trim tank as shown in Figure 24. The main parameters of the tank are listed in Table 5.

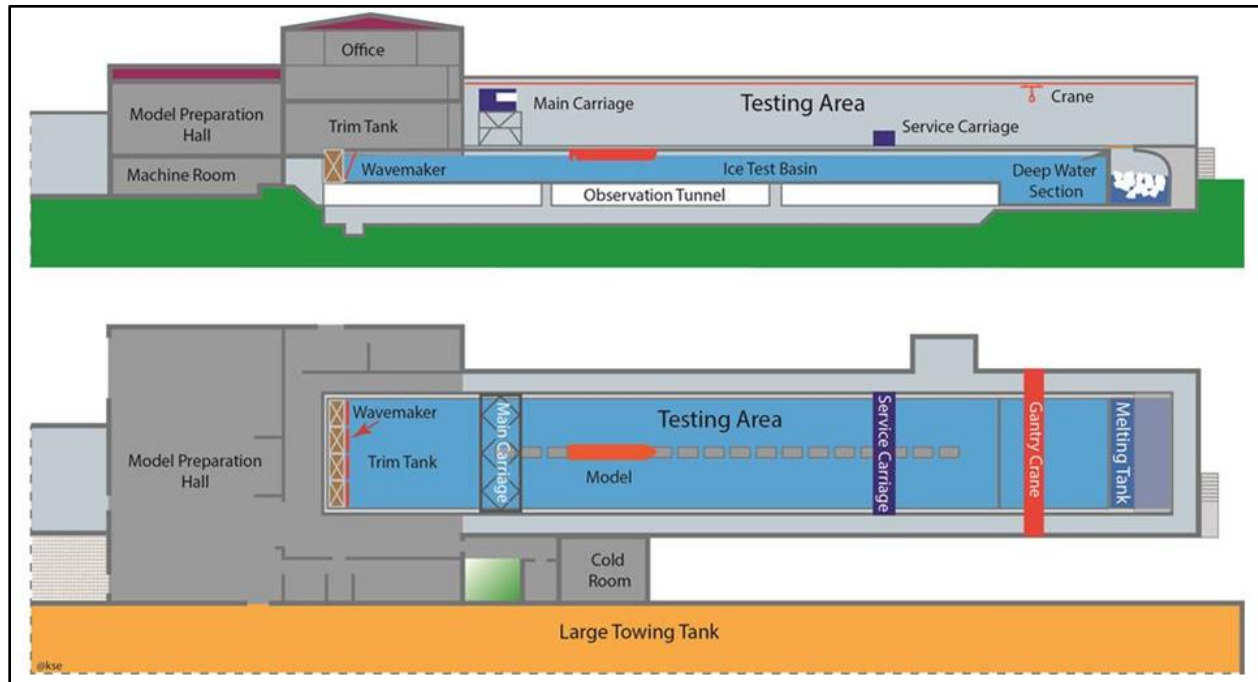


Figure 24: Schematic Representation of the Large Ice Tank at HSVA [32]

Table 5 : Main Parameters of the Large Ice Tank at HSVA [32]

S No	Parameter	Value
1.	Tank Length	78 m
2.	Tank Breadth	10 m
3.	Tank Depth	2.5 m
4.	Shallow Water Bottom	0.1 m to 2.0 m
5.	Ice Freezing Rate	about 2 mm/h
6.	Towing Carriage Speed	0.001 m/s to 3 m/s
7.	Towing Capacity	50 kN
8.	Transverse Carriage Speed	0.001 m/s to 0.5 m/s
9.	Transverse Capacity	5 kN
10.	Wave Type	Regular and Irregular
11.	Max. Wave Height	0.25 m
12.	Max. Deep Water Wave Period	1.8 s
13.	Max. Wave Period	3.0 s
14.	Frequency Range	0.5 to 5 Hz

The room that houses the large ice tank is cooled by the help of cold air blowing at -20°C through numerous air ducts located inside the room. The air is cooled by the R134a refrigerant which is compressed by 3 large compressors located in the machine room as shown in Figure 24. When the system is running at the optimal parameters, the ice freezing rate of 2 mm/hour is achieved.

4.3.2 The Ice Making Process

The model ice is produced according to the HSVA's standard procedure as given by Evers and Jochmann [15]. This ice making process has largely remained unchanged over the last two decades. The ice is made from salt water which is obtained by mixing 0.7% NaCl w/v with fresh water. The ice formation takes place in a sequence of steps as mentioned below:

- a) Firstly, the air temperature of the room is brought down to $\approx -20^{\circ}\text{C}$ by blowing in the cold air for around 8–10 hours.
- b) When the desired temperature of the room is achieved, hot water is sprayed from pressurized nozzles over the saline water of the ice tank.
- c) As soon as the hot water is sprayed into the cold air, the tiny droplets freeze instantly, forming minute ice crystals which then fall down on the surface of water leading to ice nucleation.
- d) The temperature of the room is maintained at $\approx -20^{\circ}\text{C}$ for next 8–10 hours or more, depending upon the thickness of ice desired. The crystals begin to develop and grow increasing the thickness of the ice layer.
- e) Moreover, there are small air vents on the bottom of the tank that supply air into the water of the ice tank. These tiny air bubbles of 200–500 μm in diameter rise up and get mixed with the ice, making it porous and thereby modelling it to the correct strength. The presence of these air bubbles also gives bright white appearance to the modelled ice.

After the ice is prepared it is sawed and suitable floe sizes are cut out for the use in the experiment. For the air milling experiment, the ice flow measured 700 mm by 180 mm having a thickness of ≈ 31 mm. For the water milling experiment, the ice flow measured 425 mm by 175 mm having a thickness of ≈ 41 mm. The two ice floes are shown in Figure 25.

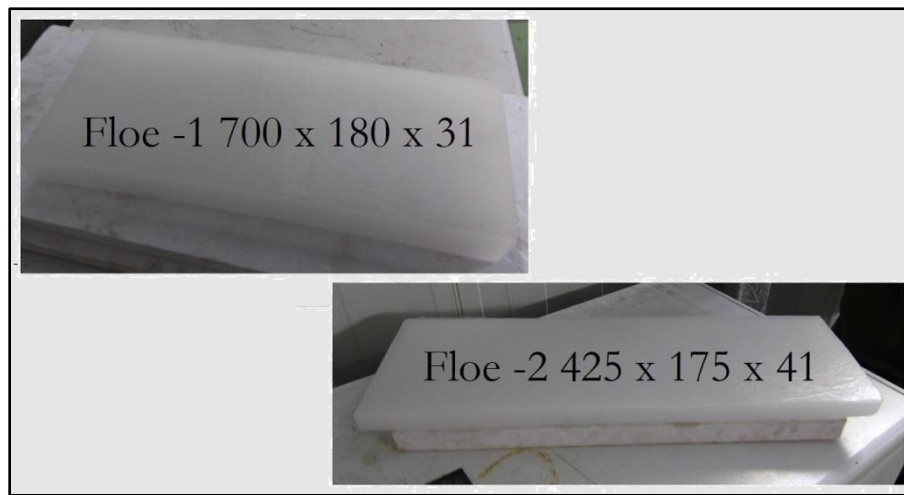


Figure 25 : Ice floes used in the Experiments

4.3.3 The Ice Feeding Device

The ice feeding device is a structure that on one end has a mechanism to deliver an ice floe towards the propeller at a controlled speed and has the podded propeller mounted on other end. It also has an ice guiding mechanism to guide the ice floe towards the propeller without any unwanted lateral motions.

The side view, top view and front view of the ice feeding device is shown in Figure 26, Figure 27 and Figure 28 respectively.

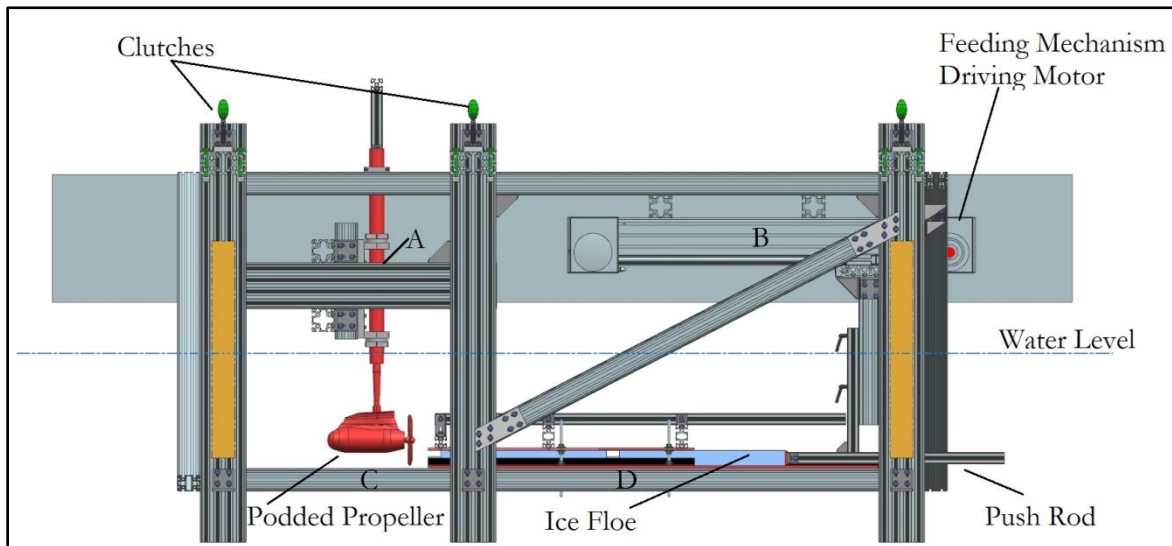


Figure 26 : Side View of the Ice Feeding Device [32]

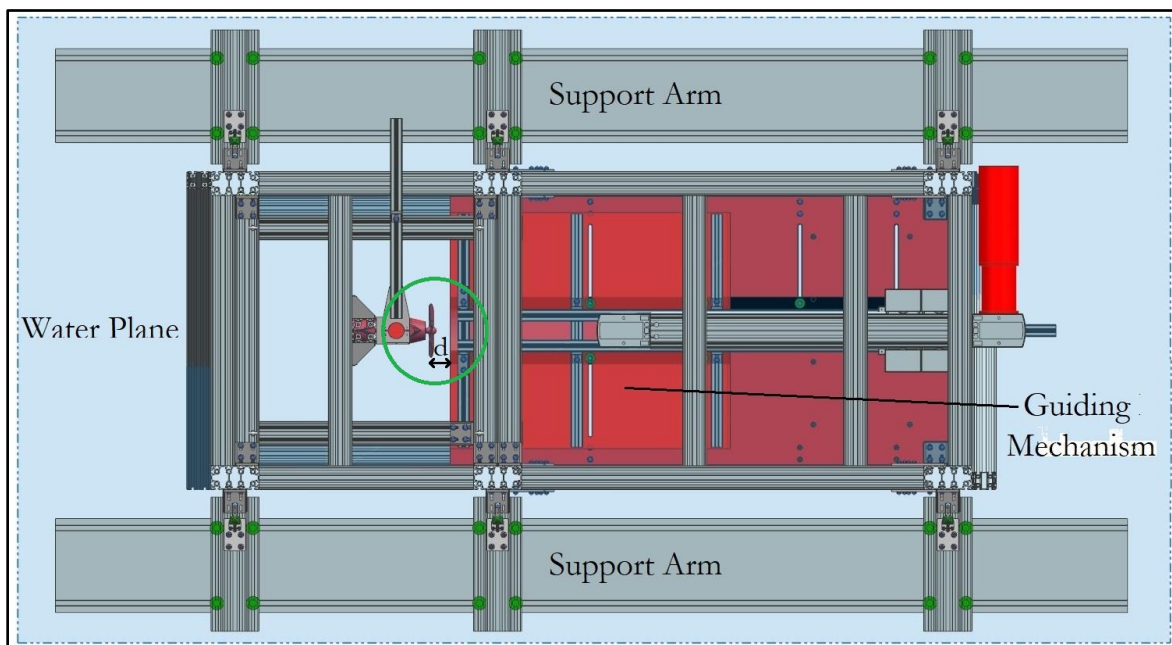


Figure 27: Top View of the Ice Feeding Device [32]

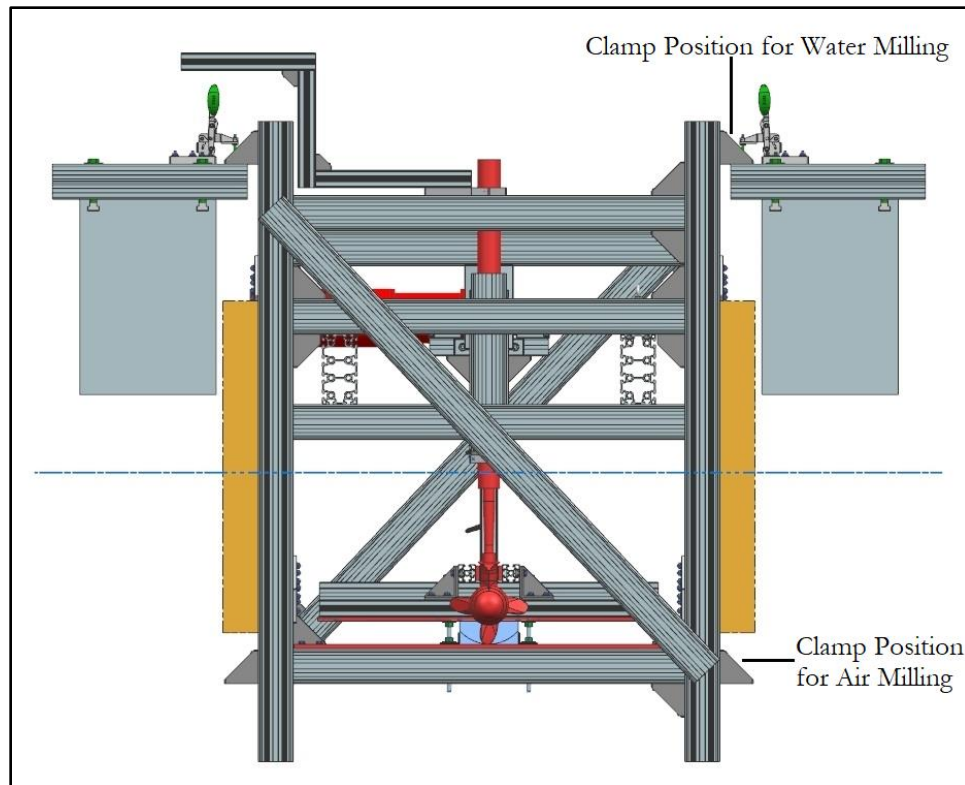


Figure 28: Front View of the Ice Feeding Device [32]

The various components of the ice feeding device are as follows:

a) **Driving Motor and Push Rod Assembly:** The driving motor of the feeding mechanism shown in Figure 26 drives the push rod back and forth. The push rod pushes the ice floe towards the propeller at a controlled speed.

The push rod is attached to a belt that is tightly wrapped around two rollers. The driving motor is connected to one of the rollers and as the motor rotates, the rollers also rotate and the belt moves in a linear fashion along with the push rod.

b) **Guiding Mechanism:** The guiding mechanism shown in Figure 29 ensures that the ice floe moves in a straight position towards the propeller. This guiding mechanism is essentially a slot having the same width and thickness as the ice floe used in the experiment. This slot is made from PVC plates that are adjustable to accommodate the ice floes of varied dimensions.

c) **Clutches and Support Arms:** The support arms shown in Figure 27 are used to attach the ice feeding device to the main carriage of the ice tank. The clutches are used to fasten the ice feeding device to the support arms that are attached to the carriage body. The clutches fasten the ice feeding device at two different positions for water milling and air milling as shown in Figure 28.

Furthermore, the water-line showed in Figure 26 is only applicable in case of the water milling of ice. The ice feeding device is put in water and the water line indicates the portion of the device under water.

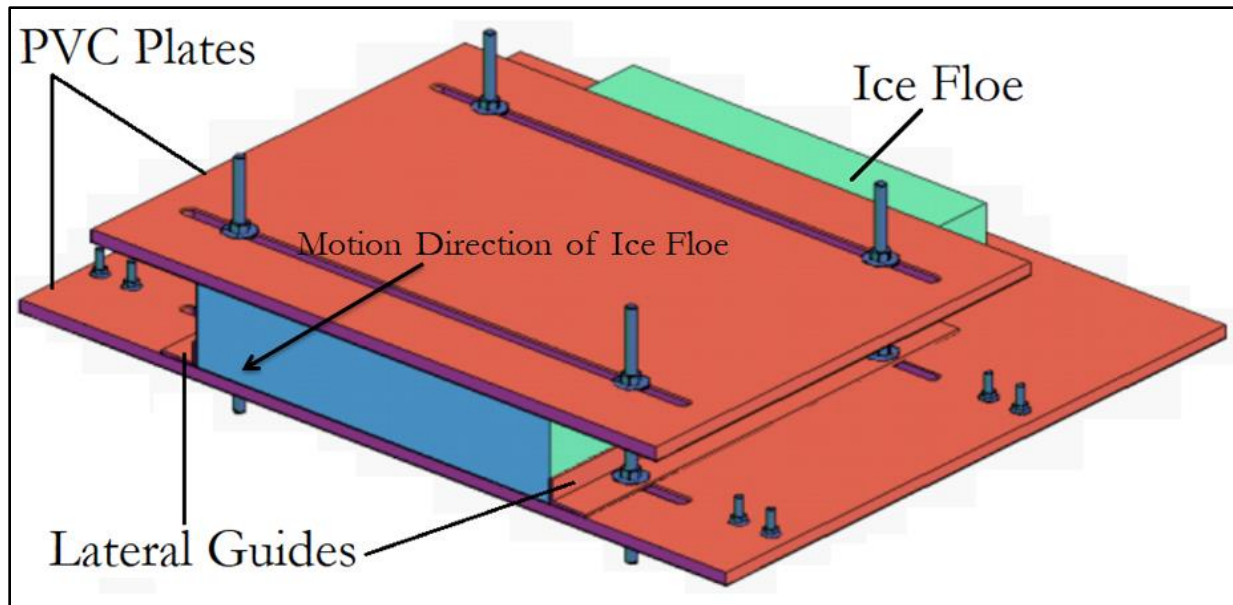


Figure 29: The Guiding Mechanism [32]

4.3.4 The Test Set-up

The propeller was tested in the puller configuration unlike the open water test, which was carried out in the pusher configuration (Table 4). In the puller configuration, the blades face towards the hull or in this case the ice feeding device. The propeller blades were put close to the guiding mechanism as shown in Figure 27 ($d \approx 50$ mm). This was done to avoid vibrations owing to the formation of a long cantilever once the ice floe was out of the PVC plates.

The pod housed the load cells to measure the torque and thrust acting on the propeller. It also contained a tachometer to measure the RPM of the propeller. Three additional load cells were present on the vertical shaft supporting the pod (point A in Figure 26) to measure the forces and moments acting on the pod along x, y and z axis.

Moreover, sensors were located on the push rod of the ice feeding device (point B in Figure 26) to measure the position and speed of the push rod and in turn the ice floe. In addition to that, two accelerometers were also present, one on the guide rails (point D in Figure 26) and other near the pod (point C in Figure 26) to measure the vibrations in the ice floe and the propeller respectively.

A list of the data channels used in the experiment is given in Table 6. The channels recorded the data at a high frequency of 2.4 kHz in order to capture the effect of individual blade–ice impacts at high rotational speeds.

To record the experiment, two GoPro Hero® cameras having a frame rate of 120 fps were used to film the experiment from two different angles. In addition to them, a high speed camera having a frame rate of 5000 fps was also used. However, the high speed camera was only used for the milling of ice under water and not for the air milling, as the high speed footage of air milling was already available from the experiments conducted by Bach [14].

Table 6: The Data Channels Recorded During the Experiment

Channel Number	Channel Data
1.	Time (t)
2.	Force in x direction on the pod, (F_x)
3.	Force in y direction on the pod, (F_y)
4.	Force on the push rod in the direction of motion, (F_p)
5.	Position of the push rod in the direction of motion, (S)
6.	RPS of the propeller, (n)
7.	Azimuth angle of the pod, (θ)
8.	Torque on the propeller shaft, (Q)
9.	Thrust on the propeller shaft, (T)
10.	Acceleration in x direction at the guide rail, (a_{x-ice})
11.	Acceleration in y direction at the guide rail, (a_{y-ice})
12.	Acceleration in z direction at the guide rail, (a_{z-ice})
13.	Acceleration in x direction near the pod, (a_{x-pod})
14.	Acceleration in y direction near the pod, (a_{y-pod})
15.	Acceleration in z direction near the pod, (a_{z-pod})
16.	Synchronization Signal

The synchronization signal mentioned in Table 6 is simply a trigger signal that when activated signifies the start of the experiment and synchronizes all the data recording equipment and the high speed camera.

4.3.5 The Air Milling Experiment

The Floe 1 was used for the air milling and the ice feeding device was placed outside the water as shown in Figure 30. Two runs were performed at two different feeding speeds of the ice floe. The test parameters are listed in Table 7.

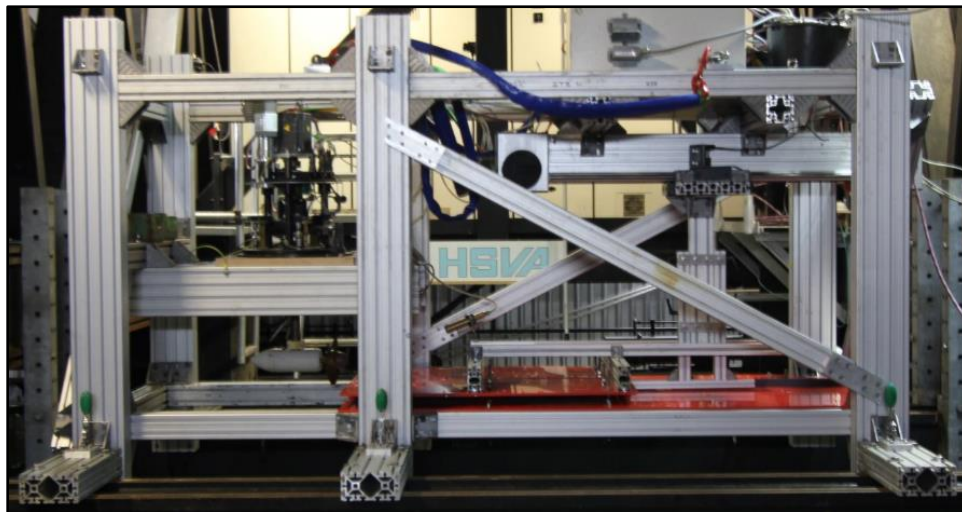


Figure 30: Ice Feeding Device in Air Milling Experiment

Table 7 : Test Parameters of Air Milling Experiment

S No	Parameter	Value
1.	Propeller RPS	9 Hz
2.	Feeding Speed	27 mm/s and 81 mm/s
3.	Propeller Diameter	200 mm
4.	Advance Values	0.015 and 0.045
5.	Depth of Cut	17 mm
6.	Ice Floe Dimensions	700 mm (L) x 180 mm (W) x 31 mm (T)

The data was recorded and processed to obtain the values of the propeller thrust and torque. The data from channels 1, 6, 8 and 9 was used to obtain time, propeller RPS, propeller torque and thrust respectively. The raw data from the two runs of the experiment is shown in Figure 31.

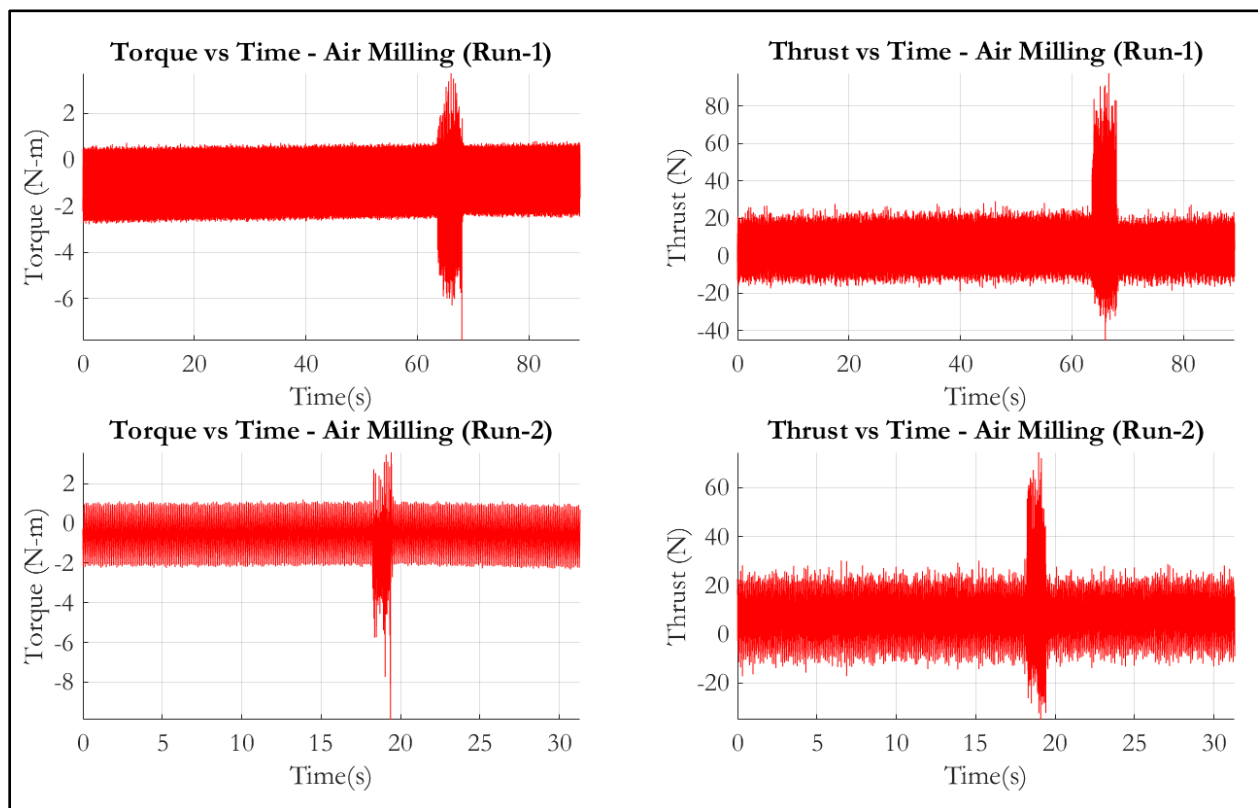


Figure 31: Raw Data from the Air Milling Experiment

4.3.6 The Water Milling Experiment

The Floe 2 was used for the water milling and the ice feeding device was placed inside the water and submerged up-to the water level shown in Figure 26. Two runs were performed using Floe 2 at two different feeding speeds of the ice floe. The depth of cut was different from the air milling. The test parameters are listed in Table 8.

Table 8 : Test Parameters of Water Milling Experiment

S No	Parameter	Value
1.	Propeller RPS	9 Hz
2.	Axial speed of Ice Floe	27 mm/s and 81 mm/s
3.	Propeller Diameter	200 mm
4.	Advance Values	0.015 and 0.045
5.	Depth of Cut	27 mm
6.	Ice Floe Dimensions	425 mm (L) x 175 mm (W) x 41 mm (T)

The data recording and processing was similar to the air milling experiment. The raw data from the experiment is shown in Figure 32. However, unlike the air milling, the data from the two runs of the water milling experiment was recorded in the same file.

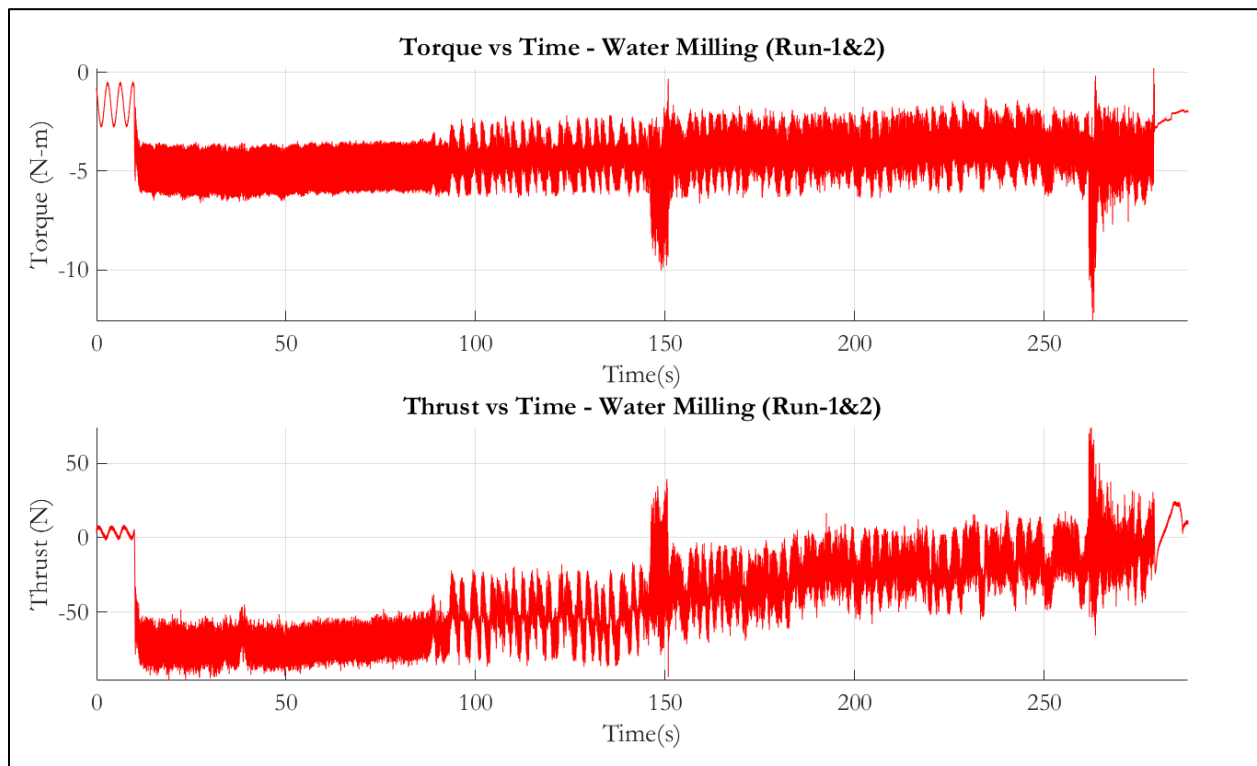


Figure 32: Raw Data from the Water Milling Experiment

4.3.7 The Ice Compression Test

The compression test was performed on samples collected from the two ice floes used in the experiment. The compression test was done on a hydraulic compression machine as shown in Figure 33. The machine used in the experiment is equipped with a load cell and a potentiometer to measure the compressive force and the change in the length of the ice respectively.

The compression test was carried out in the cold room of HSVA. Four samples of Floe 1 and two samples of Floe 2 were tested and data was recorded. The test parameters and the results of the compression tests are listed in Table 9.

The average compression strength of Floe 1 was 1.41 MPa and for Floe 2 it was 1.03 MPa. This compression strength data was also used to estimate the empirical factors used for calculation of the ice loads as mentioned in section 3.6 and 5.2.

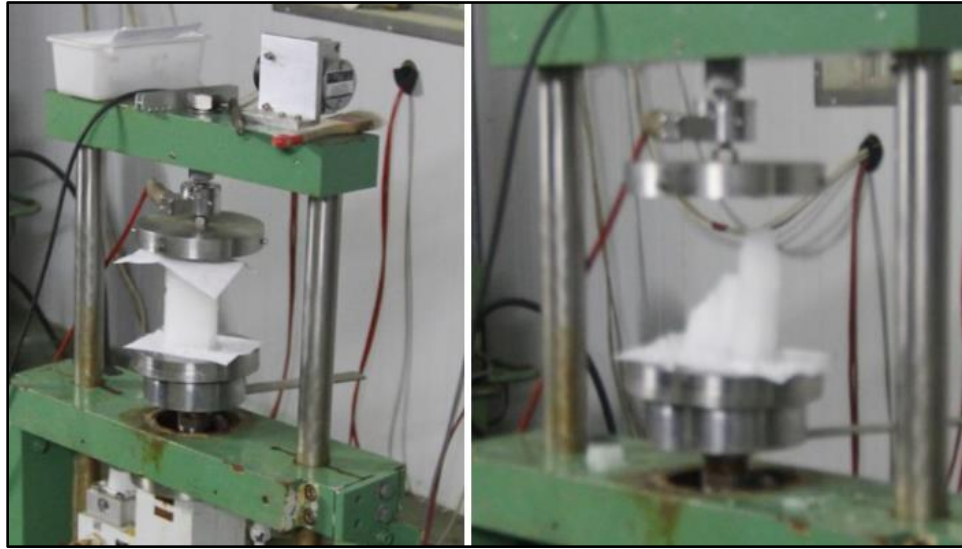


Figure 33: Compression Test of Ice: Start (Left), End (Right)

Table 9: Compression Test of Ice: Parameters and Results

Sample	Compression Force (kN)	Cross Section Dimension (mm x mm)	Compressive Strength (MPa)
Floe1/01	4.04	60 x 30	2.24
Floe1/02	1.87	60 x 31	1.00
Floe1/03	2.10	60 x 30	1.16
Floe1/04	2.34	60 x 32	1.22
Average			1.41
Floe2/01	2.24	70 x 41.0	0.78
Floe2/02	3.72	70 x 41.5	1.28
Average			1.03

4.3.8 Data Processing and Results

The raw data shown in Figure 31 and Figure 32 was processed using a variety of data processing techniques. These data processing techniques depend upon a number of factors like the noise in the signal, accuracy of the results desired, method of data acquisition, sampling frequency, etc. The data processing software used for this experiment was the Signal Processing Toolbox of MATLAB. The various steps involved in the data processing are explained below.

a) **Offset Correction:** From Figure 31 we can see that in both test runs of air milling, the propeller is running idle for some time before the milling commences, which is marked by the sudden peak in the torque and thrust values. Since the propeller is running in idle condition in air, there should be no loads acting on it. However, if we look at Figure 31, we can see that both the thrust and torque data have a non-zero average value during this time period. This can be due many reasons, like offset in the sensor, or an unbalanced force in the system due to vibrations, wobble in the axis of propeller, etc. As a result this offset has to be removed first before proceeding for further signal processing. This process is known as the offset correction.

The offset value is calculated as the difference between the average of the data before milling and zero value. This offset value is then added to the whole signal. An example of the difference due to the offset correction can be seen in Figure 34 below.

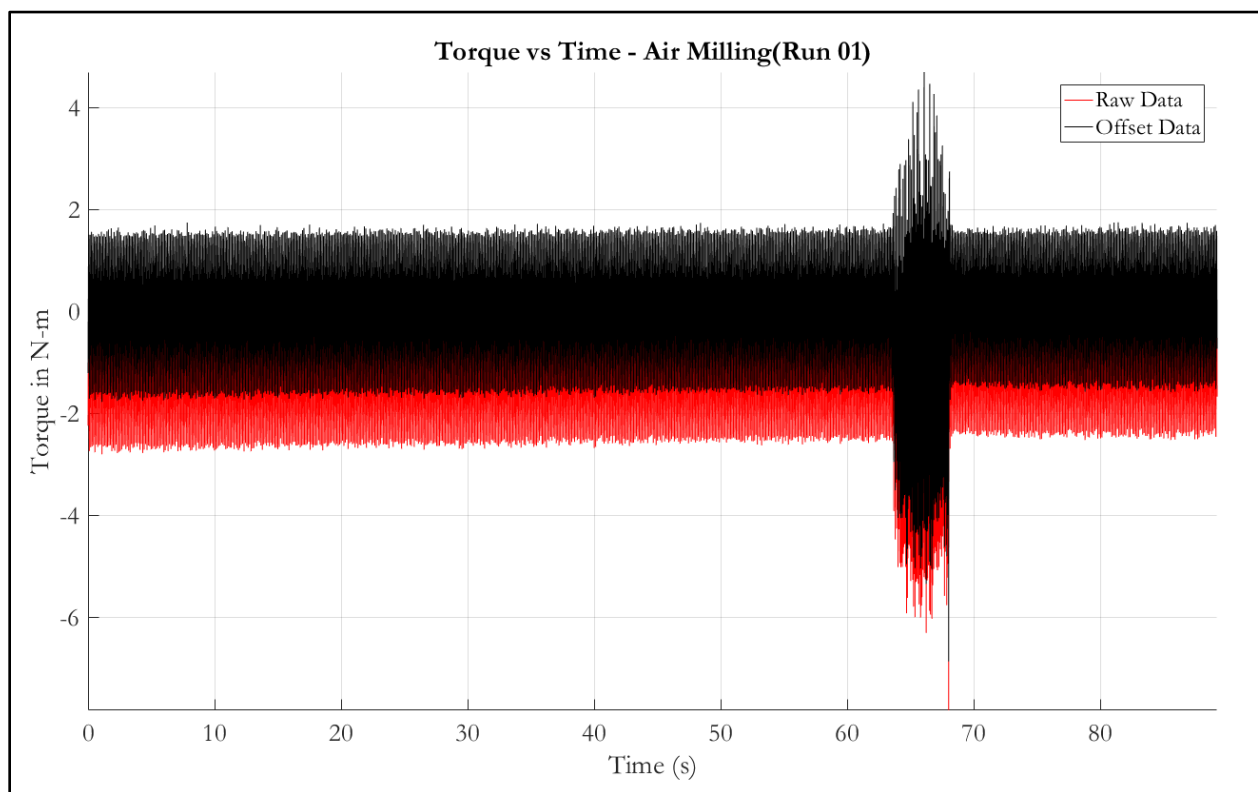


Figure 34: Raw Data and Offset Data

In case of the water milling, the propeller is also running idle for some time before the milling commences as seen in Figure 32. However, as the propeller is running in water, the hydrodynamic loads are constantly acting on it. These loads also have to be evaluated and thus the method of offset correction cannot be same as that of the air milling.

Since, no change was done in the setup of the experiment between air milling and water milling, the offset of air milling was applied to the water milling for a given feeding speed, i.e. the offset of run 1 of air milling was applied to run 1 of water milling and the offset of run 2 of air milling was applied

to run 2 of water milling. This ensured that the undesirable causes/effects that produced an offset in the air milling were also eliminated from the results of the water milling.

b) Signal Truncation: Since, the data recorded during the milling of ice is of interest and the propeller idle data is not required, the signal was truncated such that only the ice milling data was retained. This signal truncation also reduced the amount of data to be handled for further processing.

c) Frequency Filter: The data recorded in the milling experiment had a lot of noise due to many factors like vibrations, wobbling of the propeller axis, unbalanced propeller blades, etc. The best way to filter out this noise was to use a frequency filter so that the data at a particular frequency and its harmonics was retained, and the remaining data was eliminated as noise.

In the present experiment, the propeller was rotating at a frequency of 9 Hz and therefore, a significant amount of the relevant data was recorded in the raw signal at this frequency. However, the propeller had 4 blades, so the frequency of the impacts was 36 Hz. In order to extract this data, another frequency filter was required to be added at 36 Hz. Moreover, some data was also present in the higher harmonics of the propeller rotation frequency and was also to be extracted.

To get a clear picture of the frequency spectrum, the Fourier Transform of the raw signals was performed as shown in Figure 35 and Figure 36. From these figures it was clear that the maximum data was present in the propeller rotation frequency and its higher harmonics. The peaks were observable up-to the 25th Harmonic (225 Hz) of the propeller rotation frequency of 9 Hz.

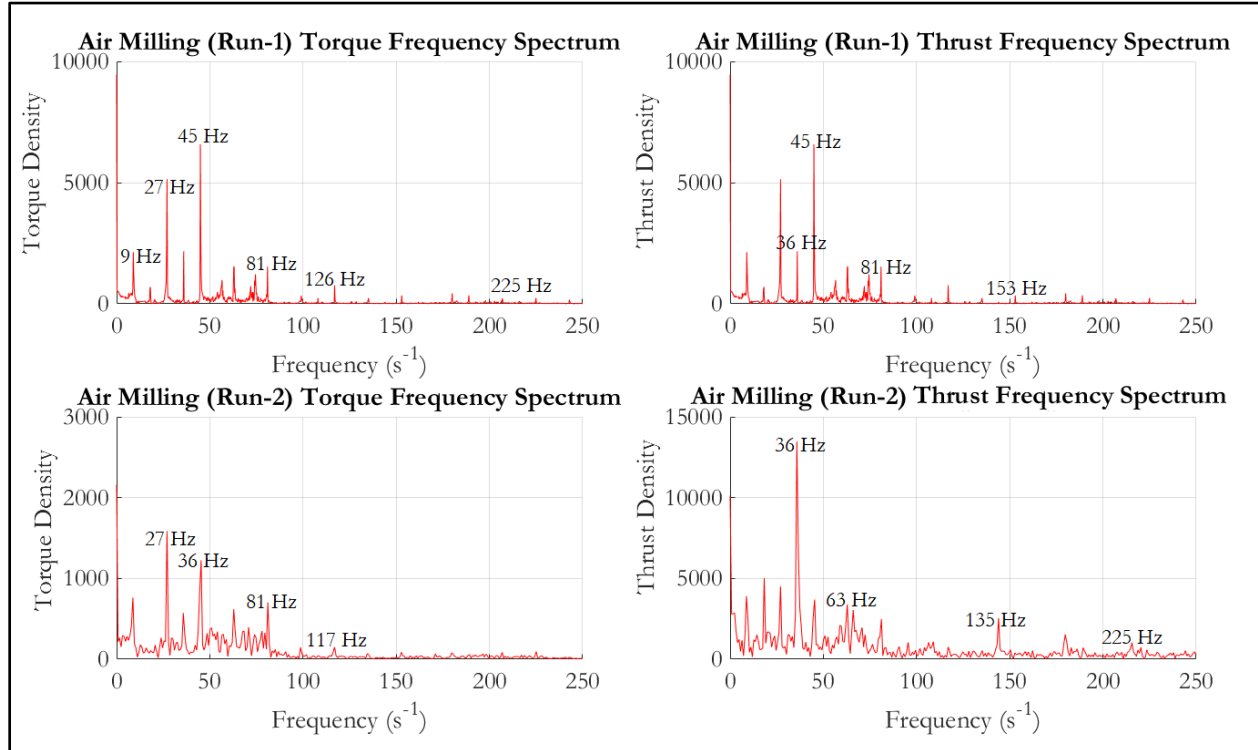


Figure 35: Frequency Spectrum of Raw Signals from Air Milling

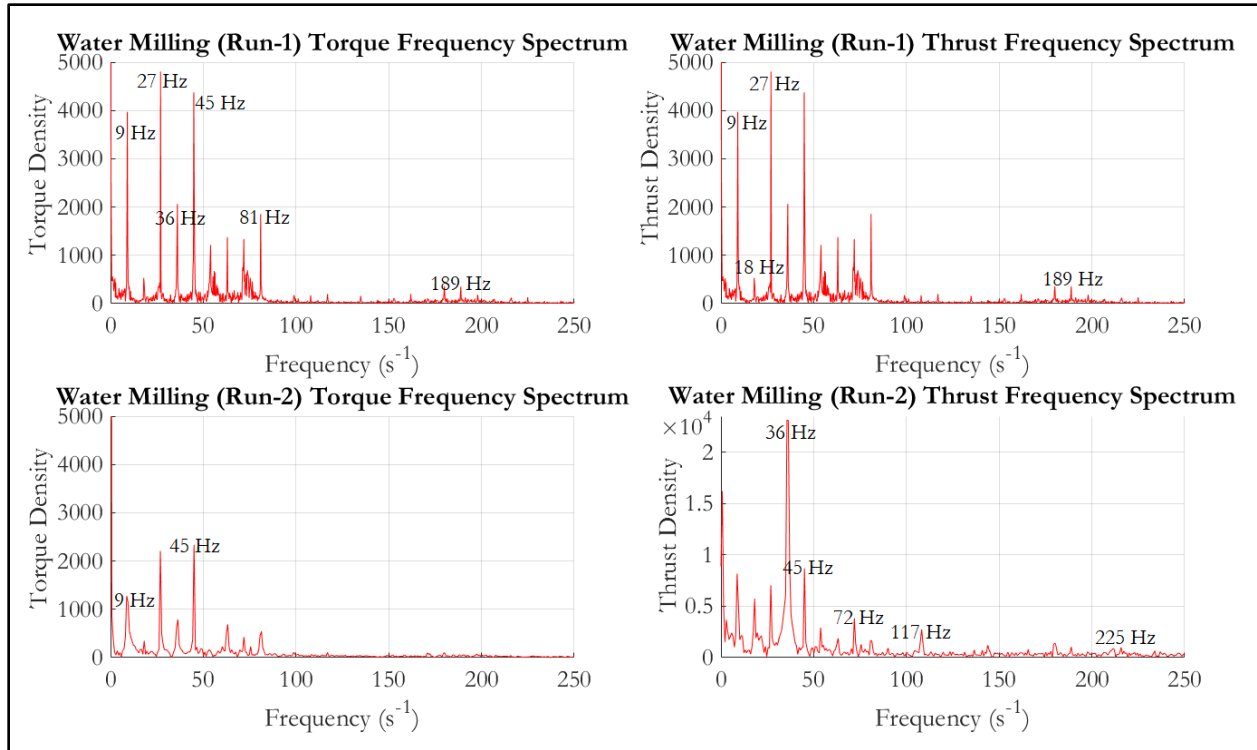


Figure 36: Frequency Spectrum of Raw Signals from Water Milling

Thus, a frequency filter was designed that filtered out the data at the frequency of 9 Hz and its first 25 harmonics. The design parameters of the filter used are shown in Table 10 below.

Table 10: Design Parameters of the Frequency Filter

S No.	Parameter	Value
1.	Impulse Response	Infinite
2.	Design Algorithm	Chebyshev Filter, Type II
3.	Filter Technique	Band-stop
4.	Filter Order	20
5.	Primary Frequency	9 Hz
6.	Number of Harmonics	25
7.	Stop band Frequencies	$f-0.25$ to $f+0.25$, $f \in [9, \dots, 225]$
8.	Stop band attenuation	60 dB

The design parameters used in the Table 10 above were selected by studying the raw signal carefully, the details of which have been omitted to keep the report short. After processing the data, the thrust and torque values were obtained. The KT & KQ values were obtained using the formulae mentioned in section 3.5.1.

The results obtained from the experiments are summarized in Table 11 below.

Table 11 : Results from the Milling Experiment

Experiment	J value	KT Value	10*KQ Value
Air Milling Run 1	0.015	-0.1326	0.7027
Air Milling Run 2	0.045	-0.2651	1.0560
Water Milling Run 1	0.015	0.3126	1.7239
Water Milling Run 2	0.045	0.2010	2.3870

Based on the results obtained from the open water test and the milling experiments, the code was calibrated individually for the separable hydrodynamic loads, inseparable hydrodynamic loads and the ice loads. The process of the calibration is explained in the chapter 5 below.

Chapter 5

CODE CALIBRATION & RESULTS

The primary objective of this chapter is to calibrate the numerical code Ice-PPB based on the experimental results obtained from the open water and ice milling tests. After the code is calibrated, the numerical code is used to generate the results and study the influence of various parameters on the propeller loads. The calibration of the code is done separately for the separable hydrodynamic, inseparable hydrodynamic and ice loads as explained below.

5.1 Calibration of the Separable Hydrodynamic Loads

In order to calibrate the separable hydrodynamic loads, the open water loads were calculated from $J = 0.00$ to $J = 0.95$ as these are the same J values that were used in the open water experiment mentioned in section 4.2. The loads were calculated as per the calculations mentioned in section 3.5. However, before the code was run and the results were obtained, a convergence study was to be performed on 3 input parameters as mentioned in section 3.3.1.

5.1.1 Convergence of the Input Parameters

The convergence study of an input parameter is carried out by varying the value of the parameter while keeping all the other input parameters constant. The convergence study was done using the Polarstern propeller with following input data.

Table 12 : Input Data for Convergence Study

S No	Parameter	Value
1.	Advance Coefficient	0.4
2.	Full scale diameter of the propeller	4200 mm
3.	Full scale diameter of the hub	1617 mm
4.	Full Scale Propeller RPM	117.84
5.	Propeller Blade Number	4
6.	Scaling Factor	21
7.	Expanded Area Ratio	0.5529
8.	Pitch to Diameter Ratio (P/D) at 0.7 R	1.0534
9.	Thickness at 0.7 R in Full Scale	123 mm
10.	Number of Harmonics	[1,...,6]
11.	Number of turn steps	[5,...,18]
12.	Number of turns in the propeller race	[1,...,6]

The K_T and K_Q values were calculated using the input data from Table 12. For a given parameter on which convergence study was to be performed, the relative errors in K_T and K_Q for successive input values were calculated. The results of the convergence study are shown in Figure 37 below. From Figure 37 it can be seen that in order to have errors less than 0.05%, the value selected for Number of Harmonics is 2, and to have errors less than 0.5% the value selected for the Number of Turns in the Propeller Race is 3 and for the Number of Turn Steps is 11.

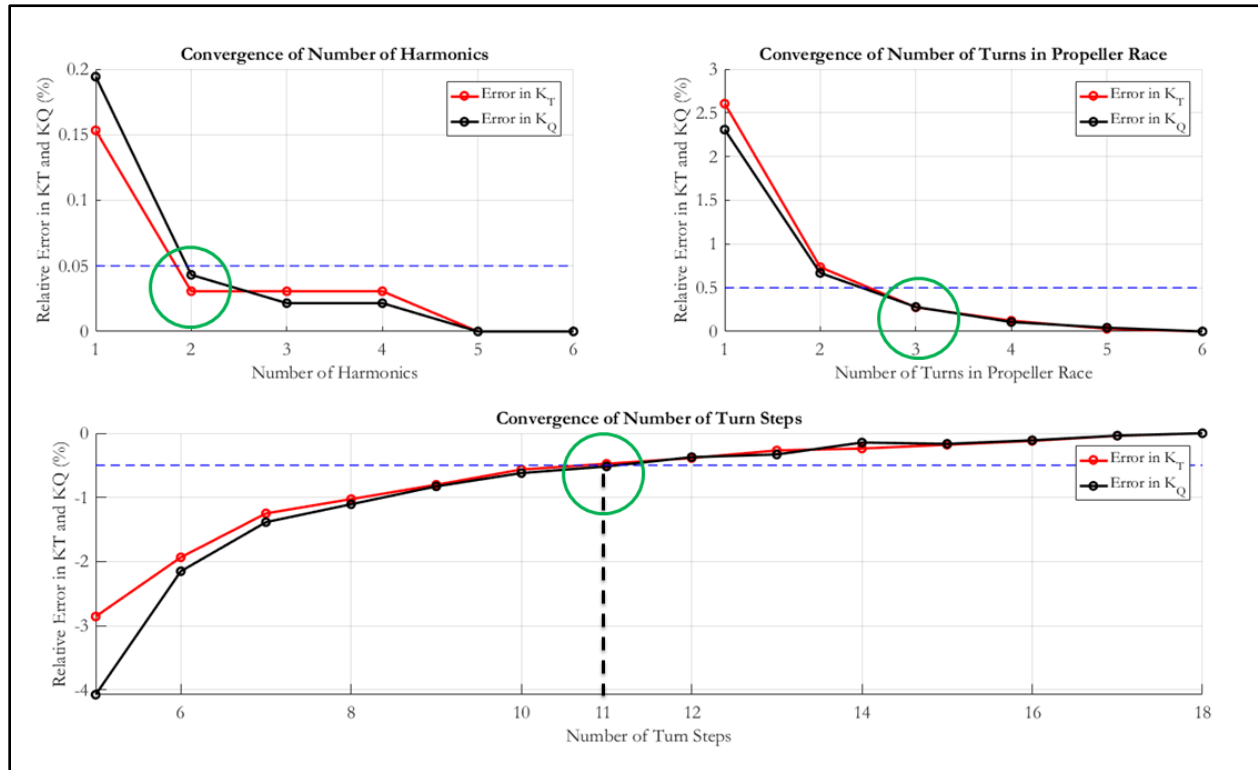


Figure 37: Convergence of the Input Parameters for Hydrodynamic Loads

Using the converged values, the open water loads were calculated and compared with the experimental values as explained in the next section.

5.1.2 Comparison of the Open Water Results

A comparison of the open water results calculated by the code and the open water experimental results (Figure 23) is shown in Figure 38 below.

In Figure 38, the solid lines indicate the values from the numerical code and the dashed lines indicate the values from the open water experiment. A large variation is observed between the experimental and numerical values especially at the small J values. The reasons behind such a large difference are explained below.

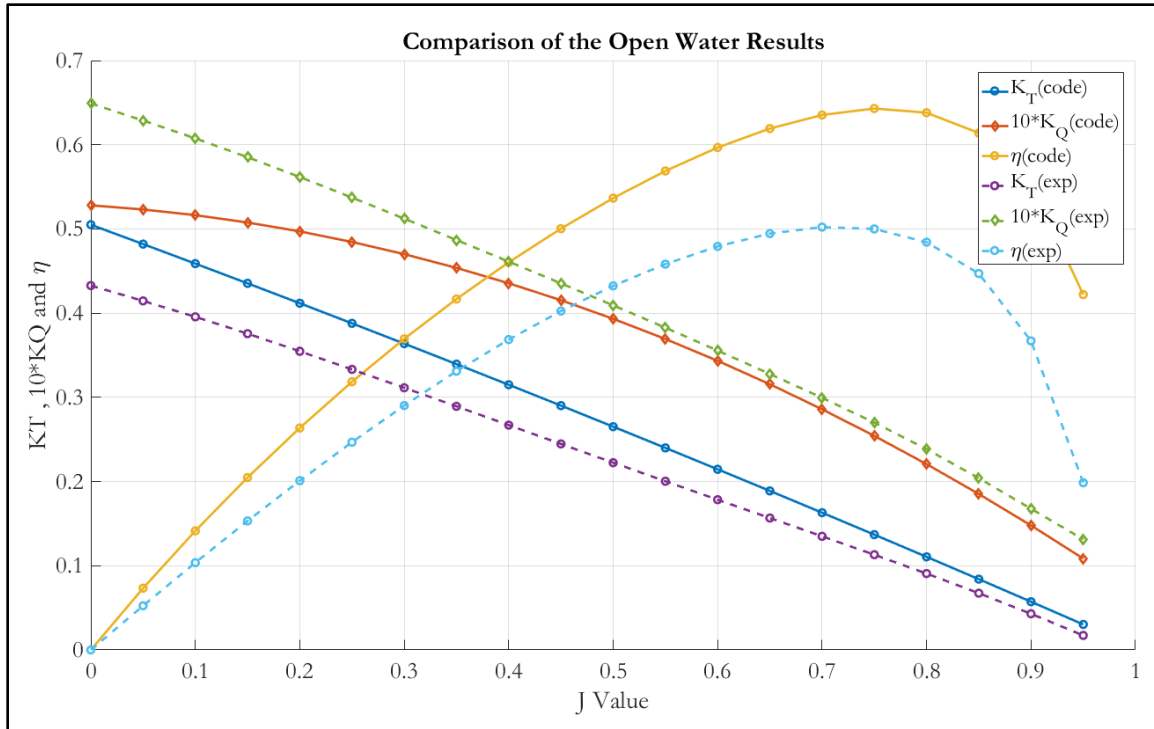


Figure 38: Comparison of the Open Water Results

a) **Difference in the KT Values:** The significant difference between the KT values of the code and the experiment has nothing to do with the calibration of the code as the difference arises due to the different positions of the pod.

The code Ice-PPB calculates the loads on the propeller in the puller mode, i.e. the blades face the hull and pod is present in the downstream of the propeller race. In this arrangement, the ice loads are more severe as the big chunks of ice coming from the hull directly hit the propeller blades and increase the loads significantly. On the other hand, in the pusher configuration, the pod body faces the hull and is located at the upstream of the propeller race. In this configuration, the big chunks of ice coming from the hull hit the pod and either get broken into smaller pieces or get diverted away from the propeller blades, thereby considerably reducing the impact loads on the blades. Thus, in order to model the severe case of impact loading during the ice interaction, the code calculates all the loads only in the puller configuration.

The open water test was carried out in the pusher configuration as mentioned in Table 4 and no experimental data was present in the HSVA archive in the puller mode for the Polarstern propeller mounted on the selected pod body and hence the pusher configuration data was used.

Due to the change in the orientation of the pod, the system thrust (thrust on blades + thrust on the pod body) changes but the blade thrust and torque is not affected much. However, both the code and the experiment calculate the system thrust values, so a correction is required in order to match the thrust results. According to a study carried out by H J Heinke at SVA Potsdam [35], for the pod

body and propeller diameter used in the experiment, the system thrust is around $\sim 10\%$ higher in puller mode than in pusher mode.

Thus, the K_T values calculated by Ice-PPB code were reduced by a factor of 10%, and the comparison is shown in Figure 39. From Figure 39, we can see that the difference between the numerical code results and experimental results has reduced significantly for all the J values. Thus, the surface panel method estimates the thrust of the propeller with very high accuracy even though it is based on potential theory. This is because the thrust is least affected by the viscosity of the fluid.

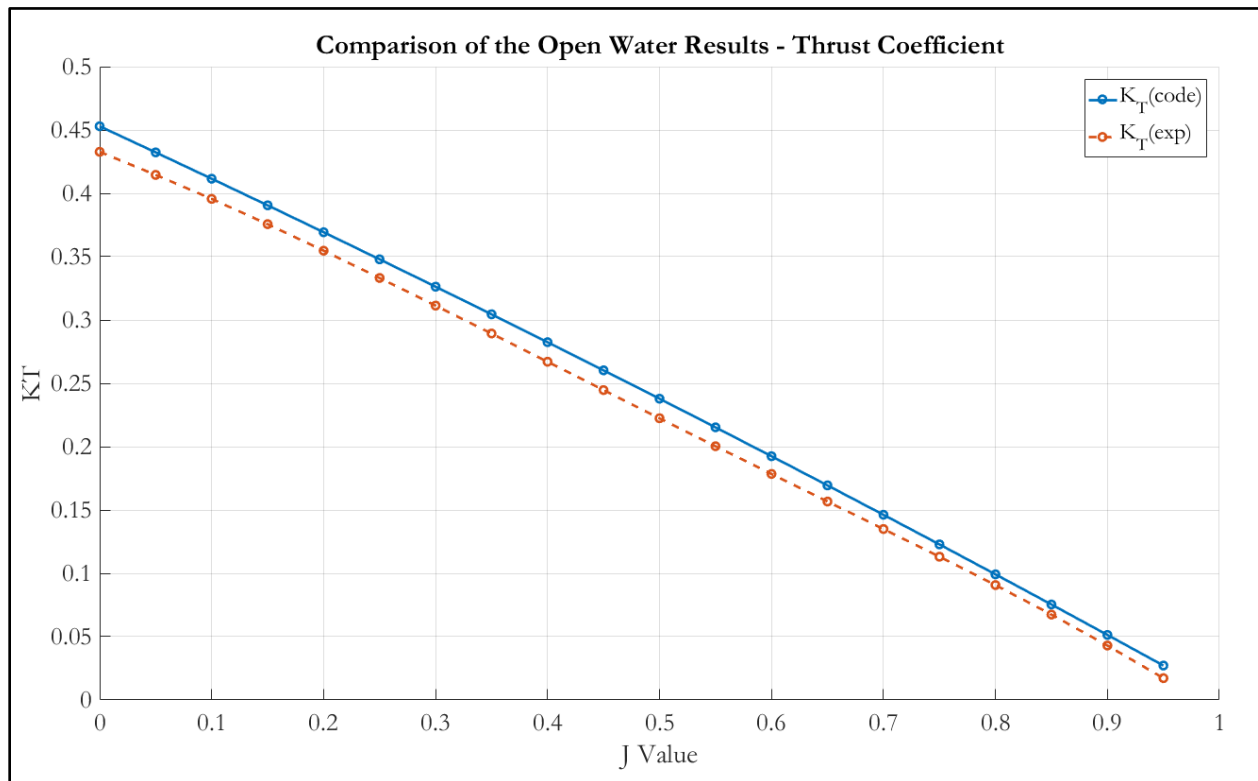


Figure 39 : Comparison of Open Water Thrust Coefficient

b) Difference in the KQ Values: The difference between the KQ values is small at high J values and very large at low J values. As discussed earlier, the change in the pod configuration does not affect the KQ values and this difference arises due to the effect of viscosity. In the original code PPB, a simple flat plate friction correction for viscosity is present, but this correction is not enough to take into consideration the viscous effects introduced at low J values.

At small J values, the angle of attack on the propeller blade sections is large and results in the flow separation near the leading edge. As a result, the viscous forces become highly complex and comparable to the inertial forces, and thus produce a large variation between the numerical and experimental results. However, at high values of J (typically $J \geq 0.4$); the angle of attack is small and no flow separation takes place and thus the viscous effects become less dominant and can be modelled by a simple flat plate friction correction with sufficient accuracy. This is evident from the small difference in the KQ values for high J values.

These complex viscous forces at low J values significantly increase the propeller torque as seen from Figure 38. Since the code Ice-PPB is based on potential flow theory, we therefore cannot directly take into account these complex viscous effects by modelling flow separation. Thus, in order to account for the increase in the torque at low J values, we use mathematical techniques that mimic this effect of viscosity. This mathematical technique called viscous correction is explained in the next section.

c) **Difference in the Efficiency Values:** The efficiency of a propeller at a given value of J is directly proportional to the ratio of KT and KQ . Since, we have a difference in the KT and KQ values; this difference is also reflected in the efficiency values. As we calibrate the code and minimize the difference between KT and KQ values of the code and the experiment, the efficiency values will automatically be taken care of.

5.1.3 Viscous Correction

The viscous correction is a mathematical modification done in the numerical code in order to take into account the effect of the viscosity at low J values. The viscous correction described here is different from the flat plate correction already present in PPB and addresses the strong change in pressure forces originating due to the flow separation. This modification ensures higher values of torque at low J values in order to minimize the difference between the numerical and experimental results.

Consider a cross section of a propeller blade at an arbitrary radius (r) as shown below in Figure 40. There are two sets of panels present; one set present on the pressure side called the pressure panels and the other set present on the suction side called the suction panels. Furthermore, each panel has a surface normal vector associated with it (green colored arrows in Figure 40) and its direction depends on the coordinates of the 4 points that constitute the panel.

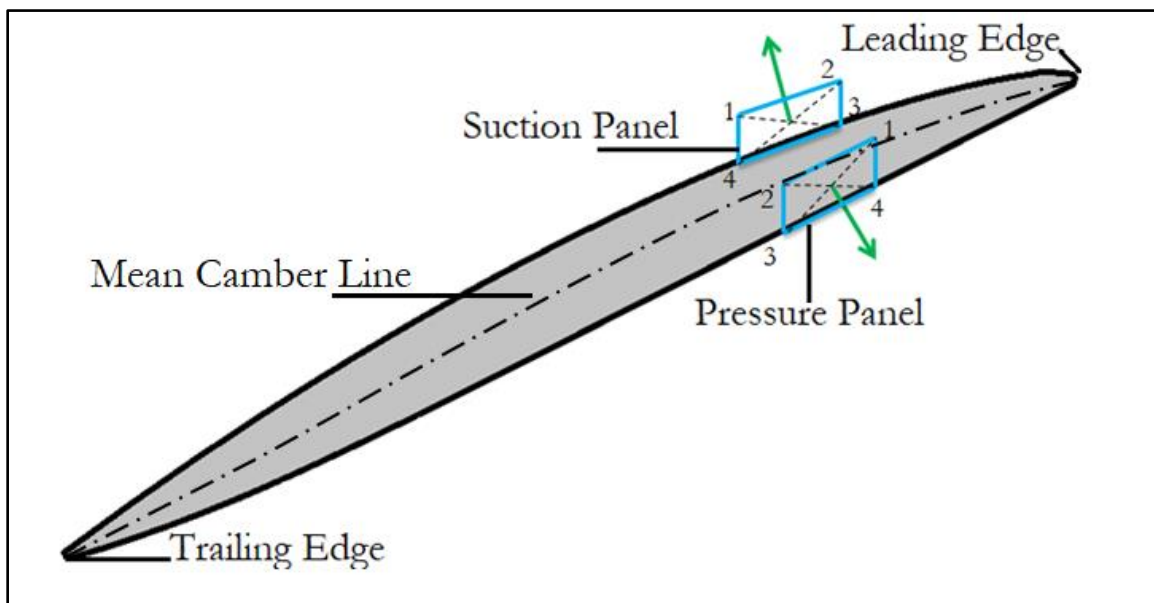


Figure 40: Pressure & Suction Panels and Surface Normal Vectors

The direction of the surface normal vector of the panels is not perpendicular to the mean camber line, and this holds true for most of the panels located on the pressure and suction surfaces at a given radius (r). This lack of perpendicularity is because of the varying curvature of the pressure and suction surface. Furthermore, the C_p values acting on the pressure panels are higher than the suction panels, and thus there is net force acting from the pressure side towards the suction side. A part of this net force is perpendicular to the mean camber line and the amount of this net force that is perpendicular to the mean camber line depends on the angle between the surface normal vector of the panels and the mean camber line. If the surface normal vector of all the panels is perpendicular to the mean camber line, then the entire net force is perpendicular to the mean camber line, otherwise only a cosine component of the net force is perpendicular to the mean camber line.

The aim of the viscous correction is to make the entire net force perpendicular to the mean camber line as increase in the magnitude of force perpendicular to the mean camber line directly increases the moment of the force acting on the propeller axis; and this in turn increases the torque. Due to this modification, the increase in the torque is higher at the lower J values in comparison to the higher J values as the difference in C_p between the pressure and suction panels (and therefore the magnitude of net force), is high for lower J values as compared to higher J values. Thus, with this mathematical modification we can bridge the gap between the KQ values of the numerical code and the experiment.

In order to make the entire net force normal to the mean camber line, the pressure and suction panels are modified in such a way that their surface normal vectors are always perpendicular to the mean camber line. To achieve this, each panel is projected on the mean camber line. When the panels are projected, the panels located exactly opposite to each other about the mean camber line (called the mirror panels), form a single panel and have the same shape and size but their surface normal vectors are now perpendicular to the mean camber line and point in the opposite directions as shown in Figure 41.

In order to project the panels on the mean camber line, two mirror panels are taken at a time and the mean of the coordinates of the 4 points that form the panel is calculated. Therefore, from two mirror panels a single panel is formed at the mean camber line. This process of calculating mean is repeated on all the panels and thus a pair of mirror panels is used twice, once when the mean is calculated using suction side panels and twice when the mean is calculated using pressure panels. Thus, the total number of panels remains the same, as we have two sets of panels at the mean camber line formed by taking mean of the mirror panels two times and the normal of one faces the suction surface while that of other faces the pressure surface. When the C_p values are applied on the pair of panels, a net force normal to mean camber line then acts from pressure side to suction side, as the value of C_p applied on pressure panels is larger than suction panels.

Moreover, as the panels are projected on the mean camber line, the area of the panels is decreased slightly. This decrease in the panel area is very small ($\approx 0.0005\%$) and does not affect the magnitude of the force acting on the panels. Thus, it is assumed that the area of the panels does not change when projected on the mean camber line, but this assumption holds true only if the number of panels used to calculate the propeller loads are large typically of the order of 300–400 per blade.

After adding the viscous correction to address the flow separation effects, the results were compared again and are shown in Figure 42 below. From the Figure 42, we can see that the results obtained from the numerical code and experiments are very similar and thus, it can be asserted that as far as the separable hydrodynamic loads are concerned, the numerical code Ice-PPB is accurate and precise.

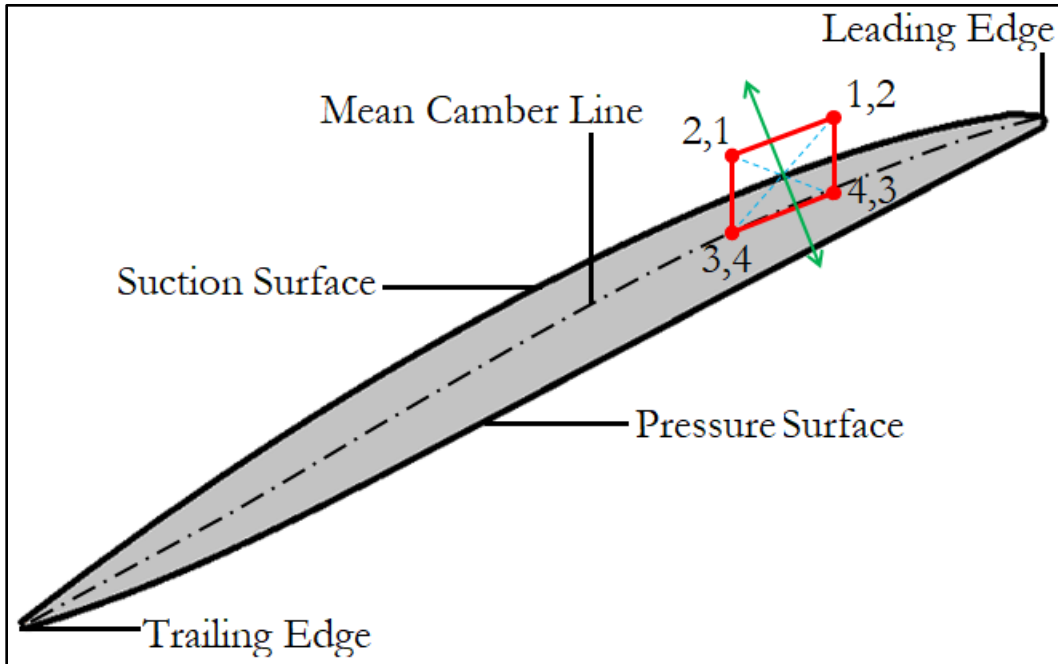


Figure 41: Modification of the Mirror Panels

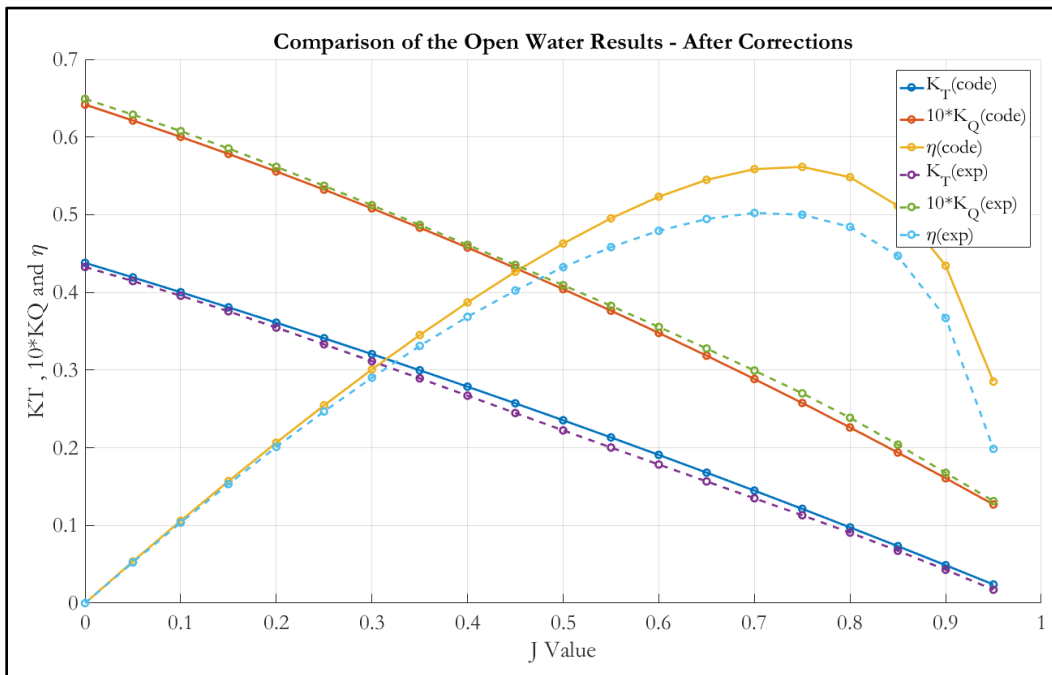


Figure 42: Comparison of the Open Water Results - After Corrections

5.2 Calibration of the Ice Loads

The calibration of the ice loads is mainly concerned with the correct estimation of the empirical factors. As discussed in section 3.3.2 and 3.6, we have four empirical factors i.e. the average weighing factor (w_{avg}), the maximum weighing factor (w_{max}), the empirical factor for crushing (EFC) and the empirical factor for shearing (EFS).

As discussed earlier, a value of 1 is assigned to w_{avg} and a value of 6 is assigned to w_{max} for the calculation of the loads on the shadow panels and leading edge panels respectively. These values largely remain unchanged for different values of ice compressive strength, propeller rpm, leading edge length, etc. [4, 5].

The other two empirical factors, EFC and EFS depend on the properties of the ice used in the experiment. Thus, the value of the empirical factors changes from the air milling to water milling as the ice properties differ for both the experiments (Table 9). The method of estimation of these empirical factors is mentioned below.

5.2.1 Empirical Factor for Crushing

The EFC is estimated to be equal to the ratio of the compressive strength (in MPa) of the ice floe and the strain rate developed in the ice floe during milling. The compressive strength of the ice floe is obtained experimentally, and the strain rate is calculated using the method described below.

The strain (ϵ) is defined as the change in length (Δl) over original length (l) and the strain rate ($\dot{\epsilon}$) is defined as the rate of change in strain. Thus,

$$\epsilon = \frac{\Delta l}{l}, \quad \dot{\epsilon} = \frac{\Delta l}{l \Delta t} = \frac{\Delta l}{\Delta t} \times \frac{1}{l} = \frac{v}{l}$$

In the above equation, v is the indentation speed and the evaluation of the strain rate by this process is quite complex. Moreover, due to high speed phenomenon, the calculation of change in length (Δl) is quite difficult. To overcome this complexity, an empirical formula developed by Cammaert [36] was used to calculate the strain rate. The strain rate is given as,

$$\dot{\epsilon} = \frac{V}{4D} = \frac{2\pi Rn}{4(2R)} = \frac{\pi n}{4}$$

The propeller in the present experiment was running at $n = 9$ Hz for both the air and water milling, and thus, the strain rate is equal to 7.07 s^{-1} . The value of EFC is approximated as,

$$EFC \approx \frac{|Compressive\ Strength|}{|\dot{\epsilon}|} \times 10^{-6}$$

Using the values of compressive strength from Table 9, the value for EFC for air milling is 0.2 and for water milling it is 0.145.

5.2.2 Empirical Factor for Shearing

The EFS is equal to the ratio of the compressive strength and shear strength of the ice floe across a given cross section. Thus,

$$EFS = \frac{\text{Compressive Strength}}{\text{Shear Strength}}$$

The compressive strength data was obtained from the experiments (Table 9); however, any experiment could not be conducted to measure the shear strength. The ratio of compressive and shear strength of the model ice used in HSVA was obtained from the database of HSVA [32] and it was observed that at an average this ratio is equal to 4.27. This value is similar to the one used by Wang [4, 5] in his numerical model. Thus, EFS was assigned a value of 4.27 as compared to a value of 4 used by Wang.

After assigning the values to the empirical factors, the results were obtained using the numerical code Ice-PPB and a comparison was made with the experimental results as shown in Table 13. For comparing the results of the air milling, the numerical code calculates only the ice loads and deletes the hydrodynamic loads and for the water milling, it adds up the hydrodynamic loads (separable and inseparable) and the ice loads.

Table 13: Comparison of Results of Ice Milling

S No	KT Values Experiment	KT Values Code	Error	10*KQ Values Experiment	10*KQ Values Code	Error
Air Milling 01	-0.1326	-0.1208	9.73%	0.7027	0.7836	-10.33%
Air Milling 02	-0.2651	-0.2419	9.59%	1.0560	1.2143	-13.04%
Water Milling 01	0.3126	0.3689	-15.26%	1.7239	1.5548	10.88%
Water Milling 02	0.2010	0.2105	-4.51%	2.3870	2.2634	5.46%

The maximum error between the results is -15.26% while the minimum error is -4.51 %. In general, the errors are between $\pm 9 - 13\%$ which are within the acceptable limits.

On comparing the results of the air milling, it can be asserted that the ice loads calculation algorithm of Ice-PPB is reliable and calculates fairly precise and accurate results.

Furthermore, on comparing the results of the water milling, it can be asserted that the algorithm for calculation of the inseparable hydrodynamic loads by Ice-PPB is also reliable. This is explained in detail in the next section.

5.3 Calibration of the Inseparable Hydrodynamic Loads

The open water and the air milling experiments are used to calibrate the separable hydrodynamic loads and ice loads respectively. From the results obtained from Table 13, it can be seen that the difference between the results obtained from the code and experiment for the open water and ice loads is quite small. Furthermore, it can also be seen that the difference between the total loads obtained from the numerical code and the water milling experiment is also small. Thus we have,

$$\text{Inseparable Hydrodynamic Loads} = \text{Total Loads} - (\text{Separable Hydrodynamic Loads} + \text{Ice Loads})$$

Since, the difference between the numerical and experimental values of total loads, separable hydrodynamic loads and ice loads is small; this directly implies that the difference between the numerical and experimental values of inseparable hydrodynamic loads is also small. Thus, we can assert that the algorithm for the calculation of the inseparable hydrodynamic loads (includes wake region, wake velocity, etc.) by Ice-PPB is reliable, precise and accurate. The inseparable hydrodynamic loads depend on the ice-wake velocity and ice-wake region and it can be inferred that the methods and assumptions used for their calculation are quite accurate. Therefore, no further calibration of any kind is needed as far as the inseparable hydrodynamic loads are concerned.

Thus, the open water test, the air milling and the water milling experiments were used to calibrate the separable & inseparable hydrodynamic loads and the ice loads. After the numerical code was calibrated, numerous results were obtained and effect of various parameters was studied. In the next section, a critical analysis of the results is performed and the influence of various parameters is studied.

5.4 Results and Critical Analysis

The numerical code Ice-PPB was calibrated and the results obtained from the code were quite accurate as seen from Figure 42 and Table 13. Post calibration, the code was used to obtain various results, study the influence of the parameters and perform sensitivity analysis as explained below.

5.4.1 Influence of Parameters

In this section the influence of various parameters on the loads acting on the propeller during its interaction with ice is studied. The various parameters that affect the loading on the propeller are the advance coefficient, RPM, ice compressive strength, depth of cut, etc. The effect of each parameter on the hydrodynamic and ice loads is analyzed.

5.4.1.1 Advance Coefficient

The change in the advance coefficient affects both the hydrodynamic and ice loads. The influence of the advance coefficient on the separable hydrodynamic loads is shown in Figure 42. Using the numerical code Ice-PPB, the influence of the advance coefficient on the total hydrodynamic loads

and ice loads was also studied. The value of J was varied from $J = 0.00$ to $J = 0.95$ at the RPS of 9 Hz. The model parameters on which the calculations were based on are mentioned in Table 14 below. The results are shown in Figure 43.

Table 14: Model Parameters for the study of variation of Hydrodynamic and Ice Loads with J values

S No	Parameter	Value
1.	Advance Coefficient	[0.00,..., 0.95]
2.	Propeller RPS	9 Hz
3.	Ice Compressive Strength	1.50 MPa
4.	Depth of cut	10 mm

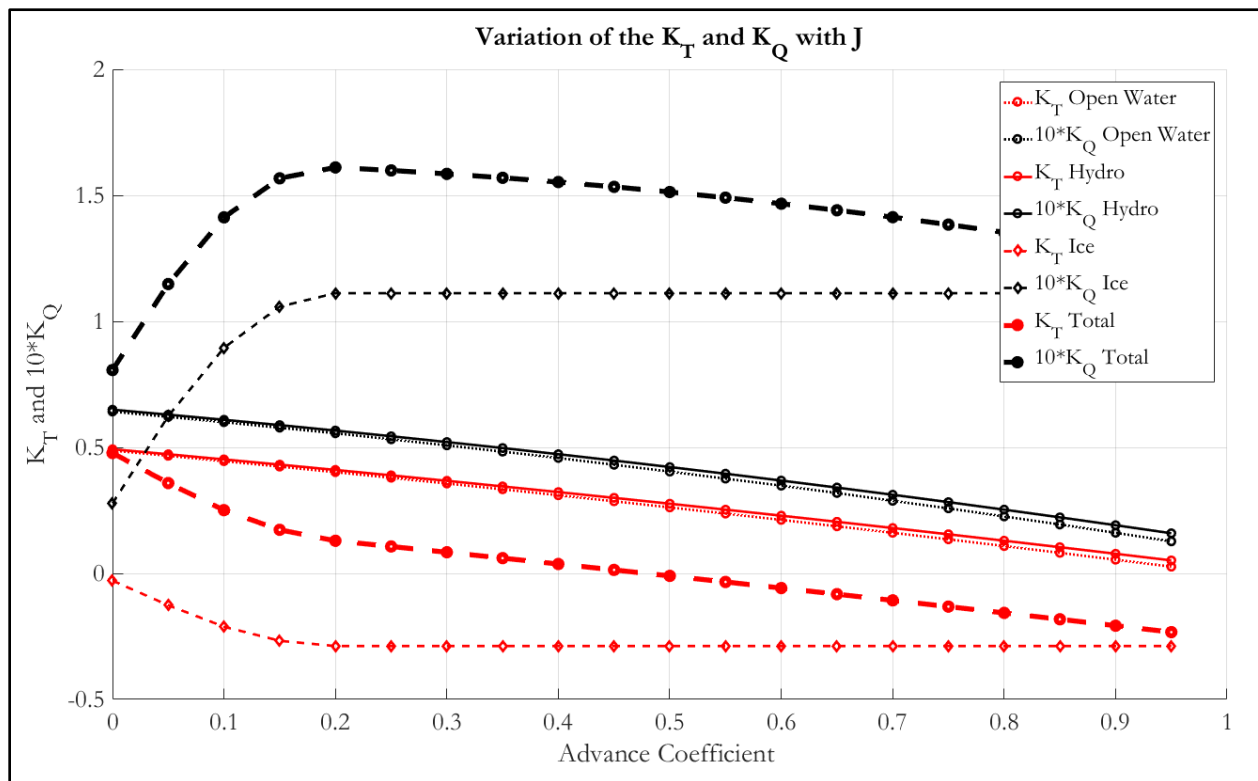


Figure 43: Variation of K_T and K_Q with J (Hydrodynamic and Ice Loads Combined)

The thin dotted red and black lines indicate the values of the separable hydrodynamic loads or the open water loads as shown before in Figure 42. The thin solid red and black lines indicate the values of the hydrodynamic loads (separable + inseparable) and the thin dashed red and black lines indicate the values of the ice loads. The thick dashed red and black lines indicate the values of the total loads. Since for this simulation, the RPS was fixed at 9 Hz and only values of J were changed, the increase in the J value led to the increase in the advance velocity (V_A).

The trend of the open water loads and the hydrodynamic loads is same. As the value of J increases, both the thrust and torque decrease leading to the decrease in the K_T and K_Q values as shown in Figure 43.

The decrease in the hydrodynamic loads on the propeller with the increase in the advance coefficient can be explained by the airfoil theory. At the low values of J , the angle of attack on the propeller blade sections is large leading to the increase in the lift developed on the blade surface. The lift acting on the blade surface has one component in the axial direction and another component in the tangential direction. The component in the axial direction generates the thrust and the component in the tangential direction generates the torque. Higher the lift, higher is the thrust and torque generated by the propeller.

With the increase in the value of J , the angle of attack decreases and as a result at high values of J , the angle of attack is small leading to a decrease in the lift. Consequently, both the thrust and torque decrease. The change in the angle of attack depends only on the J value and for a given J value it is independent of the advance velocity and RPM. Thus, as long as the J value is same, the K_T and K_Q values are also the same irrespective of the value of advance velocity or RPM as shown in Figure 54 of section 5.4.1.4.

Furthermore, the variation of normalized slipstream velocity (ratio of the slipstream velocity and the advance velocity) and normalized acceleration (rate of change of normalized slipstream velocity) along the propeller race at different J values is shown in Figure 44 and Figure 45 respectively. The values of the slipstream velocity are obtained from the PPB as explained in section 3.5.2.

The results of Figure 44 and Figure 45 are in coherence with the results of Figure 43. At low values of the advance coefficient, the thrust and torque generated are high and as a result the increase in the normalized slipstream velocity is also high. The steep increase in the velocity implies that the velocity induced by the propeller is high.

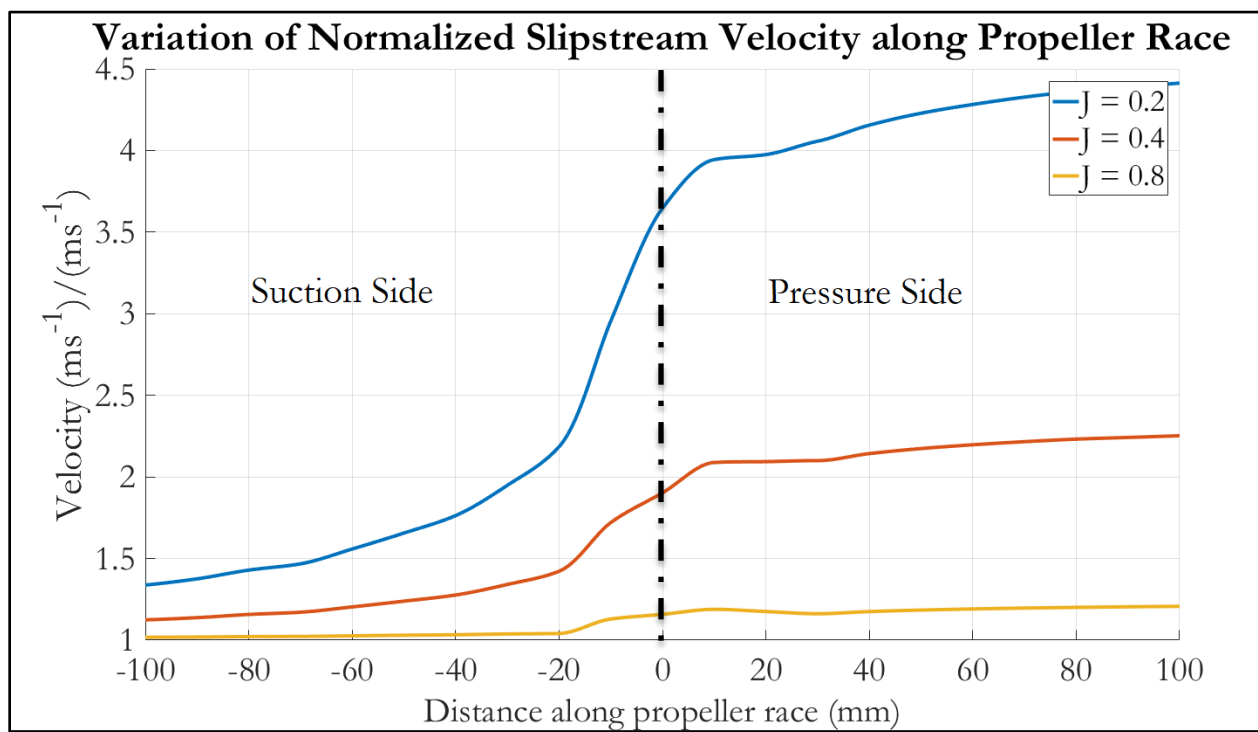


Figure 44: Variation of Normalized Slipstream Velocity along Propeller Race

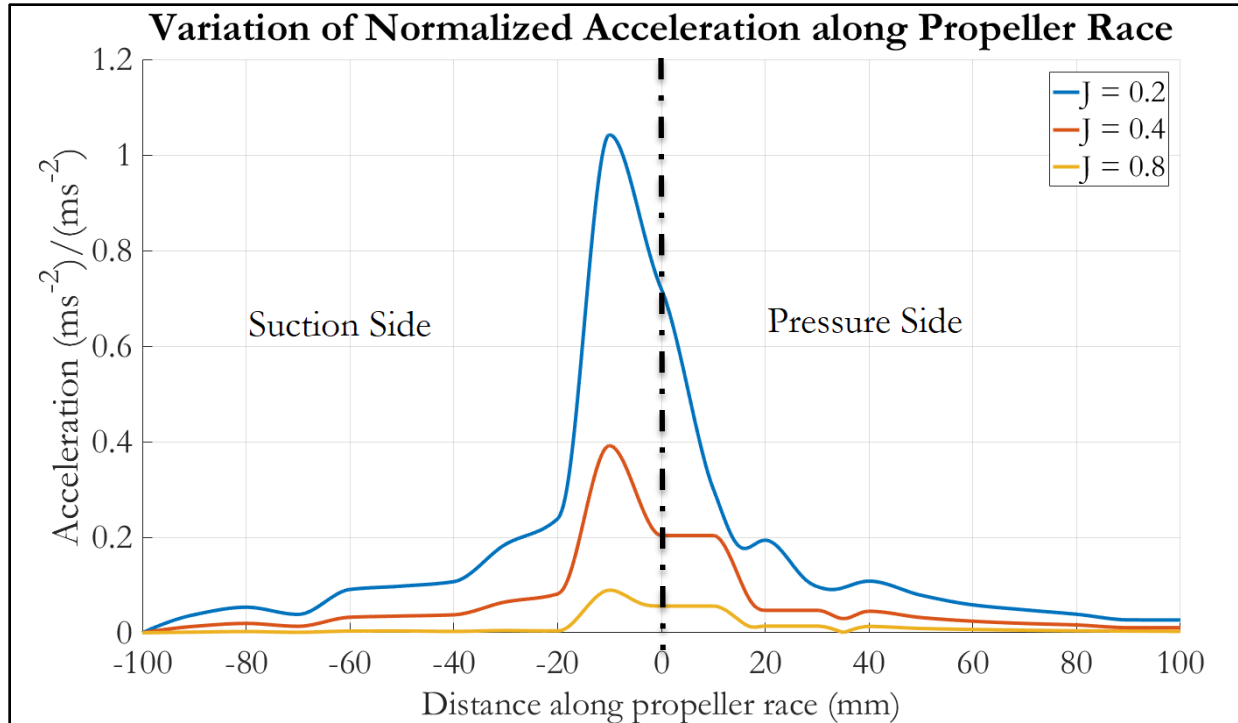


Figure 45: Variation of Normalized Acceleration along Propeller Race

Therefore, the normalized acceleration is high at low J values and decreases with the increase in the value of J due to decrease in the thrust and torque acting on the propeller, as shown in Figure 45. The normalized slipstream velocity and the normalized acceleration are dependent on the values of J and are independent of the propeller RPM and advance velocity.

In the present study, the value of the RPM was fixed, and the increase in the advance velocity led to the increase in the value of J . Thus, in other words, at a given RPM of the propeller, the hydrodynamic loads decrease with the increase in the advance velocity.

Furthermore, we can see from Figure 43 that the total hydrodynamic loads are slightly higher than the open water loads due to the presence of the inseparable hydrodynamic loads. As discussed in section 3.4.1, the advance velocity decreases due to the presence of the ice wake, this in turn decreases the value of J as the RPM of the propeller does not change due to the presence of the ice. Thus, as the J value is reduced, the loads on the propeller are higher.

On the other hand the variation of ice loads shows a different trend. The magnitude (absolute value) of the ice loads first increases with the increase in the value of J and then attains a constant value. From the section 3.6 and 5.2.1, it can be seen that for a constant RPM, the magnitude of C_p and T_w due to ice milling is independent of advance velocity and therefore the advance coefficient.

This trend however, is explained by the shadow effect as the number of shadow panels that are selected is dependent on the value of J as shown in Figure 21. For a given RPM and depth of cut, as the value of J increases, the forward speed of the ice floe increases and the number of shadow panels in contact with it also increases.

However, as the value of J is increased above a certain limit (0.2 in this case) there is no further increase in the number of shadow panels for a given depth of cut (10mm in this case). This phenomenon is shown in Figure 46. From Figure 46 it can be seen that for a depth of cut of 10 mm, there is no increase in the number of shadow panels (shown in black) beyond $J = 0.2$. Thus, as the J value is increased further, no new shadow panels are selected and the ice loads attain a constant value.

Furthermore, if the depth of cut is increased to say, 30 mm then after $J = 0.65$ no new shadow panels are selected as shown in Figure 47. This variation in the selection of the shadow panels with the depth of cut is a result of the pitch of the propeller. Due to the non-zero pitch of the propeller, the panels located at different radii of the propeller are at a different distance from the $y-z$ plane of the propeller disc.

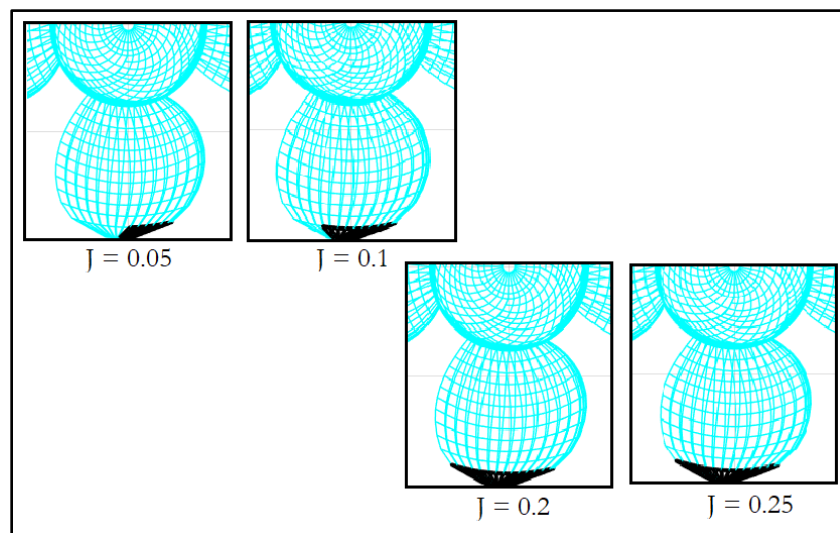


Figure 46: Variation of Shadow Panels (black) with J Value at 10 mm DOC

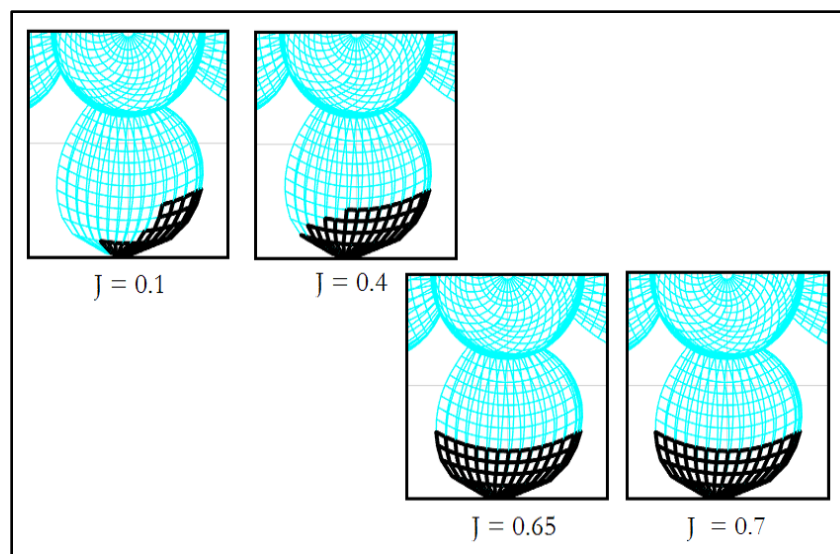


Figure 47: Variation of Shadow Panels (black) with J Value at 30 mm DOC

Figure 48 shows the variation of K_T and K_Q due to ice loads at a depth of cut of 30 mm. All the other parameters were same as in the previous case including the propeller RPM and ice compressive strength.

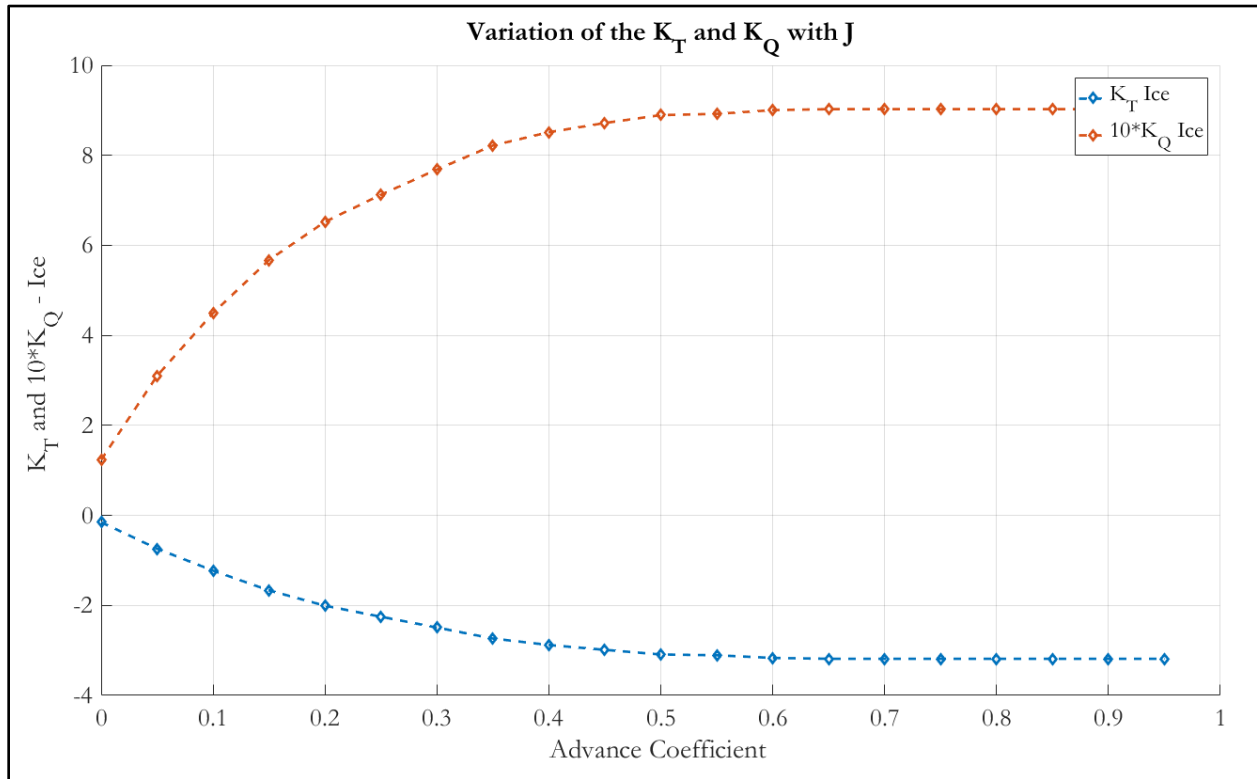


Figure 48: Variation of Ice Loads with J Value at 30 mm DOC

The results of Figure 48 are in coherence with the results of Figure 47. After $J = 0.65$, the ice loads are constant as the number of shadow panels remains constant. Moreover, the values of K_T and K_Q at this depth of cut (1/3 of propeller radius) and compressive strength are very high and can cause serious damage to the propeller.

Finally, from Figure 43 it can be seen that the total loads are equal to the sum of the hydrodynamic loads and the ice loads. In case of torque coefficient (K_Q), the total load value first increases as the increase in the ice loads is larger in magnitude than the decrease in hydrodynamic loads. When the ice loads attain a constant value, the total loads then decrease with the increase in the value of J due to the decrease in the hydrodynamic loads. In case of the thrust coefficient (K_T), the total load value first decreases rapidly (absolute value increases) due to decrease in the ice loads, and when the ice loads attain a constant value, the total loads then decrease slowly with the increase in the value of J due to the decrease in the hydrodynamic loads

5.4.1.2 Depth of Cut

The depth of cut (DOC) influences both the hydrodynamic loads and the ice loads. The hydrodynamic loads change due to the change in the inseparable hydrodynamic loads. The inseparable hydrodynamic loads depend on the ice–wake field and this wake field changes with the

change in the depth of cut. For this study the depth of cut was varied from 5 mm to 30 mm and the model parameters on which the calculations were based on are mentioned in Table 15 below. The results are shown in Figure 49 and Figure 51.

Table 15: Model Parameters for the study of variation of Hydrodynamic and Ice Loads with DOC

S No	Parameter	Value
1.	Advance Coefficient	0.2
2.	Propeller RPS	9 Hz
3.	Ice Compressive Strength	1.50 MPa
4.	Depth of Cut	[5,...,30] mm

From Figure 49 it can be seen that the variation in hydrodynamic loads is quite small with respect to the change in depth of cut. The change in depth of cut only affects the inseparable hydrodynamic loads. The contribution of these loads to the total hydrodynamic loads is very small and therefore the total hydrodynamic loads are affected marginally with the change in the depth of cut.

Nonetheless, the total hydrodynamic loads increase with the increase in the depth of cut owing to the increase in the inseparable hydrodynamic loads. This is due to the increase in the ice-wake region as shown in Figure 50.

As the depth of cut is increased, a larger portion of the propeller disc is blocked by the ice floe leading to the expansion of the ice wake field. With the increase in the ice wake field, the average advance velocity at a given y - z plane is reduced while the propeller RPM remains unchanged. Due to the decrease in the advance velocity at a given RPM, the hydrodynamic loads increase as explained in section 5.4.1.1.

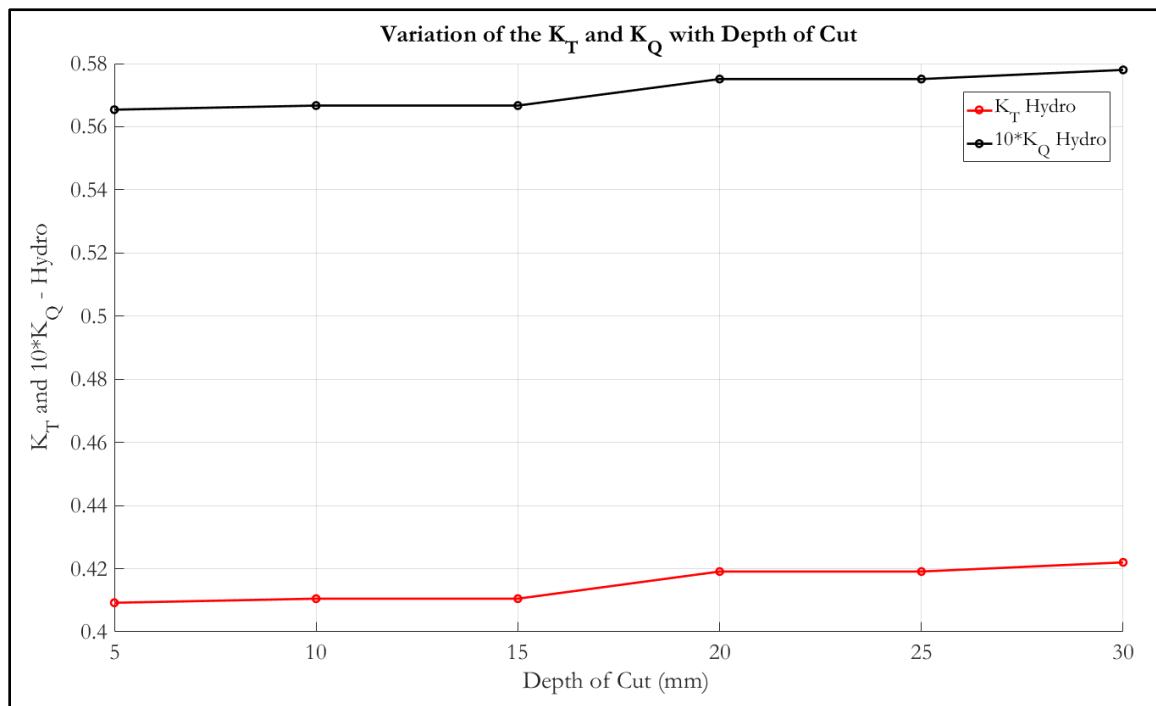


Figure 49: Variation of Hydrodynamic Loads with DOC

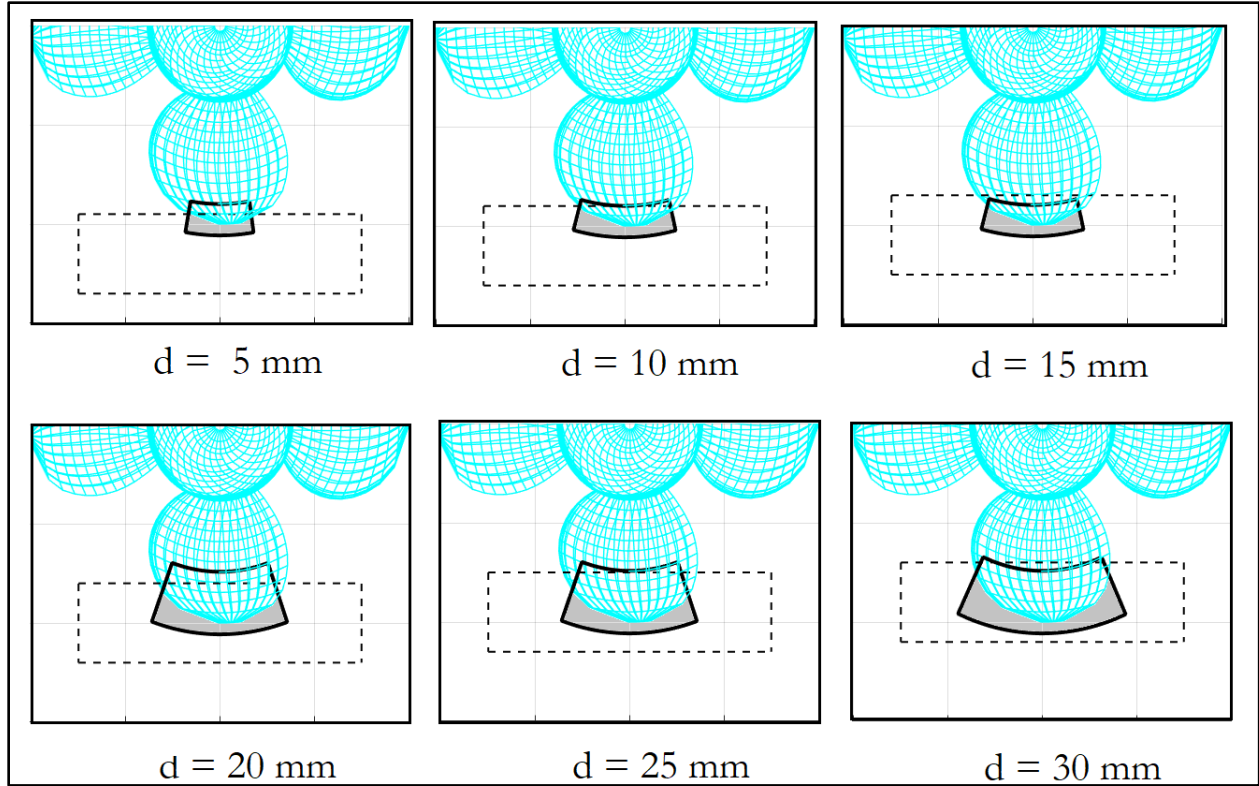


Figure 50: Variation of Ice wake Field with DOC

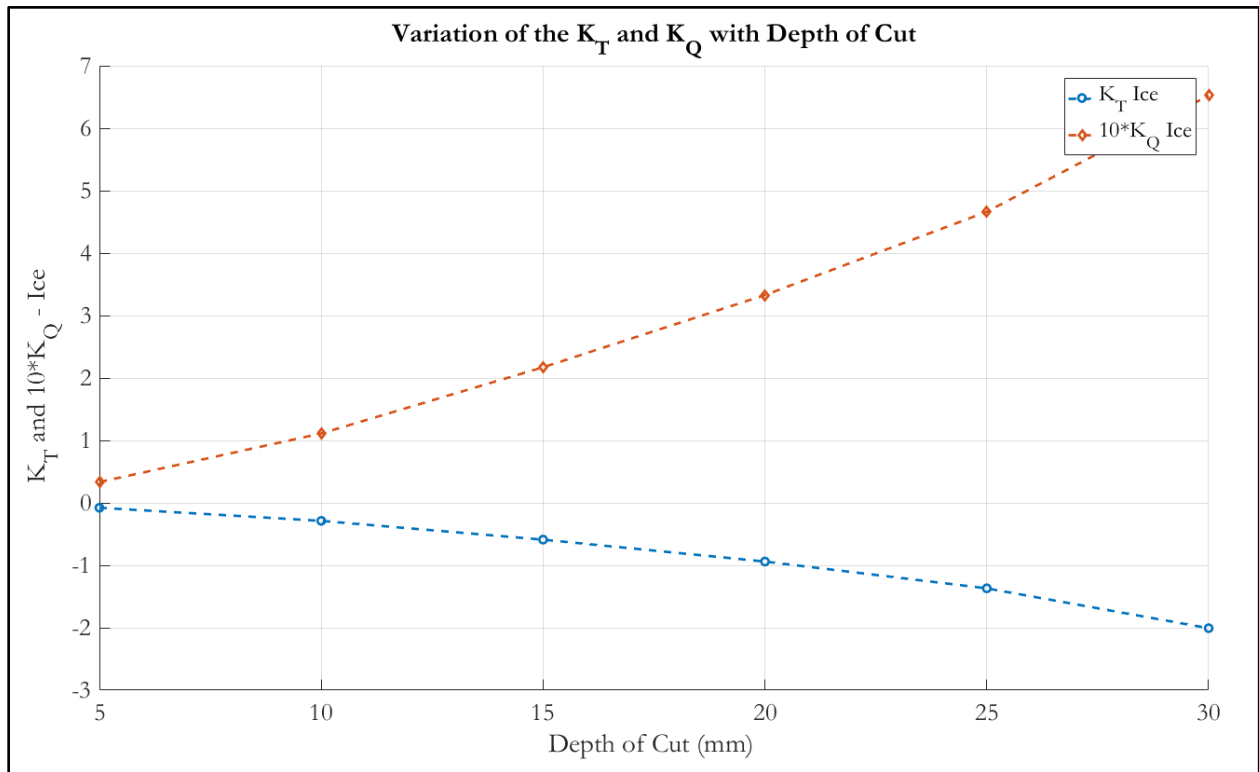


Figure 51: Variation of Ice Loads with DOC

The magnitude (absolute value) of the ice loads increases rapidly with the increase in the depth of cut as shown in Figure 51. This rapid increase is due to the increase in the number of panels that participate in the ice milling process. From Figure 50 it can be seen that with the increase in the depth of cut, the number of blade panels that receive the ice loads increases significantly due to the shape of the propeller blades and position of ice floe.

After the depth of cut of 20 mm, the current compressive strength (1.50 MPa) and advance coefficient (0.2) lead to a severe loading on the model propeller. In most cases, the propeller will either stop rotating or even the blades might bend.

5.4.1.3 Ice Compressive Strength

From the equations 1– 4 used to calculate the ice loads on the propeller as mentioned in section 3.6, it can be seen that the magnitude of the ice loads increases with the increase in the ice compressive strength. In order to study the variation of ice loads with ice compressive strength, the ice compressive strength was varied from 0.5 MPa to 4 MPa. The model parameters on which the calculations were based on are mentioned in Table 16 below. The results are shown in Figure 52.

Table 16: Model Parameters for the study of variation of Ice Loads with Ice Compressive Strength

S No	Parameter	Value
1.	Advance Coefficient	0.2
2.	Propeller RPS	9 Hz
3.	Ice Compressive Strength	[0.5,...,4] MPa
4.	Depth of Cut	10 mm

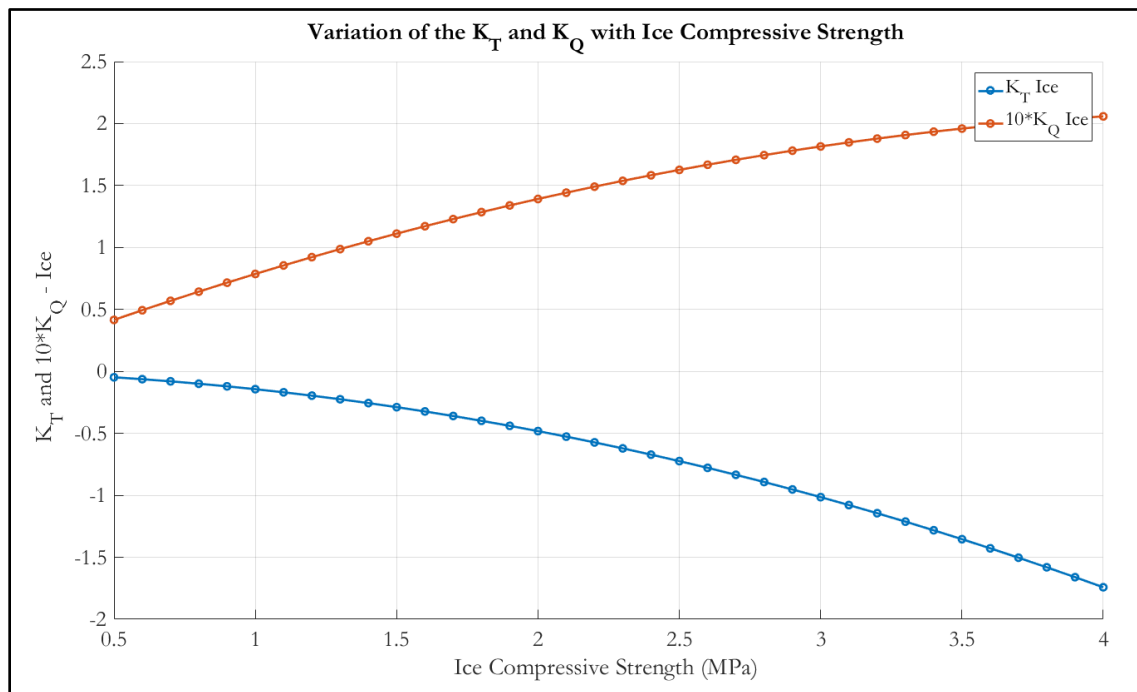


Figure 52: Variation of Ice Loads with Ice Compressive Strength

As seen from Figure 52, the variation of the ice loads with the ice compressive strength is non-linear and this non-linear behavior is attributed to the empirical factor for crushing (EFC) as explained below.

From the section 3.6 we have,

$$P_{crushing} = w \times EFC \times S_{ice} \quad (1)$$

From the section 5.2.1 we have,

$$EFC \approx \left| \frac{S_{ice}}{\dot{\epsilon}} \right| \times 10^{-6} \quad (5)$$

On combining equation 1 and 5, we have,

$$P_{crushing} \approx w \times \frac{S_{ice}^2}{\dot{\epsilon}} \times 10^{-6}$$

$$C_p \approx \frac{\left(w \times \frac{S_{ice}^2}{\dot{\epsilon}} \times 10^{-6} \right)}{0.5 \times \rho \times (\omega R)^2} \quad (6)$$

Where,

w = Empirical weighing factor

EFC = Empirical Factor for Crushing

S_{ice} = Compressive Strength of Ice

ρ = Density of water

ω = Angular Frequency of the propeller rotation

R = Radius of the propeller

$\dot{\epsilon}$ = Strain Rate

From equation 6, it can be seen that the relationship between the C_p due to ice loads and the ice compressive strength is parabolic in nature and this explains the non-linear increase in the magnitude of the ice loads with the increase in the ice compressive strength. For a constant value of EFC, the ice loads vary linearly with the ice compressive strength as shown in Figure 53.

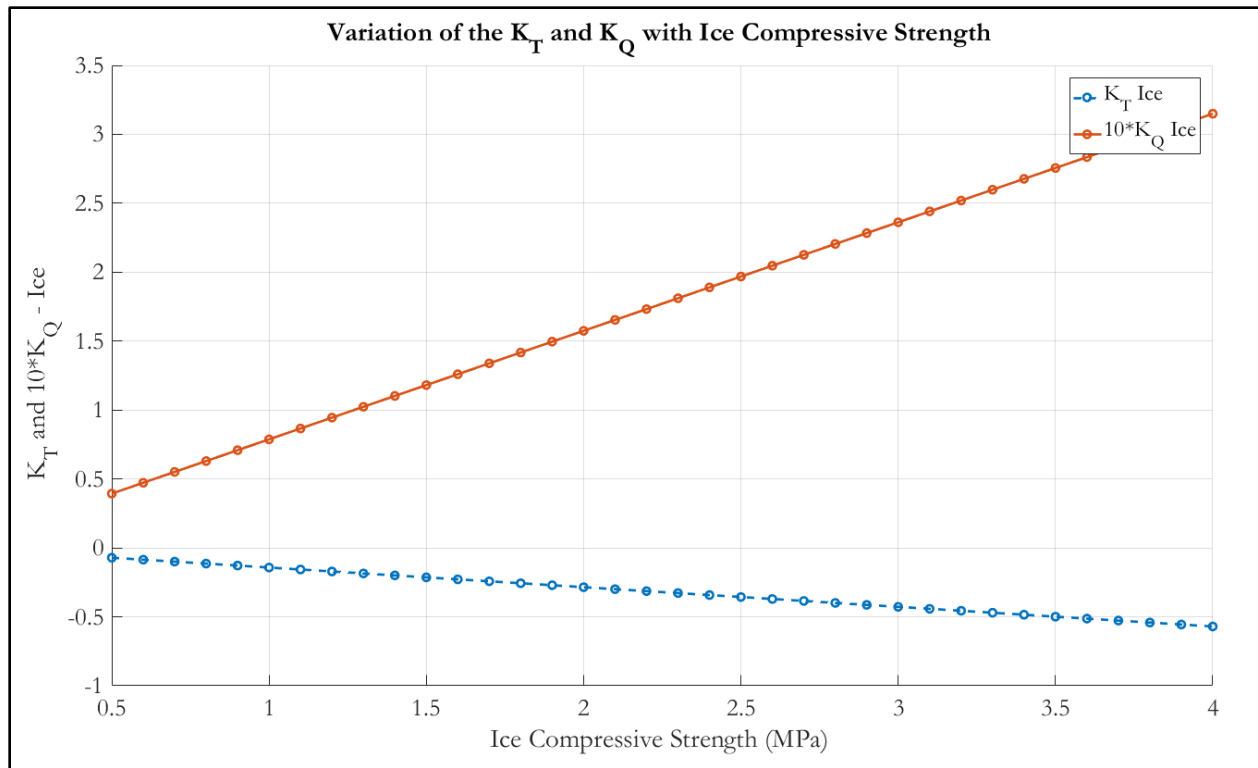


Figure 53: Variation of Ice Loads with Ice Compressive Strength at constant EFC of 0.14

5.4.1.4 Propeller RPM

The propeller RPM has an influence on the hydrodynamic loads as well as the ice loads. At a constant advance velocity, a decrease in the propeller RPM increases the J value and with the increase in the J value, the hydrodynamic loads on the propeller decrease as explained in section 5.4.1.1. In other words, at a constant advance velocity, an increase in the propeller RPM increases the hydrodynamic loads and decrease in the propeller RPM decreases the hydrodynamic loads.

However, as long as the J values are same, the hydrodynamic loads are also same even though we have different values of advance velocity and RPM as shown in Figure 54. This is because, as explained in section 5.4.1.1, the angle of attack on the propeller blade sections is solely dependent on the J value. The value of angle of attack determines the amount of lift generated on the blade surface and therefore the values of the thrust and torque.

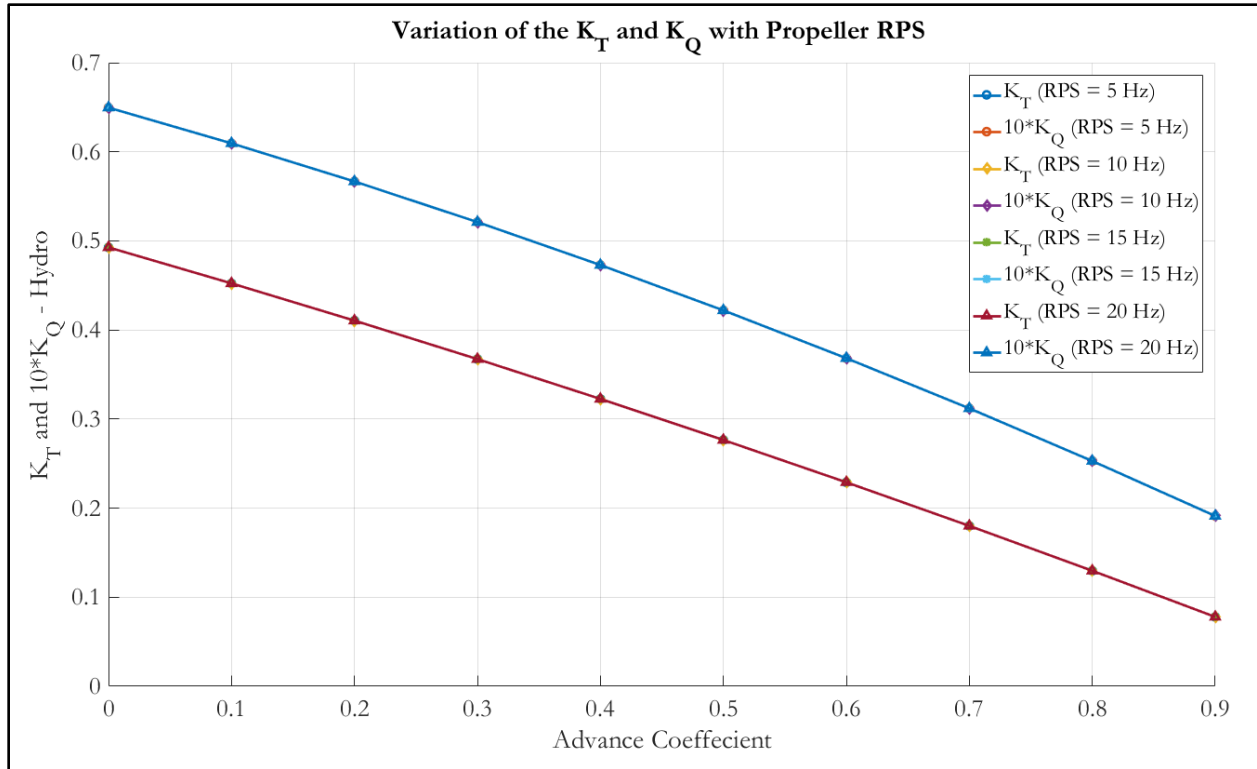


Figure 54: Variation of Hydrodynamic Loads with Propeller RPS

The behavior of the ice loads on the other hand is quite different from that of the hydrodynamic loads. For this study, the value of J was varied from $J = 0.0$ to $J = 0.90$ and the propeller RPS was varied from 5 Hz to 20 Hz. The model parameters on which the calculations were based on are mentioned in Table 17 below and the results are shown in Figure 55.

Table 17: Model Parameters for the study of variation of Hydrodynamic and Ice Loads with RPM

S No	Parameter	Value
1.	Advance Coefficient	[0.0,..., 0.90]
2.	Propeller RPS	[5,..., 20] Hz
3.	Ice Compressive Strength	1.50 MPa
4.	Depth of Cut	10 mm

From Figure 55 it can be seen that at a given value of advance coefficient, the magnitude of the ice loads decreases with the increase in the value of the RPM (or RPS). However, for each value of RPM, the trend is the same; the ice loads increase up to $J = 0.2$ and then attain a constant value as for the given value of depth of cut (10 mm) no new shadow panels are included beyond $J = 0.2$. At a constant J value, the change in the RPM does not influence the number of shadow panels selected as it depends on the ratio of advance velocity and RPM as explained in section 3.6.1.

At a given J value, the decrease in the magnitude of the ice loads with the increase in the RPM is attributed to the strain rate. The strain rate increases with the increase in the RPM (or RPS (n)) and as a result the empirical factor for crushing is decreased. From section 5.4.1.3 and 5.2.1 we have,

$$C_p \approx \frac{\left(w \times \frac{S_{ice}^2}{\dot{\epsilon}} \times 10^{-6} \right)}{0.5 \times \rho \times (\omega R)^2}, \quad \dot{\epsilon} = \frac{\pi n}{4}$$

$$C_p \approx \frac{4(w \times S_{ice}^2 \times 10^{-6})}{0.5 \times \pi \times n \times \rho \times (\omega R)^2}$$

The increase in the RPM reduces the value of C_p due to the ice loads and thereby reducing the magnitude of the ice loads acting on the propeller. This result confirms the usual practice of operating the propellers at high RPM in ice.

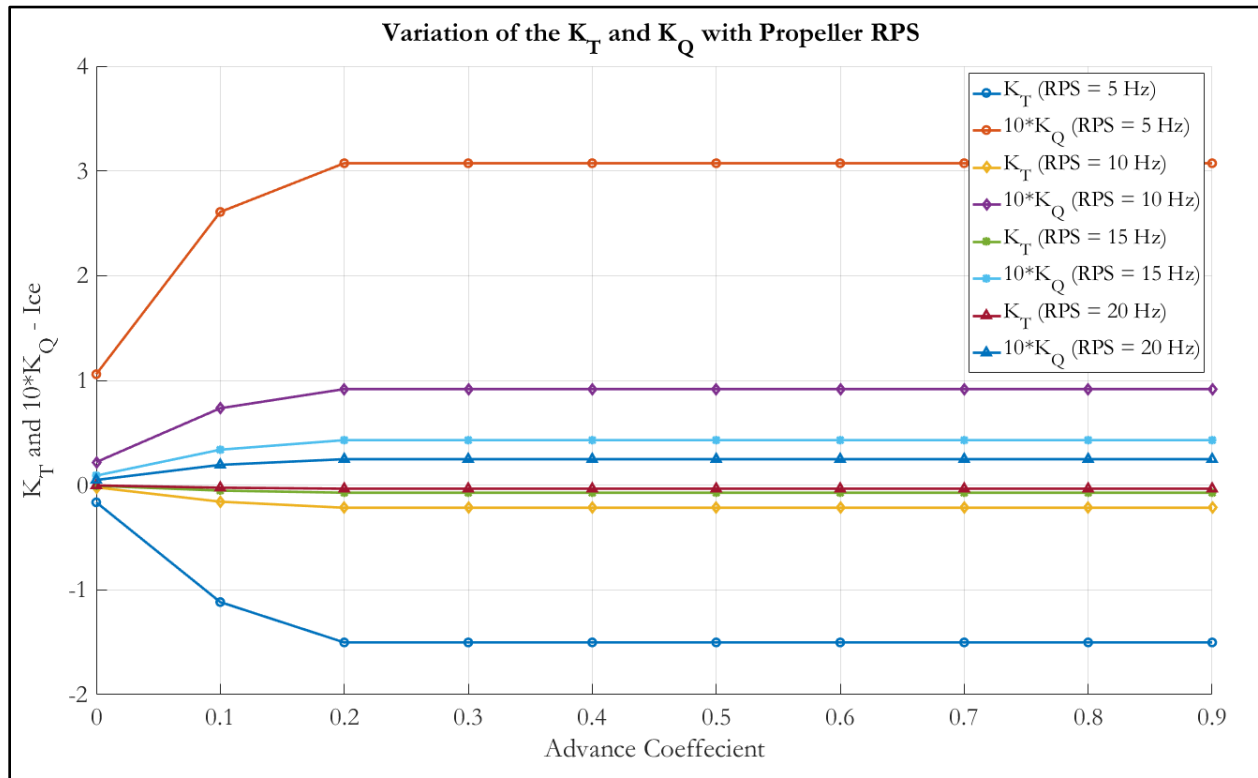


Figure 55: Variation Ice Loads with Propeller RPS

5.4.2 Sensitivity Analysis

The numerical code Ice-PPB uses certain empirical factors to calculate the ice loads and in order to study the influence of each empirical factor on the results, a sensitivity analysis was performed. The sensitivity analysis was performed on all the 4 empirical factors, i.e., EFC, EFS, W_{avg} and W_{max} . The model parameters for this analysis are shown in Table 18.

Table 18: Model Parameters for the Sensitivity Analysis of Empirical Factors

S No	Parameter	Value
1.	Advance Coefficient	0.2
2.	Propeller RPS	9 Hz
3.	Ice Compressive Strength	1.50 MPa
4.	Depth of Cut	10 mm
5.	EFC	0.14
6.	EFS	4.00
7.	W_{avg}	1
8.	W_{max}	6

In order to perform the sensitivity analysis of each empirical factor, the value of that empirical factor was varied, while all the other values were kept same as mentioned in Table 18.

a) Empirical Factor for Crushing: The highest sensitivity of the code towards EFC is because EFC is used to calculate the coefficient of pressure (C_p) on both the shadow panels and the leading edge panels. Moreover, when EFC is used to calculate the C_p on leading edge panels, it is multiplied by a high value of W_{max} (value of 6 for Figure 56). If the number of shadow panels is reduced either by reducing the J value or depth of cut, or if the value of W_{max} is reduced, the code will be less sensitive to the value of EFC as shown in Figure 57.

From Figure 57, it can be seen that there is negligible change in thrust with the change in EFC, when only the value of W_{max} is changed. This is because the factor W_{max} is multiplied to EFC only when the C_p on leading edge panels is calculated. Since, the leading edge panels mainly contribute to torque and have negligible influence on the thrust; therefore as W_{max} is reduced, the change in thrust coefficient is insignificant and the change only manifests in the torque coefficient.

The change in the J value and the depth of cut changes both the thrust and torque values with EFC. The change in the J values changes the number of shadow panels. Since, EFC is used to calculate the C_p on all the panels; a decrease in the number of shadow panels significantly reduces the influence of EFC on the final results. The change in depth of cut has maximum effect as change in the depth of cut changes both the number of shadow panels and the leading edge panels in contact with ice floe. The sensitivity of EFC is therefore subjected to change depending on the relative position of ice and the propeller and the advance coefficient.

The decrease in the sensitivity of the code with respect to EFC with the decrease in the depth of cut, J value and W_{max} value, is characterized by the decrease in the slope of ΔKT and ΔKQ in Figure 57.

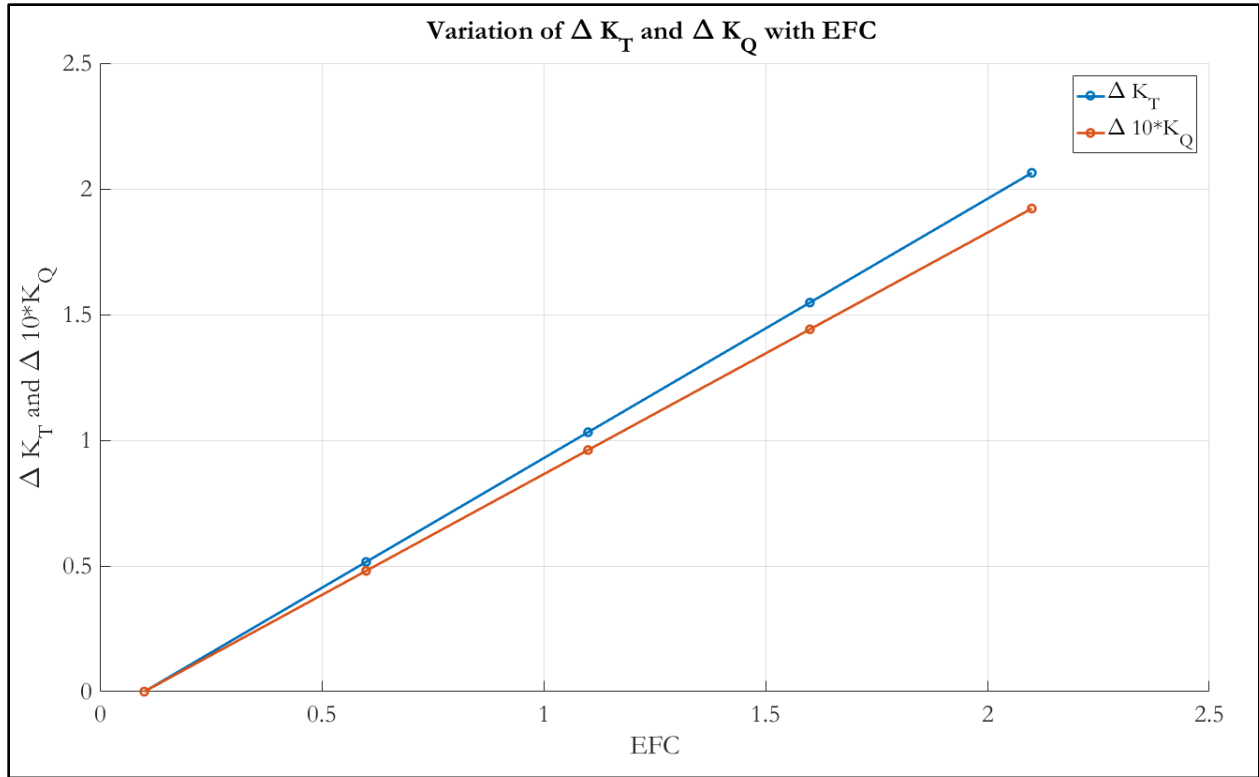


Figure 56: Change in Ice Loads with EFC

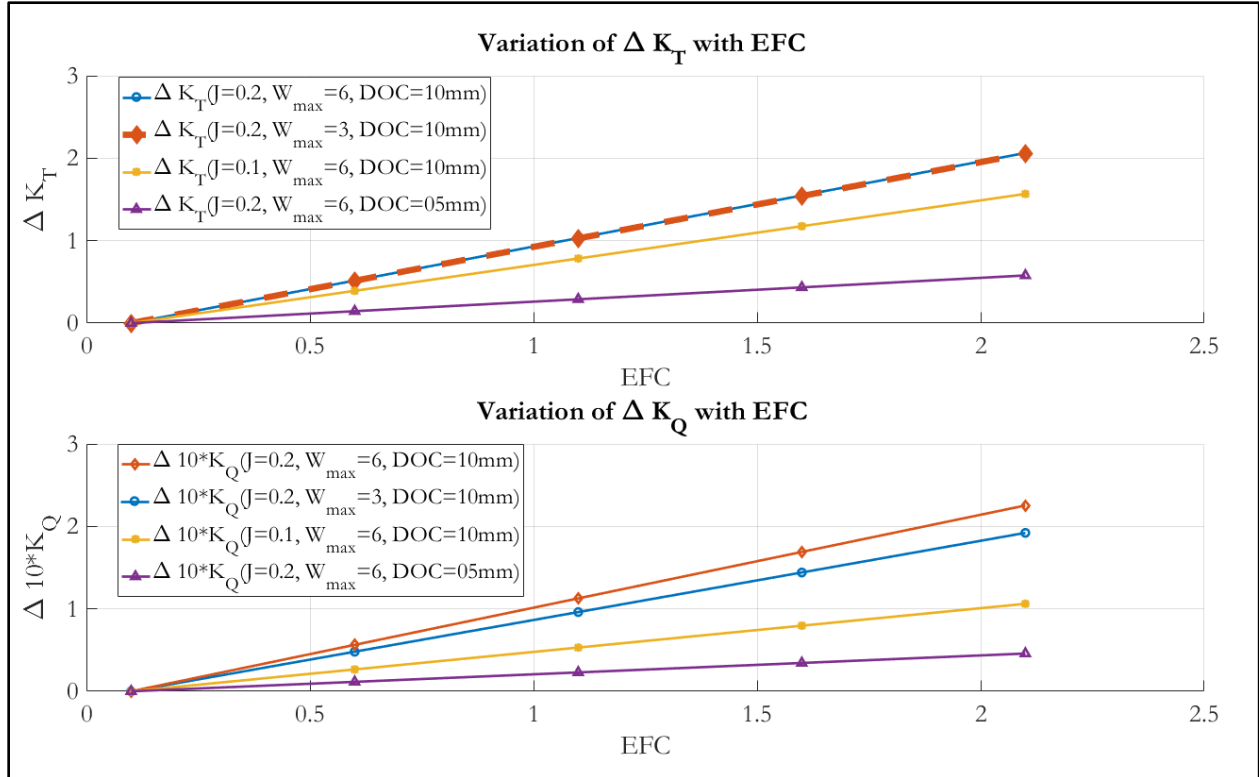


Figure 57: Influence of Parameters on the Sensitivity of EFC

b) Average Weighing Factor: The second highest sensitivity of the code is towards the empirical factor W_{avg} as shown in Figure 58. This factor is used to calculate the C_p on all the shadow panels and due to the large number of shadow panels involved for this J value (0.2) and depth of cut (10 mm), the sensitivity of the code with respect to W_{avg} is high. If the number of shadow panels are reduced either by reducing the depth of cut or J value, the sensitivity of the code with respect to W_{avg} will also be reduced as shown in Figure 59.

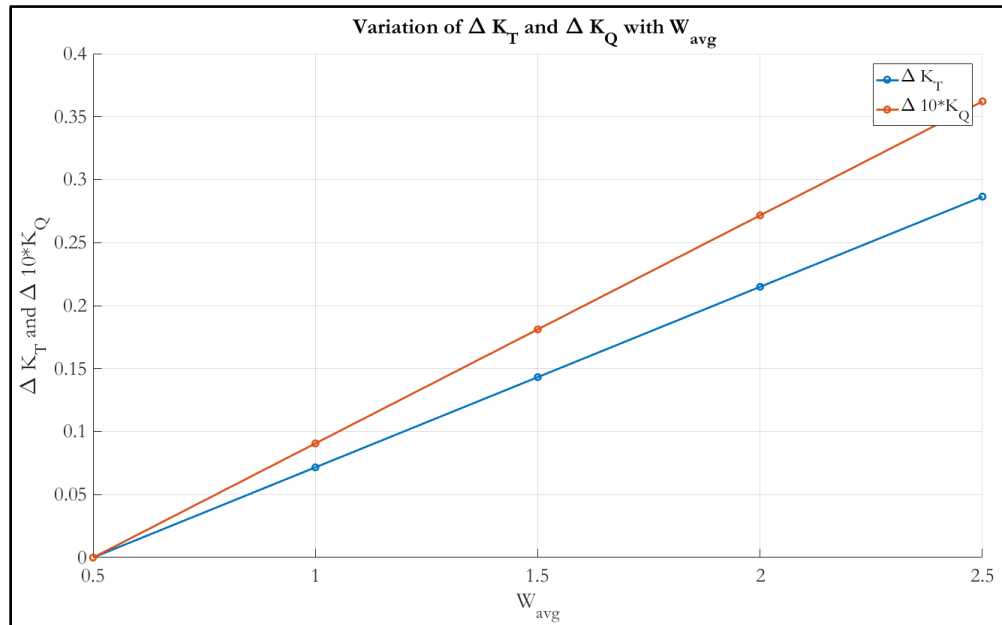


Figure 58: Change in Ice Loads with W_{avg}

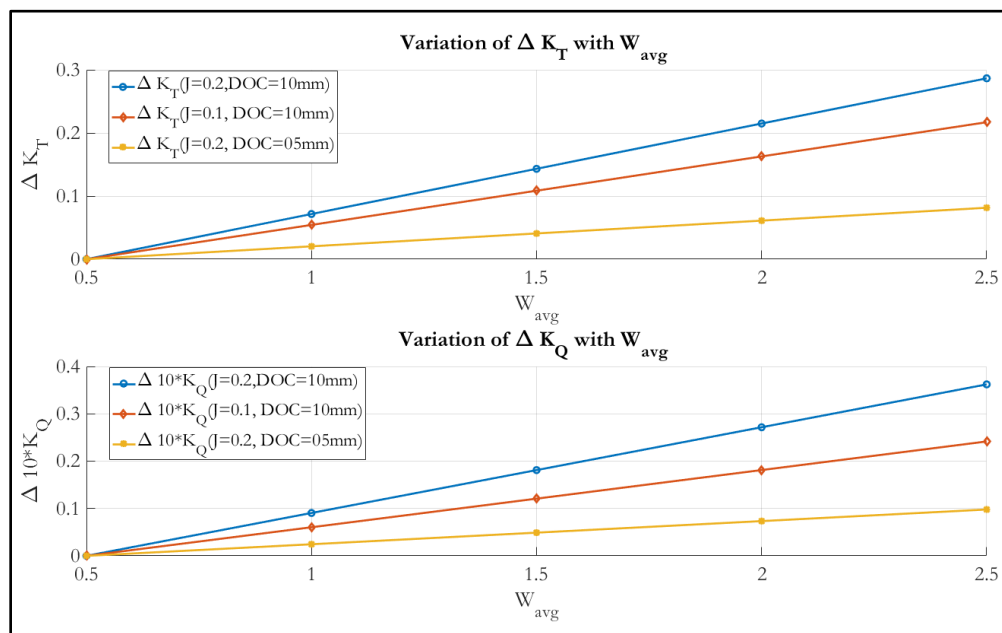


Figure 59: Influence of Parameters on the Sensitivity of W_{avg}

The decrease in the sensitivity of the code with respect to W_{avg} with the decrease in depth of cut and J value, is characterized by the decrease in the slope of ΔKT and ΔKQ in Figure 59.

c) **Empirical Factor for Shearing:** The EFS is used to calculate shear force (or Tw) on all the panels and is not multiplied by any weighing factor and thus has a reduced effect on the outcome of the code. Since, the shear force is mainly responsible for torque and has minimum effect on the thrust, the torque coefficient is mainly affected by the change in the value of EFS and the thrust coefficient remains almost constant as shown in Figure 60.

An important point to note here is that the KT and KQ values decrease with the increase in the value of EFS. This happens because the pressure due to shearing and thus Tw decreases with the increase in EFS as shown in equation 2 and 4 in section 3.6.

Similar to the first two empirical factors, reduction in the value of J or depth of cut reduces the number of shadow panels and leading edge panels thereby reducing the sensitivity of the code with respect to EFS as shown in Figure 61.

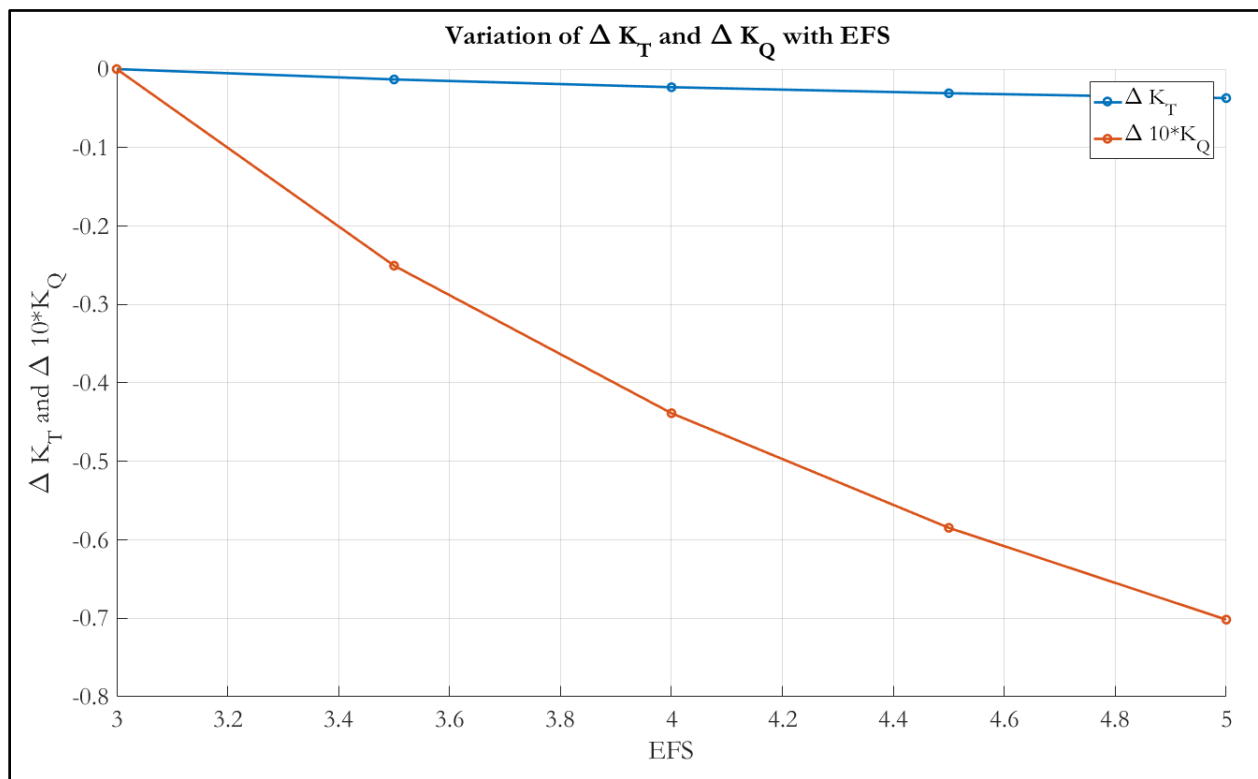


Figure 60: Change in Ice Loads with EFS

From Figure 61 it can be seen that the slope of ΔKT is ≈ 20 times less than that of ΔKQ and this is in coherence with the results of Figure 60. The code is much more sensitive to EFS for torque calculations as compared to thrust calculations.

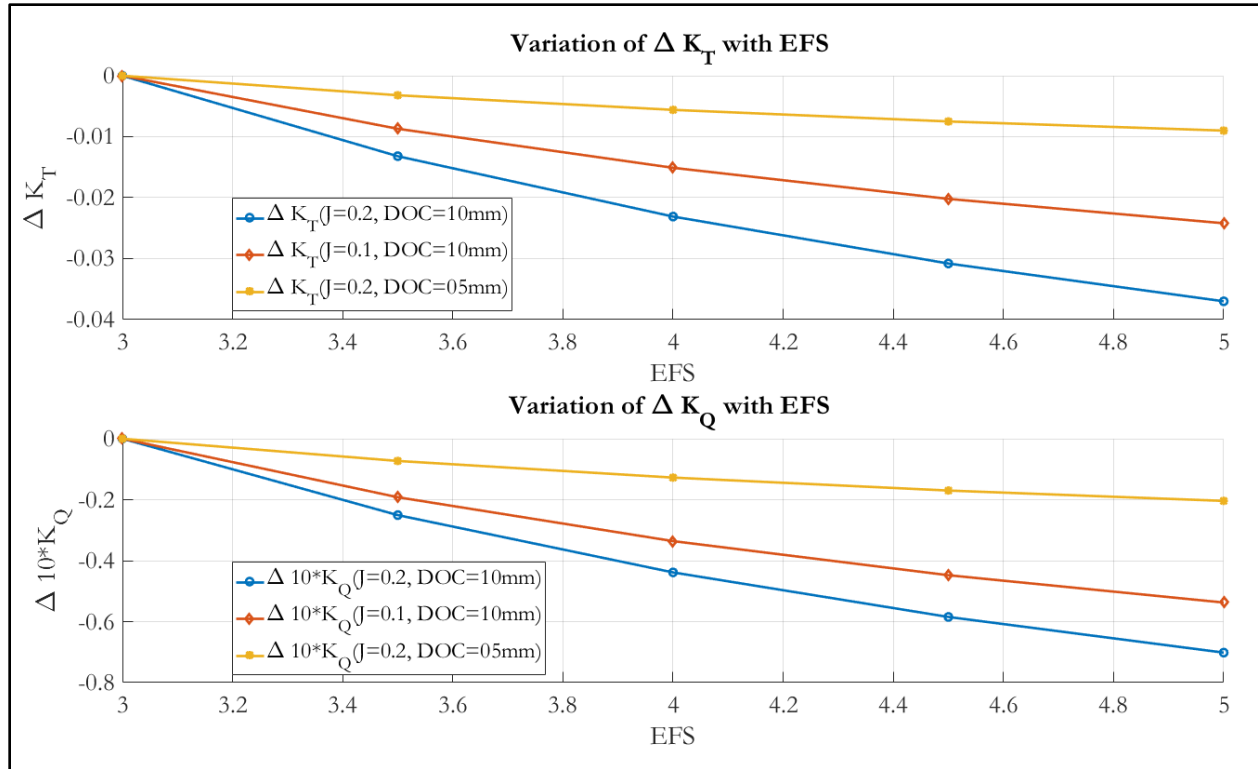


Figure 61: Influence of Parameters on the Sensitivity of EFS

d) **Maximum Weighing Factor:** The least sensitivity of the code towards W_{max} is due to two reasons. Firstly, W_{max} is used to calculate the C_p only on the leading edge panels. As the number of leading edge panels is much smaller than the shadow panels, the effect of W_{max} gets diluted. Secondly, the value of W_{max} is multiplied by the value of EFC, which has a small value of 0.14 in Figure 62. This further reduces the effect of W_{max} and thus we have a very small value of the slope of ΔK_T and ΔK_Q . Furthermore, the effect on the thrust is even more negligible as leading edge panels contribute mainly to the torque and not the thrust. This is reflected in the very small slope of ΔK_T values.

If the value of EFC increases, the sensitivity of the code with respect to W_{max} also increases, as shown in Figure 63. The sensitivity decreases with the decrease in the depth of cut as due to the decrease in the depth of cut the number of leading edge panels decreases.

On the other hand, the change in the value of J will not affect the sensitivity because the change in the value of J changes only the shadow panels and has no influence on the number of leading edge panels in contact with ice. Thus, the slope of ΔK_T and ΔK_Q remains unchanged as shown in Figure 63.

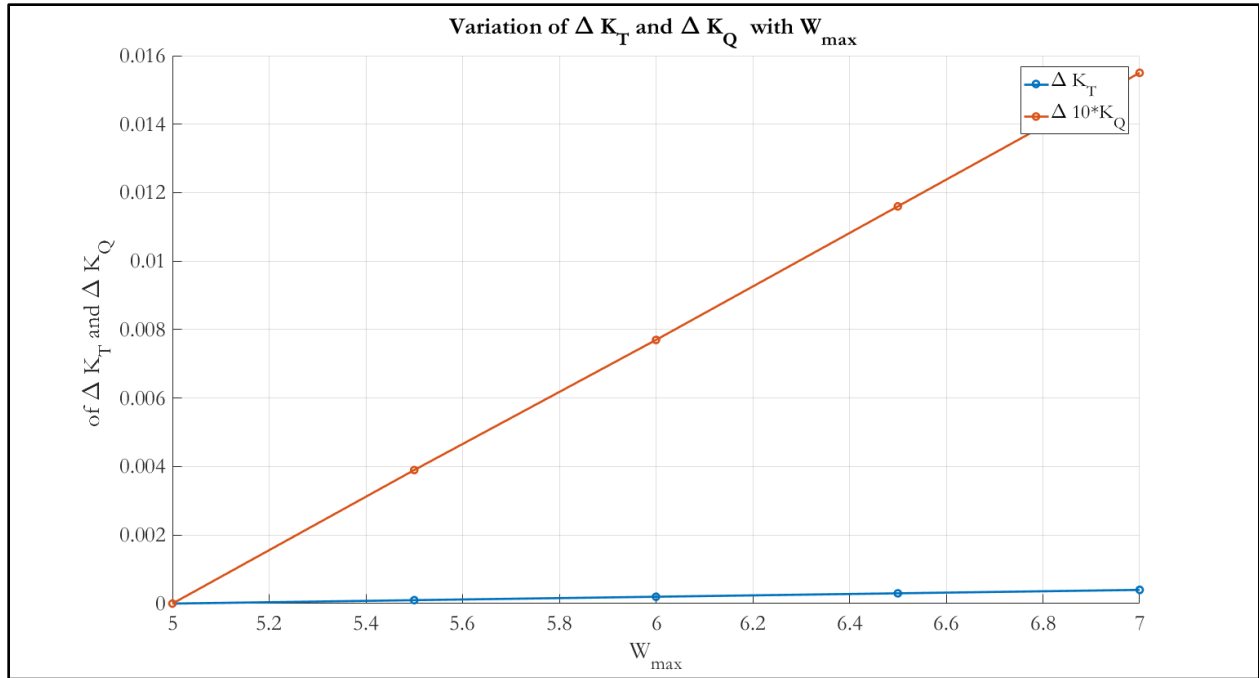


Figure 62: Change in Ice Loads with W_{max}

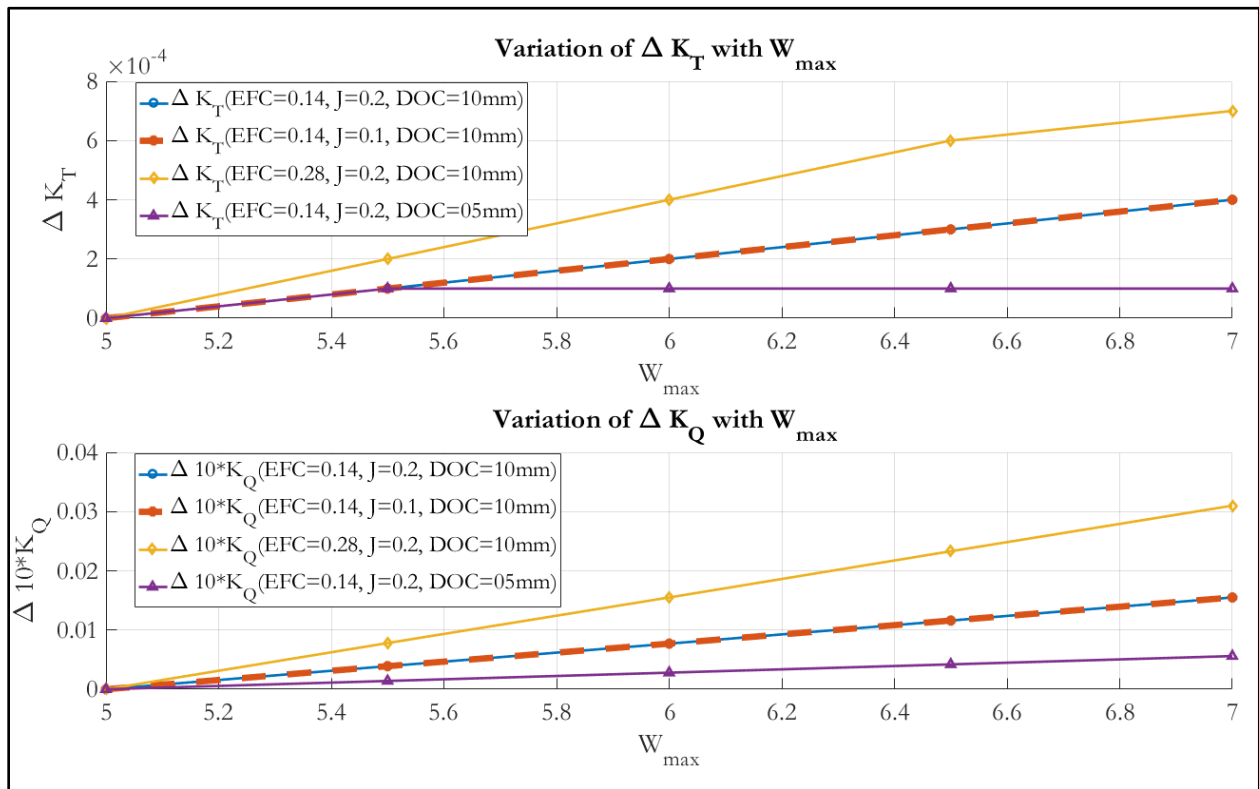


Figure 63: Influence of Parameters on the Sensitivity of W_{max}

5.4.3 Results from Polar Class Code

As mentioned in section 3.7 the numerical code Ice-PPB also compares the results obtained from the simulation with the IACS polar class code [3]. The polar class code has 7 classes from PC-1 to PC-7. The results from the polar class code are for full scale and the class code provides the value for the maximum permissible thrust and torque.

The results obtained from the simulation are therefore extrapolated to the full scale to obtain the thrust and torque values in order to be compared with the polar class code. Using the values from Table 1, the maximum permissible loads of all the 7 classes for the full scale Polarstern propeller are tabulated in Table 19.

Table 19: Maximum Permissible Loads on the Full Scale of Polarstern Propeller

Class	Maximum Thrust (kN)	Maximum Torque (kN-m)
PC - 1	829.55	9547.84
PC - 2	760.42	9547.84
PC - 3	706.72	9547.84
PC - 4	653.02	9547.84
PC - 5	477.80	8121.35
PC - 6	365.74	6097.23
PC - 7	365.74	5146.30

The maximum thrust and torque values shown in Table 19 are for the load case which yields the maximum value. The details about the load cases and the procedures for calculating the loads using the polar class code are shown in detail in Annexure 02 at the end of the report.

Chapter 6

CONCLUSION

This report describes the development of a numerical simulation tool for the calculation of loads on propellers during their interaction with ice. An ice class propeller of a German research vessel, Polarstern was used to perform the experiments in model scale and calibrate the numerical tool. Post calibration; a number of results were generated and the influence of various parameters on the ice loads acting on the propellers was studied.

The present chapter summarizes the findings of the research work and highlights the assumptions and the shortcomings of the methodology used and at the same time provides recommendations to develop a better tool in future.

6.1 Conclusion

The methodology implemented to calculate the ice loads on a propeller during its interaction with ice was the one used by Wang, J [4, 5]. The total ice loads acting on the propeller was expressed as the linear superposition of the open water (separable) hydrodynamic loads, hydrodynamic loads due to the presence of ice (inseparable) and the ice contact loads. Although the experimental results are in a good agreement with the results of the numerical simulation, whether the assumption of linear superposition holds true in different scenarios or not, is not known due to the limited number of experiments being conducted owing to the shortage of resources and time.

Furthermore, no experiment was conducted to evaluate only the inseparable hydrodynamic loads, and the calibration of inseparable hydrodynamic loads was done by calibrating total loads, separable hydrodynamic loads and ice contact loads. This method of calibration was again based on the assumption that all the three types of loads could be linearly superimposed to obtain the total loads.

Additionally, another assumption in the above methodology was that the separable hydrodynamic loads acting on the propeller during its interaction with ice were the same as that of the open water conditions. This assumption holds true if the ice floes/particles were flowing naturally towards the propeller. However, in the water milling experiments conducted for evaluating the total loads on the propeller, an ice feeding device was present on the suction side of the propeller that led to some blockage of the flow towards the propeller. Due to the presence of the ice feeding device, the separable hydrodynamic loads acting on the propeller were slightly higher than the open water loads. In order to correctly model the influence of the ice feeding device, a RANSE code was required that could correctly estimate the wake field developed due to the ice feeding device at the upstream of

propeller. This modified wake field could then be fed as an input to the Ice-PPB to accurately calculate the separable hydrodynamic loads. The RANSE code simulation was however too expensive both in terms of time and resources and could not be performed within the framework of the present thesis.

6.1.1 Separable Hydrodynamic Loads

The separable hydrodynamic loads were calculated using a surface panel method which operated under the assumptions of the potential theory. In order to match the results with the experiments, a viscous correction was added which was essentially a mathematical manipulation of the surface normal vector of panels of the propeller blades. This correction was in addition to the flat plate friction correction present in the original code. The influence of various parameters on the hydrodynamic loads was studied and it was found out that the loads decrease with the increase in the advance coefficient irrespective of the value of the advance velocity and propeller RPM.

In addition to the advance coefficient, the hydrodynamic thrust load was also dependent on the position of the pod with respect to the flow of fluid around the propeller. The thrust values in case of the puller configuration of the pod, i.e. when the pod is located on the pressure side are higher than the thrust values in case of the pusher configuration of the pod, i.e. when the pod is located on the suction side. The difference in the thrust values depends on the shape and size of the propeller and the pod.

6.1.2 Inseparable Hydrodynamic Loads

The inseparable hydrodynamic loads also calculated by the surface panel method, come into the existence due to the proximity and blockage effect of the incoming ice floes thereby making them dependent on the size of the ice floes. Larger the size of the ice floes or the depth of cut, larger is the ice wake field and thus larger is the magnitude of the inseparable hydrodynamic loads.

These loads were calculated by only taking the blockage effect into consideration which although plays a major role is not the only effect. At high advance velocities, the formation of vortices takes place due to the presence of the ice particles in the propeller race and simulation of these vortices is not possible with the panel based code. An advance RANSE code simulation is required that also takes into consideration the kinematics of the ice particles as they are sucked into the propeller race by the accelerating fluid. This methodology requires the development of partial differential equations of motion for all the 6 degrees of freedom which are to be solved both in time and spatial domain, making the approach extremely complex and time consuming. Although the accuracy of the results would be high, but that increased accuracy will come at the cost of very large computational time, making the process quite expensive.

6.1.3 Ice Contact Loads

The ice contact loads were divided into crushing and shearing loads and both the types of loads were obtained using the empirical formulae having different empirical factors for crushing and shearing phenomena. The empirical factors for crushing and shearing were dependent on the ice compressive strength and the propeller RPM at which the milling of the ice was carried out.

The ice loads varied linearly with depth of cut; the increase in the depth of cut increased the magnitude of the ice loads. However, the relationship was parabolic in terms of ice compressive strength due to the dependence of the empirical factors on ice compressive strength. A double fold increase in the ice compressive strength, quadrupled the magnitude of the ice loads acting on the propeller.

The relationship with the advance coefficient was dependent on the depth of cut. At a given depth of cut, the ice loads first increased in magnitude and then attained a constant value. This behavior of the ice loads was due to the shadow panels, as at higher J values no new shadow panels took part in the ice loads, making them constant. This critical J value, beyond which the ice loads did not increase was dependent only on the depth of cut and was independent of the propeller RPM and advance velocity.

For a given depth of cut and advance coefficient, the ice loads changed with the change in the RPM due to the dependence of empirical factor for crushing (EFC) on the propeller RPM. The loads decreased with the increase in the RPM, however, the value of critical advance coefficient remained unchanged as it is independent of the propeller RPM.

Furthermore, a sensitivity analysis of the code with respect to the empirical factors was carried out and it was observed that the sensitivity of all the empirical factors was dependent on a number of parameters like depth of cut and advance coefficient.

However, a major drawback of the present thesis lies in the fact that sufficient experiments could not be carried out to support the simulation results regarding the influence of various parameters on the ice loads as well as the influence of various parameters on the changes in the sensitivities of the code with respect to the empirical factors. By performing more experiments, the calibration of the code could be done in a better way as more number of data points would be available for performing the interpolations and statistical analysis.

6.2 Recommendations

From the discussions of section 6.1, following recommendations are suggested by the author in order to improve the code so that the loads acting on the propellers during their interaction with ice could be calculated with improved precision and accuracy:

- A RANSE code to be used instead of a panel based code to carry out simulations for calculating the hydrodynamic loads. The use of the RANSE will not only calculate the hydrodynamic loads with better accuracy but at the same will calculate the exact wake field at the upstream of the propeller due to the presence of the ice as well as the ice feeding device.
- In order to calculate the inseparable hydrodynamic loads with better accuracy, a study on the kinematics of the ice particles is to be done so that depending on the shape and size of ice particles, the momentum of each ice particle can be determined. Furthermore, using a RANSE simulation, the pressure distribution along the surface of the ice particles is to be determined so

that the vortex generation due to the ice particles can also be studied. The study of these phenomena will greatly improve the accuracy of the inseparable hydrodynamic loads.

- As far as ice contact loads are concerned, empirical factors were used to obtain the results. The empirical approach although provides quite accurate results, can be replaced by a more accurate analytical approach. To calculate the ice loads analytically, a detailed study regarding the ice fracture at high indentation speeds needs to be investigated.
- Finally, for the improved numerical simulation tool developed, the calibration should be done by performing a large number of experiments so that the validity of the tool can be assessed over a larger range of input parameters. A separate experiment also needs to be performed to calculate the inseparable hydrodynamic loads due to blockage and proximity phenomena.

ACKNOWLEDGEMENTS

This thesis was developed in the frame of the European Master Course in “Integrated Advanced Ship Design” named “EMSHIP” for “European Education in Advanced Ship Design”, Ref.: 159652-1-2009-1-BE-ERA MUNDUS-EMMC.

I would like to thank my supervisor Professor Dr. Nikolai Kornev for his guidance and mentoring throughout the duration of my thesis. I would also like to express my sincere gratitude to Professor Dr. Philippe Rigo and Professor Dr. Robert Bronsart for going out of their way to help me in securing an internship at Hamburgische Schiffbau-Versuchsanstalt GmbH (HSVA), Hamburg.

I am greatly indebted to Dr. Heinrich Streckwall, Department of Propellers and Cavitation, HSVA for helping in developing the numerical code Ice-PPB and interfacing the PPB with Ice-PPB. Without his immense help in the development of the hydrodynamic part of the thesis and multiple reviews and proof reads of the report despite his busy schedule, this thesis could not be delivered in the present form.

A special thank of mine goes to my supervisor at HSVA, Mr. Quentin Hissette, Department of Arctic Technology, HSVA, Hamburg, for helping in the coding of Ice-PPB, performing the experiments and reviewing this report multiple times.

At last but not the least I want to thank my family and friends who appreciated me for mine work and motivated me and finally to God who made all the things possible.

REFERENCES

- [1] *The Arctic*, Columbia Encyclopedia, Sixth Edition, Columbia University Press. 2004.
- [2] Streckwall, H., *Hydrodynamic Analysis of Three Propellers Using a Surface Panel Method for Steady and Unsteady Inflow Conditions*, 22nd ITTC Propulsion Committee (1998), Propeller RANS/Panel Method Workshop.
- [3] International Association of Classification Societies (IACS), *Structural requirements for Polar Class Ships*, Requirements Concerning Polar Class (2016), pp. I2-I3.
- [4] Wang, J., *Prediction of Propeller Performance on a Model Podded Propulsor in Ice (Propeller-Ice Interaction)*, PhD Thesis (2007), Faculty of Engineering and Applied Science, Memorial University of Newfoundland, Canada.
- [5] Wang, J., Jones, S.J., Bose, N., Kim, M.C., and Chun, H.H., *Ice Loads Acting on a Model Podded Propeller Blade*, Journal of Offshore Mechanics and Arctic Engineering, vol. 129 (2007), issue 3, pp. 236-244.
- [6] Jagodkin, V. Ya, *Analytical Determination of the Resistance Moment of a Propeller during its interaction with ice*, (translated from Japanese), Problem of the Arctic and Antarctic, vol. 13 (1963), pp. 79-88.
- [7] Ignatjev, M.A., *Determination of Ice Loads Encountered by Ship Propeller Blades*, (translated from Russian), Problems of the Arctic and Antarctic, vol. 15 (1964), pp. 41-51.
- [8] Wind, J., *The Dimensioning of High Power Propeller Systems for Arctic Icebreakers and Icebreaking Vessels*, International Shipbuilding Progress vol. 31 (1984), pp. 105-117.
- [9] Veitch, Brian J., *Propeller Ice Interaction*, PhD Thesis (1992), Faculty of Mechanical Engineering, Helsinki University of Technology, Finland.
- [10] Jones, Stephen J., *Propeller-Ice Interaction*, SNAME Transactions, vol. 105 (1997), pp. 399-425.
- [11] Soininen, H., *A Propeller-Ice Contact Model*, PhD Thesis (1998), Valtion Teknillinen Tutkimuskeskus (VTI), Espoo Finland.
- [12] Soininen, H., and Liukkonen S., *Laboratory Tests of Pressure Distribution around a Propeller Blade Profile during Ice Contact*, Proceedings of the International Shipbuilding Conference, October 8-12, 1994, pp. 90-97.

-
- [13] Soininen H., Liukkonen, S., and Muhonen, A., *Laboratory Tests of Propeller Blade Profile Pressure Distribution under Ice Contact*, vol. 1(1995), Meddelanden Research Notes 1664 pp. 70; vol. 2 (1995) Tiedotteita Meddelanden Research Notes 1664, pp. 324; Valtion Teknillinen Tutkimuskeskus (VTI), Espoo Finland.
- [14] Bach, C., *An Experimental Method for Model Propeller-Ice Interaction in Air: Concept and First Results*, Proceedings of the ASME 2017 36th International Conference on Ocean, Offshore and Arctic Engineering, June 25-30, 2017.
- [15] Evers, K. U., and Jochmann P., *An advanced technique to improve the mechanical properties of model ice developed at the HSV A ice tank*, Hamburgische Schiffbau- Versuchsanstalt (1993), Hamburg, Germany.
- [16] Okamoto, H. et al., *Experimental study on propeller ice interaction for ice breaking merchant ship (1st report, ice load model experiment)*, Journal of the Society of Naval Architects of Japan, vol. 1981 (1981), issue 149, Japan, pp. 100-110.
- [17] Okamoto, H. et al., *Experimental study on propeller ice interaction for ice breaking merchant ship (2nd report, static load test and FEM analyses)*, Journal of the Society of Naval Architects of Japan, vol. 1981 (1981), issue 150, Japan, pp. 359-370.
- [18] Chernuka, M.W., Jategaonkar, R.P., Norwood, M.E., and Warner, J.L., *Development of a Procedure for Predicting Propeller-Ice Interaction Forces*, Transport Canada Publication (1989), TP 9850E.
- [19] Bose, N., Veitch, B.J., and Doucet, J.M., *A Design Approach for Ice Class Propellers*, SNAME Transactions, vol. 106 (1998), pp. 185-121.
- [20] Varma, G.C., *Ice Loads on the Propellers Under Extreme Operating Conditions*, Master Thesis (2000), Faculty of Engineering and Applied Science, Memorial University of Newfoundland, Canada.
- [21] Norhamo, L., et al, *Challenges related to propulsor – ice interaction in arctic waters*, First International Symposium on Marine Propulsors (2009), Trondheim, Norway.
- [22] Pengfei, L., Bose, N., and Veitch, B.J., *Evaluation, design and optimization for strength and integrity of polar class propellers*, Journal of Cold Regions Science and Technology, vol. 113 (2015), pp. 31-39.
- [23] Tsarau, A., Lubbad, R., and Løset, S., *A numerical model for simulating the effect of propeller flows in ice management*, Journal of Cold Regions Science and Technology, in press, corrected proof (2016).

-
- [24] Polić, D., Æsøy, V., and Ehlers, S., *Transient simulation of the propulsion machinery system operating in ice – Modeling approach*, Journal of Ocean Engineering, vol. 124 (2016), pp. 437-449.
- [25] Ye, L.W., Wang, C., Chang, X., and Zhang, H.Y., *Propeller-ice contact modeling with peridynamics*, Journal of Ocean Engineering, vol. 139 (2017), pp. 54-64.
- [26] Det Norske Veritas AS, *Design of Propeller and Propeller Shaft*, Rules for Classification of Ships, part 5, chapter 1, Ships for Navigation in Ice (2011), sub section 2.C 200, pp.13-14.
- [27] Bureau Veritas, *Propulsors in Ice*, Rule Note NR 584, Section 1, July 2012.
- [28] American Bureau of Shipping, *Propeller Strength Assessment*, Guidance Note on Ice Class (2005), chapter 3, pp.49-68.
- [29] American Bureau of Shipping, *Propulsion and Maneuvering Machinery*, Guide for Vessels Operating in Low Temperature Environments (2006), section 4.3, pp.16-17.
- [30] Nippon Kaiji Kyokai (Class NK), *Polar Class Ships and Ice Class Ships*, Rules and Guidance for the Survey and Construction of Steel Ships (2017), Part I.
- [31] MATLAB R2016a, © 1994-2017, The MathWorks, Inc.
- [32] Database, Images and Videos Archive, Hamburgische Schiffbau- Versuchsanstalt, Hamburg, Germany.
- [33] Veitch, Brian J., *Predictions of Ice Contact Forces on a Marine Screw Propeller during the Propeller–Ice Cutting Process*, Mechanical Engineering Series No. 118 (1995), Ship Laboratory, Helsinki University of Technology, Finland.
- [34] Bose, N., *Ice Blocked Propeller Performance Prediction Using a Panel Method*, Transaction of the Royal Institution of Naval Architects, Vol. 138(196).
- [35] Abdel-Maksoud, M., *Advanced Propulsion*, Lecture Notes, Hamburg University of Technology, Germany (2015), pp. 9–12. (Original Citation, *Study by H J Heinke at SV A Potsdam*)
- [36] Cammaert, A. B., and Muggeridge, D. B., *Ice Interaction with Offshore Structures*, New York: Van Nostrand Reinhold (1988), pp. 228.

ANNEXURE 01

A. Calculation of Geometrical Parameters of Panels

The panels that form the propeller are essentially skew quadrilaterals. Since, all the four points that form the panel are not coplanar; the calculation of centroid, area, etc. is more complex as compared to planar quadrilaterals. On processing the data files from PPB we have,

- The x, y and z coordinates of the all the points that form the panels
- The list of all the panels and for each panel, the index number of the points forming the panel.

Using the above data, the panels are generated and at the same time various geometrical parameters are calculated as mentioned below.

A.1 Calculation of the centroid

Consider a 3D quadrilateral panel shown in Figure A-1. There are 4 points A, B, C and D with coordinates (a_1, a_2, a_3) , (b_1, b_2, b_3) , (c_1, c_2, c_3) and (d_1, d_2, d_3) respectively.

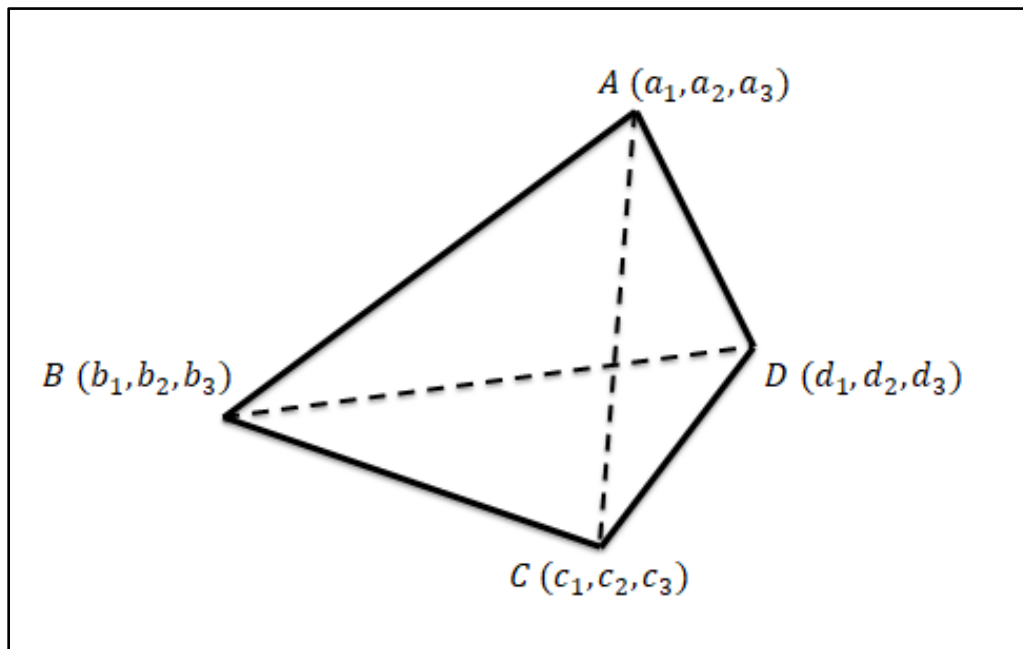


Figure A-1: 3D Quadrilateral

The quadrilateral is divided into two triangles, ΔABC and ΔADC . To calculate the centroid we first define a vector (\vec{R}) that contains the average of the 3 points of a triangle. For ΔABC we have,

$$\vec{R}_1 = \frac{a_1 + b_1 + c_1}{3} \hat{i} + \frac{a_2 + b_2 + c_2}{3} \hat{j} + \frac{a_3 + b_3 + c_3}{3} \hat{k}$$

For ΔADC we have,

$$\vec{R}_2 = \frac{a_1 + c_1 + d_1}{3} \hat{i} + \frac{a_2 + c_2 + d_2}{3} \hat{j} + \frac{a_3 + c_3 + d_3}{3} \hat{k}$$

Furthermore, we define two vectors per triangle and take their vector cross product. For ΔABC we have,

$$\vec{V}_1 = (a_1 - b_1) \hat{i} + (a_2 - b_2) \hat{j} + (a_3 - b_3) \hat{k}$$

$$\vec{V}_2 = (b_1 - c_1) \hat{i} + (b_2 - c_2) \hat{j} + (b_3 - c_3) \hat{k}$$

For ΔADC we have,

$$\vec{V}_3 = (c_1 - d_1) \hat{i} + (c_2 - d_2) \hat{j} + (c_3 - d_3) \hat{k}$$

$$\vec{V}_4 = (d_1 - a_1) \hat{i} + (d_2 - a_2) \hat{j} + (d_3 - a_3) \hat{k}$$

Taking the vector cross product, we have

$$A_1 = |\vec{V}_1 \times \vec{V}_2|, \quad A_2 = |\vec{V}_3 \times \vec{V}_4|$$

The centroid is defined as,

$$C(x, y, z) = \frac{A_1 \vec{R}_1 + A_2 \vec{R}_2}{A_1 + A_2}$$

A.2 Calculation of Normal, Radial and Tangential Vectors

The normal, radial and tangential vectors are fairly simple to calculate as compared to the centroid. To calculate the normal vector, we first define the two vectors as shown below.

$$\vec{V}_1 = (a_1 - c_1) \hat{i} + (a_2 - c_2) \hat{j} + (a_3 - c_3) \hat{k}$$

$$\vec{V}_2 = (b_1 - d_1) \hat{i} + (b_2 - d_2) \hat{j} + (b_3 - d_3) \hat{k}$$

The normal vector (\vec{N}) is obtained by taking the vector cross product of the above two vectors. Thus, we have,

$$\vec{N} = \vec{V}_1 \times \vec{V}_2$$

The unit normal vector (\hat{n}) is defined as,

$$\hat{n} = \frac{\vec{V}_1 \times \vec{V}_2}{|\vec{V}_1 \times \vec{V}_2|}$$

The radial vector (\vec{R}) of the panel is calculated using the centroid $C(x, y, z)$ of the panel and is defined as the radial distance of the centroid from the origin $O(p, q, r)$. Thus we have,

$$\vec{R} = (x - p) \hat{i} + (y - q) \hat{j} + (z - r) \hat{k}$$

The unit radial vector (\hat{r}) is defined as,

$$\hat{r} = \frac{\vec{R}}{|\vec{R}|}$$

The tangential vector (\vec{T}) of the panel is equal to the vector cross product of the normal and the radial vector. The tangential vector is, therefore, also calculated using the centroid. The tangential vector of a panel at the centroid is given as,

$$\vec{T} = \vec{N} \times \vec{R}$$

The unit tangential vector (\hat{t}) is defined as,

$$\hat{t} = \frac{\vec{N} \times \vec{R}}{|\vec{N} \times \vec{R}|}$$

A.3 Calculation of Area

To calculate the area of a skew quadrilateral, we first define 4 vectors as,

$$\vec{V}_1 = (a_1 - b_1) \hat{i} + (a_2 - b_2) \hat{j} + (a_3 - b_3) \hat{k}$$

$$\vec{V}_2 = (b_1 - c_1) \hat{i} + (b_2 - c_2) \hat{j} + (b_3 - c_3) \hat{k}$$

$$\vec{V}_3 = (c_1 - d_1) \hat{i} + (c_2 - d_2) \hat{j} + (c_3 - d_3) \hat{k}$$

$$\vec{V}_4 = (d_1 - a_1) \hat{i} + (d_2 - a_2) \hat{j} + (d_3 - a_3) \hat{k}$$

The area is calculated by taking a scalar dot product of the unit normal vector (\hat{n}) and the sum of the vector cross products of the above vectors. Thus we have,

$$Area = \text{abs} \left(\frac{\hat{n} \cdot (\vec{V}_1 \times \vec{V}_2 + \vec{V}_2 \times \vec{V}_3 + \vec{V}_3 \times \vec{V}_4)}{2} \right)$$

B. Calculation of KT, KQ and Efficiency

The values of KT, KQ and Efficiency are calculated from the values of C_p (Coefficient of Pressure) and Normalized Tangential Force per unit area (T_w) acting on the panels. The first step in the process is to calculate the normal and tangential force acting on each panel.

$$f_n = \frac{1}{2} \rho V^2 C_p A$$

$$f_t = \frac{1}{2} \rho V^2 T_w A$$

Where,

ρ = Density of Water

V = Advance Velocity

A = Panel Area

Next, we calculate the force in x, y and z direction acting on each panel. The distribution of the normal and tangential force in three directions depends on the unit normal (\hat{n}) and unit tangential vector (\hat{t}) of the panels. Thus for the pressure panels we have,

$$f_x = f_n \cdot n \hat{i} + f_t \cdot t \hat{i}$$

$$f_y = f_n \cdot n \hat{j} + f_t \cdot t \hat{j}$$

$$f_z = f_n \cdot n \hat{k} + f_t \cdot t \hat{k}$$

The suction panels have a negative normal and therefore the tangential vector of these panels points in the opposite direction to that of the pressure panels. Thus for the suction panels we have,

$$f_x = f_n \cdot n \hat{i} - f_t \cdot t \hat{i}$$

$$f_y = f_n \cdot n \hat{j} - f_t \cdot t \hat{j}$$

$$f_z = f_n \cdot n \hat{k} - f_t \cdot t \hat{k}$$

The total thrust acting on the propeller is given as,

$$T = \sum_{i=1}^s (f_x)_i$$

In order to calculate the torque, we first need to calculate the total moment generated by all the panels at the propeller axis. This is obtained by multiplying the force in y direction (f_y) by the z component of unit radial vector ($r \hat{k}$) and force in z direction by unit radial vector in y direction ($r \hat{j}$). Thus we have,

$$m_y = f_y \cdot r \hat{k}$$

$$m_z = f_z \cdot r \hat{j}$$

The total torque acting on the propeller is given as,

$$Q = \sum_{i=1}^S (m_y - m_z)_i$$

The thrust and torque coefficients are calculated as,

$$K_t = \frac{T}{\rho n^2 D^4}, \quad K_q = \frac{Q}{\rho n^2 D^5}$$

The efficiency is calculated as,

$$\eta = \frac{J K_t}{2\pi K_q}, \quad J = \frac{V}{nD}$$

Where

V = Advance Velocity

ρ = Density of Water

n = Model RPS

D = Model Diameter

S = Total number of panels

ANNEXURE 02

The IACS Polar Class Code was used to calculate the maximum permissible torque and thrust on the propeller.

The maximum backward force (F_B) on the propeller blade is given as,

- $D < 0.85 * (H_{ice})^{1.4}$

$$F_B = -27 \times S_{ice} \times (nD)^{0.7} \times \left(\frac{EAR}{Z}\right)^{0.3} \times D^2 \text{ kN}$$

- $D \geq 0.85 * (H_{ice})^{1.4}$

$$F_B = -23 \times S_{ice} \times (nD)^{0.7} \times \left(\frac{EAR}{Z}\right)^{0.3} \times D \times (H_{ice})^{1.4} \text{ kN}$$

The maximum forward force (F_F) on the propeller blade is given as,

- $D < \left\{\frac{2}{1-\frac{d}{D}}\right\} H_{ice}$

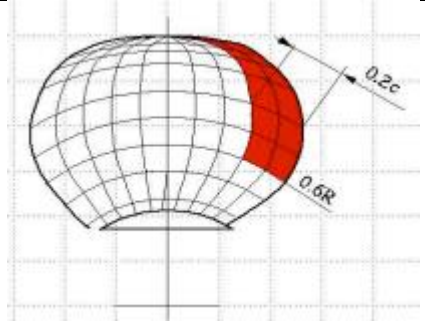
$$F_F = 250 \times \left(\frac{EAR}{Z}\right) \times D^2 \text{ kN}$$

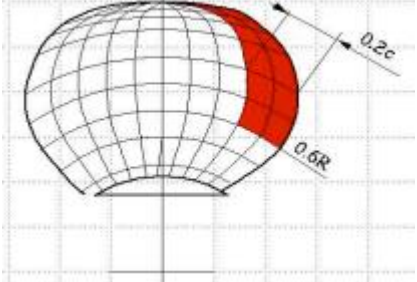
- $D \geq \left\{\frac{2}{1-\frac{d}{D}}\right\} H_{ice}$

$$F_F = 250 \times \left\{\frac{2}{1-\frac{d}{D}}\right\} \times H_{ice} \times \left(\frac{EAR}{Z}\right) \times D \text{ kN}$$

In order to calculate the maximum value of thrust, we take in consideration load case 1 for F_B and load case 5 for F_F . The maximum of the two values is the value for maximum thrust. The definition of the load cases is given in Table T below.

Table T: Load Case Definition

Load Case	Force	Loaded Area	Right handed propeller blade seen from back
Load Case 1	F_B	Uniform pressure applied on the back of the blade (suction side) to an area from $0.6R$ to the tip and from the leading edge to 0.2 times the chord length.	

Load Case 5	F_F	Uniform pressure applied on the blade face (pressure side) to an area from $0.6R$ to the tip and from the leading edge to 0.2 times the chord length.	
-------------	-------	---	--

The maximum torque (Q_{max}) on the propeller shaft is given as,

- $D < 1.81H_{ice}$

$$Q_{max} = 105 \times D^3 \times S_{qice} \left(1 - \frac{d}{D}\right) \left(\frac{P_{0.7}}{D}\right)^{0.16} \left(\frac{t_{0.7}}{D}\right)^{0.6} (nD)^{0.17} \text{ kNm}$$

- $D \geq 1.81H_{ice}$

$$Q_{max} = 202 \times D^{1.9} \times H_{ice}^{1.1} \times S_{qice} \left(1 - \frac{d}{D}\right) \left(\frac{P_{0.7}}{D}\right)^{0.16} \left(\frac{t_{0.7}}{D}\right)^{0.6} (nD)^{0.17} \text{ kNm}$$

Where,

D = Propeller Diameter

n = Propeller RPS

EAR = Expanded Area Ratio

Z = Number of Propeller Blades

d = Hub Diameter

$P_{0.7}$ = Pitch at 0.7R

$t_{0.7}$ = Thickness at 0.7R

H_{ice} = Ice Thickness for machinery strength design

S_{ice} = Ice Strength Index for blade ice force

S_{qice} = Ice Strength Index for blade ice torque

The values of H_{ice} , S_{ice} and S_{qice} depend on the polar class and the values for different classes is shown in Table U.

Table U: Values of Ice Thickness and Ice Strength Indices

Class	S_{ice}	$H_{ice}(m)$	S_{qice}
PC01	1.2	4	1.15
PC02	1.1	3.5	1.15
PC03	1.1	3.0	1.15
PC04	1.1	2.5	1.15
PC05	1.1	2.0	1.15
PC06	1.0	1.75	1.0
PC07	1.0	1.5	1.0